Growth and Structural Characterisation of Novel III-V Semiconductor Materials

Jacqueline Lesley Hall, MSci.

Department of Physics & Astronomy
University of Nottingham

Thesis submitted to the University of Nottingham
for the degree of Doctor of Philosophy

· July 2010 ·

Abstract

This thesis describes the growth and characterisation of four different III-V semiconductor materials. Growth was primarily performed by molecular beam epitaxy, while characterisation, which was largely structural, was carried out mainly using X-ray diffraction and atomic force microscopy.

Growth of low temperature (LT) GaAs was undertaken to investigate whether a phase transition accompanies the structural transition which occurs when GaAs is grown at temperatures below $\sim 150\,^{\circ}$C. It was found however, that LT GaAs remains zinc-blende, albeit with a significant degree of disorder. Migration enhanced epitaxy was subsequently used to grow LT GaAs, resulting in single crystalline GaAs at growth temperatures down to $115\,^{\circ}$C.

The possibility of using AlN as a source for nitrogen, in the growth of GaAs based dilute nitrides was explored. No conclusive evidence has been presented to suggest that small amounts of nitrogen were incorporated into the GaAs lattice.

The potential for ScN to be used as a buffer layer/interlayer to reduce the defect density in cubic GaN (c-GaN) was investigated. It was found that ScN grows on c-GaN(0 0 1)/GaAs(0 0 1) in a (1 1 1) orientation, leading to overgrowth of GaN occurring in the hexagonal phase. If the ScN interlayer was sufficiently thin (<3nm), then overgrowth of GaN was cubic, but no evidence of a reduction in stacking fault density was observed. Growth of ScN on GaAs(0 0 1) was also found to result mainly in a (1 1 1) orientation, but films were of poor quality. Growth of ScN on ScAs(0 0 1) was subsequently explored. ScN was found to grow in a (0 0 1) orientation, with both smoother surfaces and improved material quality than ScN(1 1 1). Growth of GaN atop ScN(0 0 1) was found to be c-GaN(0 0 1), but insufficient studies have been carried out to determine the effect on material quality.

During the growth of InGaN, it was found that unmounted substrates lead to large temperatures rises (>100 °C) for In rich compositions. Modelling heat absorption due to bandgap, phonon and plasmon absorption showed that this is due primarily to the large number of free carriers and not to the narrow bandgap (wrt substrate). The preliminary doping of $In_{0.8}Ga_{0.2}N$ with Mn was investigated. The amount of Mn that can be incorporated without causing a significant reduction in film quality was found to increase with decreasing growth temperature.

Publications and Presentations

Publications

- J.L. Hall, M.A. Moram, A. Sanchez, S.V. Novikov, A.J. Kent, R.P. Campion, C.T. Foxon and C.J. Humphreys, "Growth of ScN epitaxial films by plasma-assisted molecular beam epitaxy", *J. Cryst. Growth*, **311** 7 (2009) 2054-2057.

- C.T. Foxon, S.V. Novikov, J.L. Hall, R.P. Campion, D. Cherns, I. Griffiths and S. Khongphetsak, "Growth of GaN nanocolumns prepared by plasma-assisted molecular beam epitaxy" *J. Cryst. Growth*, **311** 13 (2009) 3423-3427.

- J.L. Hall, A.J. Kent, C.T. Foxon and R.P. Campion, "Temperature effects during the growth of $In_xGa_{1-x}N$ films through the whole compositional range by plasma-assisted molecular beam epitaxy", Accepted into *J. Cryst. Growth*: Awaiting publication.

Presentations

- (2008) - MBE 2008, Vancouver, Canada, Poster presentation entitled: *Growth of ScN films using plasma assisted Molecular Beam Epitaxy.*
- (2008) - Mini Symposium on Physics and Applications of InN and InGaN Semiconductor material, Grasmere, UK, Oral presentation entitled: *Growth Studies of ScN on GaN.*
- (2008) - UK Nitride Consortium summer meeting with UK Semiconductors, Sheffield, UK, Oral presentation entitled: *Growth Studies of ScN on GaN.*
- (2009) - Euro MBE 2009, Zakopane, Poland, Oral presentation entitled: *Growth of ScN films using plasma assisted Molecular Beam Epitaxy.*
- (2009) - UK Nitride Consortium summer meeting with UK Semiconductors, Sheffield, UK, Oral presentation entitled: *Temperature effects during growth of In-rich InGaN films by plasma assisted molecular beam epitaxy.*
- (2009) - IBPOWER, Madrid, Spain, Oral presentation for 18 month progress meeting.
- (2009) - Invited Talk, Dpt. Ingenieria Electronica, ETSI Telecomunicacion Universidad Politecnica, Madrid, Spain, Oral presentation covering aspects of chapters 4 and 5.

Acknowledgements

There are a great number of people who without their help, my PhD would not have been possible. Firstly my mentor Prof. Tom Foxon, leading on from his role the supervisor of my third year undergraduate project. He has always been (and I suspect always will be) there to answer any questions I might have, on a wide variety of topics. His help in not only increasing my understanding of the necessary physics, but also equally important, helping me plan new experiments to drive my work forward by subtly showing me that, at times, I kind of know what I'm doing, has been invaluable and is greatly appreciated.

I owe a great debt also to my PhD supervisor Dr. Richard Campion for teaching me how to use the MBE machines and for many stimulating conversations, particulary in regards to my InGaN project. Dr. Sergei Novikov's help in teaching me all the tricks required to operate the mini-MBE machine and how to grow nitrides was also invaluable, as well as his teachings of some of the finer points of 'life politics'.

For all the times I broke either the MBE machine, an electronic component or any of the computers I'd like to thank the technicians: Steve Tabreham, Bob Chettle (who also put up with all my mountaineering queries), Andrew Wilson (old computer guy) and Michael Parker (new computer guy), plus all the others that helped along the way.

Chris Staddon not only trained me in how to use the X-ray equipment, but more importantly provided me with conversations on what it all meant as well as suggestions for more obscure/detailed scans to reveal further information. I'd also like to thank Dr Matt Blunt in training me in the AFM.

There have many people who have helped me to further characterise my samples. From the University of Nottingham, I'd like to thank Dr. Andy Rushworth who performed all the SQUID measurements and Dr. Nicola Farley who helped considerably when I decided EXAFS measurements should be performed. She not only put together the proposal and secured us beam time, but helped with (and showed me how to do) the measurements and carried out the analysis.

In regard to my dilute nitride project, I owe thanks to Prof. Eric Larkins for arranging SIMS analysis. For the Sc related work, I'd like to thank the Cambridge collaborators organised by Dr. M. Moram for TEM analysis and the Warwick

collaborators, Prof. Chris McConville and Louise Bailey, for all their electrical and transport characterisation.

In keeping me sane, I owe a great amounts of thanks to all my office mates (past and present), in particular James and Ryan for all our climbing soirées. A special thanks goes to Anna, how will I live without those morning coffee breaks.

Finally, I suppose I should thank my husband, Chris. Seriously, without his support, those times of difficultly would have felt infinitely harder. Sorry for all those times I dragged you to the physics department with me. I will (eventually) make up for those lost weekends and evenings. I owe thanks to my beautiful daughter Esme, for giving me such as definite deadline to adhere to. Thanks also to my family for getting me here in the first place.

Contents

Thesis Outline

The work described in this thesis is primarily concerned with the growth and structural characterisation (mainly by XRD) of bulk III-V semiconductor materials. Experimental results are presented over four chapters, each of which represents work based around a different material system. As such, each chapter has its own introduction outlining the motivation behind the work, as well as a short literature review. Conclusions and further work are also presented at the end of each results chapter, though the main results from all the work can be found in a standalone chapter at the the end.

Chapter 1 outlines the principles of the main experimental techniques used in this work. Detailed descriptions are given on the MBE growth method. This includes how band-edge spectrometry is used to measure the temperature of samples in a vacuum, as well as an outline of the RHEED technique as a tool for surface structure analysis. The description of RHEED, explains the underlying physics of the technique and also why surface atoms often differ in structure to those in the bulk. An overview of the most used ex-situ characterisation techniques is presented, with a particular emphasis on the use of X-ray diffraction to determine key structural parameters such as phase and crystallinity of material, lattice parameters, strain and as a qualitative tool for assessment of material quality.

The following four chapters include all the experimental results. Chapter 2 refers to the work carried out on GaAs grown at low growth temperatures ($< 200\,^{\circ}\mathrm{C}$). It had been suggested that growth at very low growth temperatures would result in GaAs growing in a rock-salt phase compared with the conventional zinc blende polytype. Different polytypes of a material are expected to have different properties, therefore if rock-salt GaAs could be achieved it would be interesting material system to investigate. Although a structural transition was witnessed at a growth temperature of $150\,^{\circ}\mathrm{C}$, this was to amorphous/microcrystalline but still

zinc-blende material. The use of migration enhanced epitaxy (as a slight modification of the MBE technique) was therefore investigated, as a means of achieving good quality GaAs down to growth temperatures of 120 °C. This technique was also used as an alternative to growing Mn-doped GaAs at growth temperatures of $\sim$ 150 °C. Potentially, this could lead to epitaxial growth of GaMnAs at lower temperatures, allowing for larger incorporations of Mn to be achieved. This is predicted to raise the temperature at which GaMnAs behaves like a ferromagnetic (the Curie temperature, Tc), hopefully pushing Tc towards room temperature [1].

The production of dilute nitrides with emission wavelengths in the 1.3-1.55 µm range holds attraction for optical fibre applications, such as high speed data transmission [2]. The incorporation of the necessary amounts of N into Ga(In)As has proved problematic, with larger concentrations of nitrogen associated with decreased emission efficiency [3]. This is generally due to nitrogen being supplied by a plasma source, which damages the growing surface with increasing operating power and nitrogen flux [4]. The sublimation of AlN is potentially a way of supplying nitrogen without the need for damaging active nitrogen radicals and a plasma source [5]. Work investigating dilute nitride semiconductors using the sublimination of AlN as a novel source of nitrogen is presented in chapter 3.

Despite the success of GaN based blue LEDs for use in solid-state lighting, the expected numerous other applications have not yet materialised. The main problem with GaN based materials is the high level of structural defects [6]. These arise from a lack of suitable substrates, which result in GaN being grown on materials with very different lattice parameters and temperature characteristics [7]. One successful approach in reducing the dislocation density in hexagonal GaN has been the use of ScN interlayers [8]. The motivation of the work reported in Chapter 4 is to investigate whether this approach can be applied to reducing the number of stacking faults in cubic GaN. Cubic GaN offers many potential benefits over the thermodynamically stable GaN polytype hexagonal. The main advantages are (i) lack of polarisation effects (ii) expected higher electron and hole mobilities and (iii) easier to fabricate into devices such as lasers [7]. Chapter 4 details the work carried out on ScN as a means of improving the material quality of cubic GaN. Growth of ScN was carried out on a variety of different materials, resulting in growth in different orientations. This included the growth of ScAs, a material that has not been well studied in the literature. Also outlined in the chapter are results from the growth of GaN on different orientations of ScN.

Preliminary work into ScGaN and Mn-doped ScN has been carried out and is also discussed in chapter 4. The ScGaN alloy system potentially offers a way of achieving emission in the green wavelength range, a spectral range that does not yet have adequate representation [6]. Mn-doped ScN meanwhile has been predicted to exhibit ferromagnetic behaviour at room temperature [9].

Due to the small 0.7 eV bandgap of InN and the high 3.4 eV bandgap of GaN, the InGaN alloy has the potential to span the whole visible spectrum, making it attractive for numerous optical applications, e.g. solar cells and light emitting devices. Good-quality growth can be problematic, due to the different properties of InN and GaN. There exists a narrow window of optimal growth conditions. If these are not met, segregation of In and phase separation can occur leading to poor emission [10–13]. The incorporation of a suitable amount of dopant elements provides the opportunity to form an absorption band in addition to the bandgap of the host material, ideally located in the middle of the main bandgap. It has been predicted that for $In_{0.8}Ga_{0.2}N$ doped with small small amounts of Mn ($\sim 0.25\%$) such an intermediate band structure could occur [14]. This interesting material has applications in solar cell research, as it potentially provides a mechanism of a single cell being able to absorb photons of differing energy, independently of other absorption processes [15].

The final experimental chapter, chapter 5, looks at growth studies of In-rich InGaN. The effects of growth temperature (and effects of experimental set-up on growth temperature) are outlined in detail. Also presented, are results from efforts to control alloy composition. The end of this chapter describes initial studies on structural quality of doping InGaN with Mn, including how much Mn can be incorporated into InGaN and not adversely affect film quality and also how this concentration changes with growth temperature.

Finally all of the main results are summarised in chapter 6. A list of publications and conference presentations can be found following the abstract on page iii.

Chapter 1

Experimental Techniques

1.1 Molecular Beam Epitaxy (MBE)

Molecular beam epitaxy (MBE) is an ultra high vacuum (UHV) based technique used for the production (or 'growth') of high-quality epitaxial structures. Monolayer control, uniformity and high purity permit the growth of complicated heterostructure semiconductors, where interfaces between layers of differing structural and chemical properties need to be well defined.

1.1.1 Basic Principles

MBE is in principle, a basic technique; a typical experimental arrangement is shown in figure 1.1. In a conventional set-up, solid (or liquid) sources are heated up in effusion cells until they sublimate (or evaporate). During growth, shutters placed in front of the source(s) are opened, allowing atomic/molecular beams to impinge, collision free, on a heated substrate. On arrival at the substrate, surface atoms/molecules can adsorb (physical adsorption or chemisorption), migrate, interact with other atoms/molecules, dissociate, incorporate into the growing crystal or desorb. If the conditions are right, then the film can grow in an ordered monolayer by monolayer, single crystalline manner to form a set of epitaxial layers (or epilayers for short). Not all materials though, require growth in a 2D layer by layer mode (Frank van der Merwe [16]). 3D growth modes (Volmer-Weber [17] and Stranski-Krastanow [18]) can be employed for the production of quantum dot

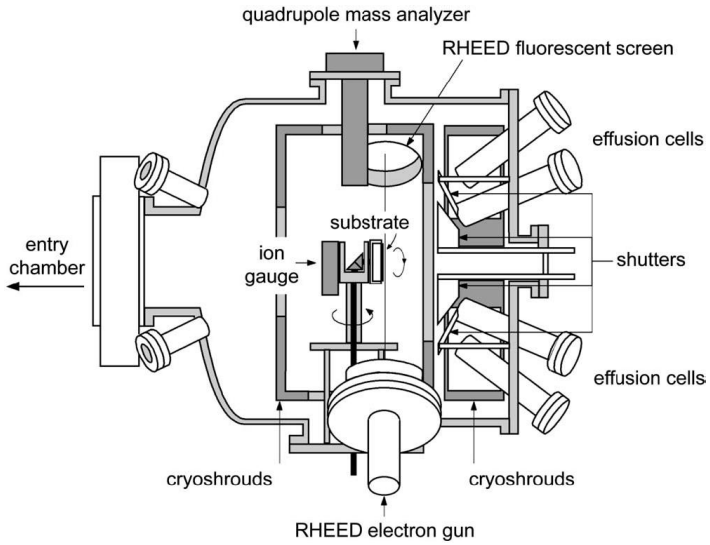

Figure 1.1 – Schematic of an MBE growth chamber. Figure taken from Franchi 2003 [19].

structures [19] and nanowires [20]. For a more detailed description of MBE, both as a technique and its applications, the reader is referred to the review authored by C.T. Foxon [21].

The substrate ideally acts as a seed crystal, encouraging the depositing film to takes on a lattice structure and orientation identical to that of the substrate. If the growing film has the same composition and crystal structure as the substrate, then the process is referred to as homoepitaxy, otherwise the process is called heteroepitaxy. Although homoepitaxy is generally preferred, it is not always a realistic option. Single crystalline bulk substrates of a material are not necessarily commercially available or can be prohibitively expensive. When selecting an appropriate substrate for growth, several factors need to be taken into account; lattice parameter, orientation, polytype, thermal expansion properties, cost, preparation and doping. Generally there is a trade off between material quality (high lattice mismatch introduce strain and eventually defects) and cost.

The sample substrate is held on a holder which can be rotated and heated. The temperature of the substrate is often referred to as the growth temperature. Sample rotation allows material from all cells to be deposited evenly onto a substrate surface during growth. Ideally at least one rotation is performed per monolayer of growth. The flux from each cell is dependent on the cell temperature and is measured by an ion-gauge that can be rotated into the substrate growth position. Fluxes are measured in units of pressure, generally mbar or Torr.

The complexity of MBE arises from the high vacuum needed to produce high purity films. All movements within the equipment must, therefore, be achieved without significant outgassing or leaks. To this end, multi-chamber systems are used; in addition to the growth chamber, additional chambers are used to introduce samples into the vacuum environment and to prepare wafers in-situ before introduction into the growth chamber. It is common for additional chambers to be added for post-growth analysis, allowing the movement and analysis of grown samples without the need to come to air.

UHV conditions also allow the use of in-situ analysis tools, such as quadrupole mass analyzers (to monitor the vacuum environment) and refection high energy electron diffraction (RHEED) equipment (to study the growing surface), which have become standard additions to an MBE machine. Other characterisation techniques, such as Auger electron spectroscopy (AES), X-ray photoelectron spectroscopy (XPS), secondary ion mass spectroscopy (SIMS) and scanning tunneling microscopy (STM), can also be positioned in the growth chamber. These however, are more frequently located in separate chambers.

Liquid nitrogen cooled cryoshrouds placed in the growth chamber help to improve the vacuum and ensure UHV conditions during growth, as well as removing heat from the substrate heater and cells. Additional cryoshrouds surround the cells preventing thermal cross-talk.

Growth rates are typically in the order of a few Å s^{-1} and beams can be shuttered in a fraction of a second. This means shutters can generally be opened or closed in less time than it takes to grow one monolayer of material. It is this feature in MBE that allows for atomically abrupt interfaces and, consequently, the production of complex structures.

1.1.2 Machine set-ups

Two MBE machines were used to carry out the investigations reported in this thesis: (i) a Veeco Gen III (referred to as simply the Gen III) and (ii) a custom built 'mini-MBE' system.

The low-temperature growths of GaAs were performed in the Veeco Gen III, which has a background pressure in the region of 10^{-10} Torr. The growth chamber has

the capacity for 14 effusion cells. At the time of use these housed several group III sources (In, Al and two Ga solid sources), two solid As sources (provided through a valved arsenic cracker providing As_2, rather than the tetramer As_4), magnetic materials (Co, Fe and Mn), dopant elements (Si and C) and a gaseous H_2 source. Two ports were used by the BandiT equipment (used to measure the growth temperature, see section 1.2), one each for light source and detector. The chamber also has a 12 keV RHEED facility for surface reconstruction analysis and a mass spectrometer to study the presence and composition of background gases.

For all other work reported in this thesis the 'mini-MBE' system was used (see figure 1.2), which has an ultimate base pressure in the region of 10^{-9} mbar. The growth chamber has the capacity for five effusion cells. At all times, three effusion cell ports housed a Ga cell, an As cell (provided through a cracker) and an Oxford applied research (OAR) RF plasma source to provide activated nitrogen. For the dilute nitrides work, the additional cell ports housed elemental Al and AlN powder (99% purity). The cell used to provide AlN was a specialised high temperature cell which was run at $\sim$1400 °C. During the investigations on Sc containing compounds and InGa(Mn)N, the two additional ports housed either Sc (in a high temperature cell), In, Mn or Al. The system also has a RHEED facility (12 keV) for surface reconstruction analysis. Due to the fact that this is a custom built machine, it differs from conventional modern systems. The key differences between this system and the commercial systems available are outlined below:

1. Samples cannot be continuously rotated during growth, though they can be manually rotated in order to look at different azimuths in the RHEED.

2. Samples are not mounted on pyrolytic boron nitride (PBN) plates, but are effectively free standing with only a very small area of contact with the holder. In this way, the back side of the wafer directly faces the substrate heater.

3. There is no buffer chamber between the main growth chamber and the load lock.

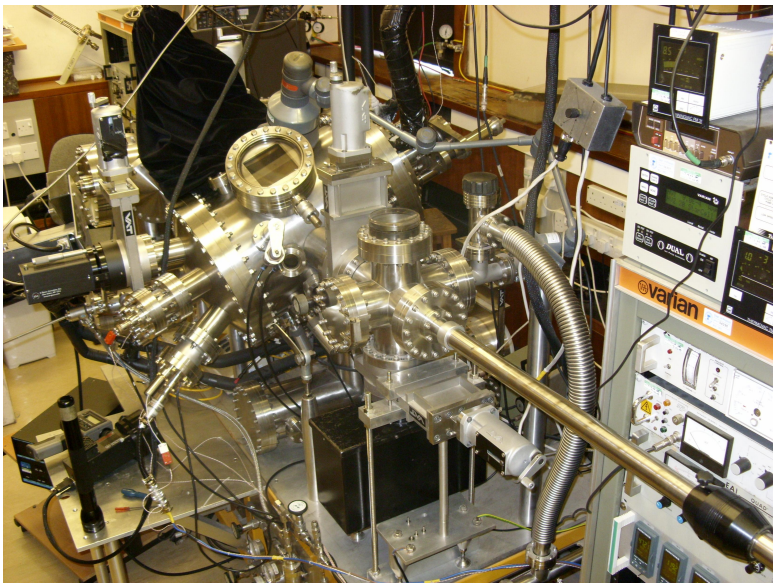

Figure 1.2 – Picture of the 'mini-MBE' system

1.2 Temperature Monitoring using BandiT

Until recently, accurately measuring the sample temperature was a serious difficulty in MBE. Traditional thermocouples indicate more accurately what is happening to the heater, rather than the sample itself. Pyrometry, a common tool for measuring sample temperature, can typically only be used for growth temperatures above 500 °C. Additionally, it suffers from being emissivity dependent, a problem if the emissivity is unknown or changes with growth, as is common with heteroepitaxy and during growth of new material systems.

The MBE machines used in this work are equipped with a k-Space Associates (kSA) BandiT. It is a non-invasive, real time, absolute substrate temperature sensor which exploits the fact that a semiconductor's bandgap varies with temperature.

As thermal energy is applied to a material, there is an increase in atomic vibrations. This leads to an increase in the inter-atomic spacings, an effect quantified by a material's linear expansion coefficient. The longer bond lengths mean the electric potential experienced by the electrons decreases leading to a reduction in the bandgap energy, E_g. The temperature dependence of the bandgap in semiconductors has been experimentally determined and is represented by the

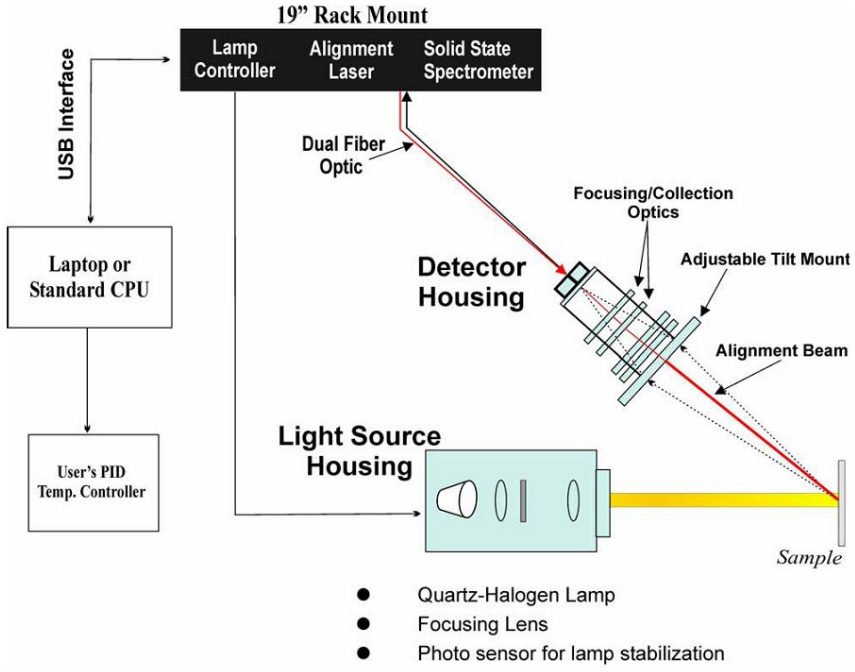

(a) Schematic of a kSA BandiT setup

(b) Example of kSA BandiT software display

Figure 1.3 – kSA BandiT product schematic and example software display. Figure (a) taken from www.k-space.com

semi-empirically derived Varshni equation [22]:

$$E_g(T) = E_g(0) - \frac{\alpha T^2}{T + \beta} \tag{1.1}$$

where $E_g(0)$, α and β are material dependent parameters.

Since semiconductors are transparent for $h\nu < E_g$ and opaque for $h\nu > E_g$, by measuring the wavelength of a material's absorption edge, the BandiT is able to infer its bandgap energy and therefore its temperature.

To measure the absorption edge, diffusely scattered light from the sample is used. The light can come from either the substrate heater directly (*transmission mode*), with a single port for the detector, or shone from an external kSA light source, mounted on a second port, (*reflection mode*). The detector, mounted on a non-specular port, uses collection optics to carry the light to a solid state spectrometer. The spectrum is then sent to a computer via a single USB connection, where it undergoes a fitting procedure to determine the wavelength, and thus energy, of the absorption edge. To reduce noise, a background reference can be subtracted from the raw data before the fitting stage. Using the library of kSA generated calibration tables integrated into the software, a real-time temperature output display of the substrate temperature is available, see figure 1.3. Since films in MBE are generally thin, it is assumed that the temperature of the growing material is equal to that of the substrate.

The dependence of the BandiT system on only the bandgap of the substrate is an important feature of this set-up. This advantage over pyrometry means that the substrate temperature can be controlled during deposition or etching, when the emissivity could be changing. Other advantages include: insensitivity to changing view port transmission, e.g. coating and stray light, low temperature sample monitoring and allowing for absolute temperature calibration from machine to machine. In addition, the automatic readout means that temperature fluctuations due to sample rotation and temperature increases due to exposure from cells can be easily detected.

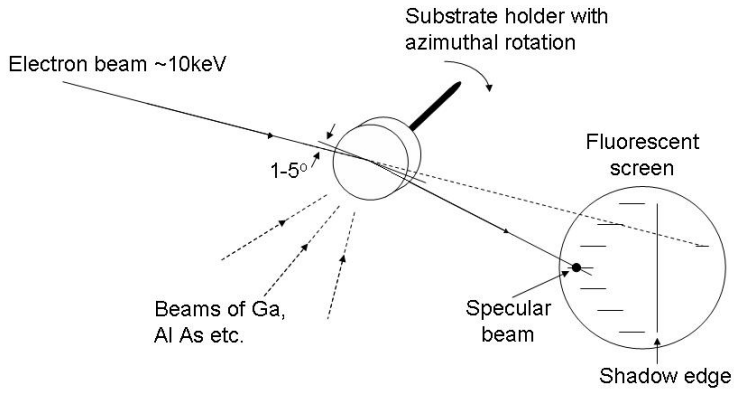

Figure 1.4 – Schematic diagram of the application of RHEED to MBE (or any thin film growth technique).

1.3 Reflection High Energy Electron Diffraction (RHEED)

The UHV environment in MBE allows the employment of diffraction techniques, such as RHEED and low energy electron diffraction (LEED), to study the a samples surface structure. These techniques require vacuum in order to minimise the scattering of electrons by background gas molecules.

Although LEED is the more common and theoretically understood method for determining surface structure, its requirement for near normal incidence and diffracted beams proves impractical in MBE, where it would interfere with the rest of the equipment. In RHEED the electron gun and viewing screen are positioned at low angles relative to the substrate surface, see figure 1.4. This allows it to be used for real time analysis and continuous monitoring of crystal growth and growth dynamics.

The intensity of RHEED features is particularly sensitive to surface roughness, down to the monolayer scale. This allows the growth rate of a depositing film to be calculated by analysing so-called s'RHEED oscillations', see section 1.3.3.

1.3.1 RHEED Technique

RHEED is based on the reflection of high energy electrons, typically in the 5-50 keV range. Despite the incoming electrons high energy and therefore large

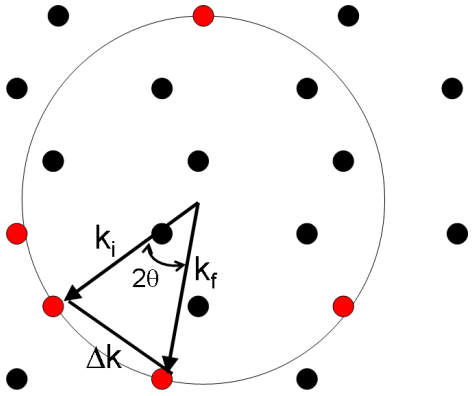

Figure 1.5 – The Ewald construction. The lattice points (or corresponding planes) highlighted in red give rise to diffraction.

mean free path, the technique is surface sensitive due to the electrons low angle of incidence, typically less than 5°. In this instance the penetration depth of an electron beam is small, total external reflection of the electron beam will occur and beams will be diffracted out of the crystal after passing through only a few atomic layers. The result being that the diffraction pattern is determined by the periodicity of the crystal surface.

In order to visualise which lattice planes will result in diffraction (and hence the resolution of a diffraction technique for a given wavelength and cell dimensions) the Ewald sphere concept is often used. In reality this is more generally a circle, rather than a sphere. The Ewald sphere is an imaginary geometry construct with a radius $2\pi/\lambda$, which corresponds to the length of the incident plane wave's (k_i) wave vector. Assuming that the diffraction process is elastic, then the scattering vector (k_f) also a wave vector whose length is $2\pi/\lambda$. Since k_i and k_f have the same length the scattering vector must lie on the surface of a sphere of radius $2\pi/\lambda$. To assess which condition will lead to diffraction, the Ewald sphere is superimposed onto a map of reciprocal lattice vectors, figure 1.5. Where lattice points touch the edge of the sphere, momentum transfer satisfies the Bragg condition and diffraction occurs.

At high energies the wavelength of the electron is small and the radius of the Ewald sphere, k_o, is large, compared to typical reciprocal lattice vectors. At 10 keV, λ=0.037 nm and k_i=170 nm^{-1} whereas $2\pi/a$ might typically be 20 nm^{-1}, making RHEED an extremely sensitive technique. Since the Ewald sphere is so large in a RHEED experiment, it is necessary to change the diffraction geometry in order to find the arrangement of reciprocal lattice rods in three dimensions and thus,

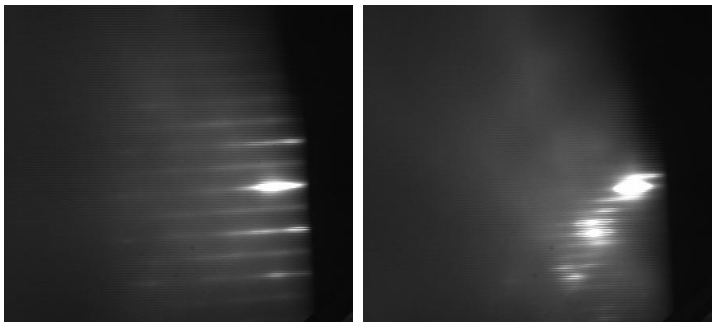

(a) GaAs [1 1 0] (b) GaAs [$\bar{1}$ 1 0]

Figure 1.6 – RHEED patterns obtained at 12 keV from a smooth (0 0 1) GaAs surface showing a 2x4 reconstruction. (a) [1 1 0] azimuth 2x; (b) [$\bar{1}$ 1 0] azimuth 4x.

define the unit mesh. All the reciprocal lattice rods can be explored by rotating the surface normal. As the azimuthal angle is varied, simple diffraction patterns can be observed when the incident beam is along a direction of high crystal symmetry. An example of RHEED patterns from a As stabilised GaAs(001) surface in two azimuths is shown in figure 1.6.

If electrons interact only with the first atomic layer of a perfectly flat and ordered surface, the three-dimensional reciprocal lattice points degenerate into parallel infinitely thin rods. The resulting intersection with the Ewald sphere would consist of a series of points placed on a half circle, known as a Laue ring or zone.

In reality, thermal vibrations and lattice imperfections cause the reciprocal lattice rods to have a finite thickness, while the Ewald sphere itself has some finite thickness, due to divergence and dispersion of the electron beam. These factors combined with the extreme sensitivity of RHEED, mean a nearly flat surface results in a diffraction pattern consisting of a series of streaks, see figure 1.6, rather than points, as would be seen in LEED.

If the surface is not flat, electrons will be transmitted through surface asperities and scattered in different directions. This would result in a RHEED pattern consisting of many spotty features. The first important information provided by RHEED in MBE therefore, often regards the flatness of a surface.

Diffraction from an amorphous surface (such as an oxide on top of a semiconductor) gives no diffraction pattern; only a diffuse background. This is useful for evaluating oxide desorption from a new substrate prior to growth in the MBE chamber.

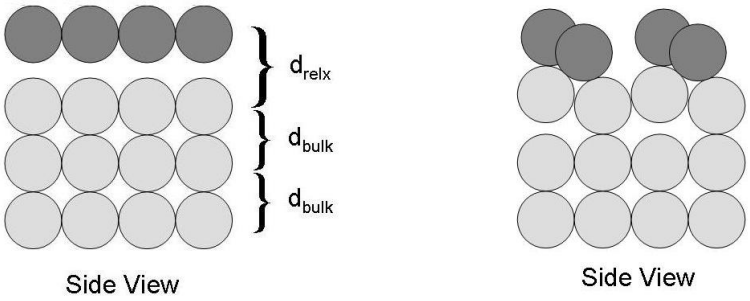

(a) relaxation (b) reconstruction

Figure 1.7 – Atoms at a surface often exhibit a different structure to those in the bulk, surface atoms can undergo either relaxation (a) and/or reconstruction (b).

1.3.2 Surface Crystallography

As well as topographical information, a RHEED image can also provide information on surface structure. Surface atoms of a clean surface tend not to be in the positions expected from a simple termination of the bulk structure. The term surface therefore, normally refers to the outermost atomic layers (monolayers) that differ structurally from the bulk material; generally speaking this is about three monolayers. Atoms at and near the surface can move either perpendicular to the bulk structure (relaxation) or both perpendicular and parallel (reconstruction) to the bulk structure, figure 1.7.

In relaxation, the outer layer relaxes bodily outwards or inwards, but the structure parallel to the surface remains the same as the bulk, i.e. $d_{relx} \neq d_{bulk}$ where d_{relx} is the layer spacing of the surface layer and d_{bulk} is the layer spacing in the bulk sample, see figure 1.7(a). This generally has no effect on densely packed surfaces, but for more open channelled surfaces the effect can be sizable e.g. for Ag(1 0 0), $(d_{relx} - d_{bulk})/d_{bulk}$ is 0%, while for Ag(1 1 0) the figure is -9%. Relaxation is common in metals and has its origin in the overflow of electrons into the vacuum.

In reconstructed surfaces, the top layer(s) of atoms move both perpendicular and parallel with respect to the bulk, in order to attain a minimum energy configuration, see figure 1.7(b). Bonds that would otherwise be formed to material above in a bulk crystal scenario, cause atoms to pull together leading to surface bond formation. Reconstruction is more common for semiconductors, where atoms have highly directional covalent bonds. These surface atoms experience a much larger difference in interatomic force (relative to bulk atoms) than that experienced by

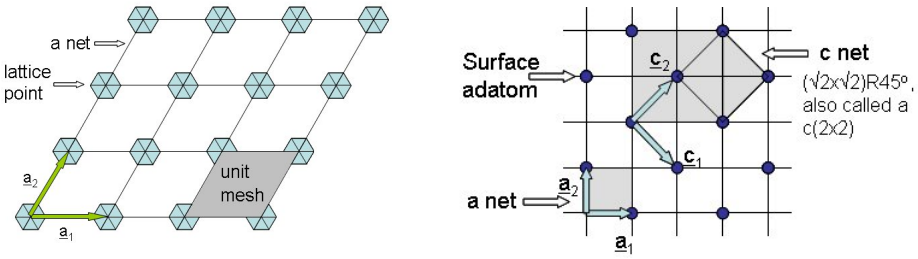

(a) *a nets* are used to describe unreconstructed surface structures

(b) *a* and *c nets* are used to describe an overall surface structure; whereby arrangements of atoms on a surface are different to those in the bulk structure

Figure 1.8 – Bravais nets are used to describe 2D structures.

metallic surface atoms. Reconstruction can occur in metals which have highly directional electrons, for example gold, which has d and f electrons. There is no need for the periodicity of the surface to differ from the bulk, but it often does, generally assuming an in-plane periodicity greater than in the bulk. The surface unit mesh (2D unit cell) may consist of the same, fewer or more atoms than that of the bulk. The specific reconstruction depends critically on the material, the surface orientation and the surface termination (that in turn is a function of temperature and composition of ambient gases).

To describe 2D structures, 2D Bravais nets are used, cf. 3D Bravais lattices for bulk material. To describe the arrangement of surface atoms it is useful to introduce the notion of *a*, *b* and *c nets*, all of which are Bravais lattices. The *a net* generally describes the Bravais net associated with the surface and has a unit mesh described by vectors a_1 and a_2, see figure 1.8(a). If adsorbed foreign atoms (or molecules), adatoms, on a surface are viewed by themselves, they sometimes form a regular structure, called the *b net*. When the adatoms and substrate atoms are considered together the periodicity of the entire surface is represented by the adlayer *c net*. While the *b net* can be interesting, it is the *c net* that gives the more useful information.

In order to describe reconstructed surfaces, it is common practice to envisage 'out of position' surface atoms as foreign adatoms. In this case, the structure of a hypothetical slice through the bulk material is described by the *a net* and the reconstructed surface atoms by the *c net*. Wood notation is used to relate the *c net* to the *a net* (ideal bulk termination). The side lengths of the substrate mesh are taken as unity and the adlayer net size is given relative to this. In long form,

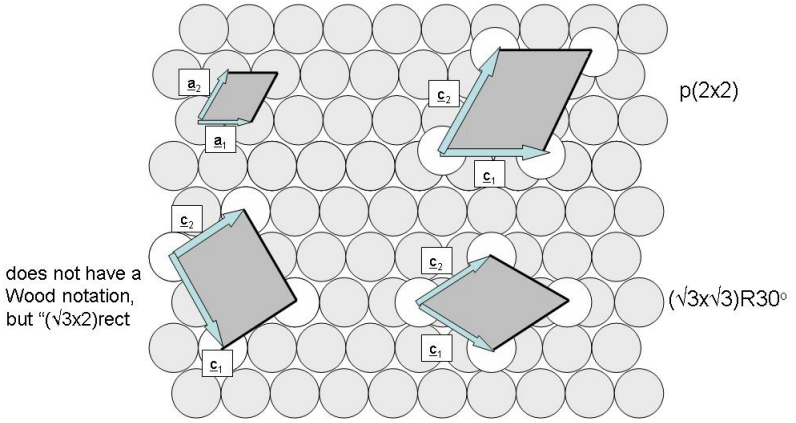

Figure 1.9 – Various reconstructions and their associated Wood notations.

Wood notation is expressed as:

$$\text{substrate(Miller index)- w } [(b_1/a_1) \text{ x } (b_2/a_1)]R\theta \text{ - N adsorbate}$$

where w describes the type of cell and is p if the unit cell is primitive (contains only one atom/molecule) and c if the unit cell is described as a centered unit cell (has a lattice point in center of cell, example given in figure 1.8(b).). $R\theta$ is the angle of rotation between the *c net* and the *a net*. The number, N, preceding the adsorbate chemical symbol, is the number of adsorbate molecules in the unit cell, if primitive N is omitted. The omission of w indicates that the substrate unit cell is primitive, while the omission of Rθ means that the *c net* is not rotated with respect to the *a net* and if describing a reconstructed surface then N adsorbate is omitted.

For example, Pt(100)-($\sqrt{2}$ x $2\sqrt{2}$)-R45°-O describes how oxygen adsorbs onto a platinum (1 0 0) surface and Si(111)-(7x7) describes the surface reconstruction of Si on a (1 1 1) surface. Examples of reconstructions and their Wood notation can been seen in figure 1.9.

RHEED gives a diffraction pattern which is a picture of the surface in reciprocal space. The relationship between a Bravais net in real and reciprocal space therefore needs to be understood, in order to relate the diffraction image to a real structure.

Let the reciprocal space net to the *a net* be described by a*, with translation vectors $\underline{a}_1^*$ and $\underline{a}_2^*$. The translational vectors of the real and reciprocal space nets

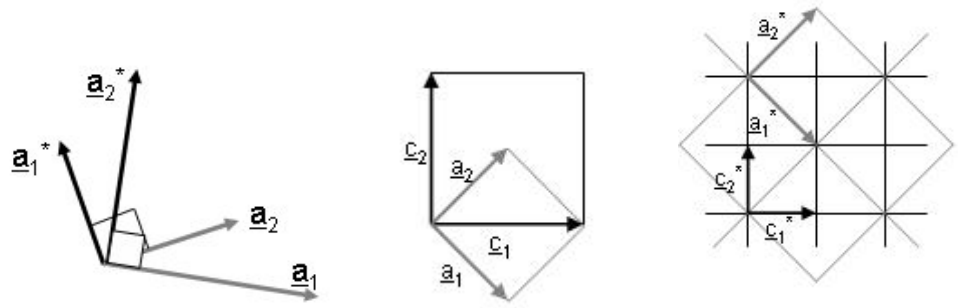

(a) Relationship between real vectors a_1 & a_2 and their reciprocal space counterparts a_1^* & a_2^*

(b) a structure in real space

(c) structure in fig(b) in reciprocal space

Figure 1.10 – Translation between real and reciprocal space for: (i) of a pair of vectors describing a unit mesh - (a), and (ii) a pair of unit mesh's including their relation to one another - (b) and (c).

are related by:

$$\underline{a}_1^* \times \underline{a}_1 = 1 \qquad \underline{a}_1^* \cdot \underline{a}_2 = 0$$
$$\underline{a}_2^* \times \underline{a}_2 = 1 \qquad \underline{a}_2^* \cdot \underline{a}_1 = 0$$

This means that $\underline{a}_x^*$ and $\underline{a}_x$ have a reciprocal relationship while $\underline{a}_x^*$ is $\perp$ to $\underline{a}_y$ and vice versa, see figure 1.10(a). These relations apply to all Bravais nets and allows us to swap freely between real and reciprocal space. In reciprocal space the smaller repeating pattern corresponds to the *c net* while the larger corresponds to the *a net*, see figure 1.10.

A RHEED diffraction pattern of a nearly flat reconstructed surface consists of bright streaks, corresponding to the bulk periodicity, intercalated by weaker, surface-related lines, see figure 1.6a. These fractional order periodic streaks correspond to the periodicity (with respect to the ideal bulk terminated surface) of the reconstructed surface in the viewing direction. RHEED used in MBE therefore, can provide fundamental information about surface geometry and chemistry, both in static and dynamic conditions.

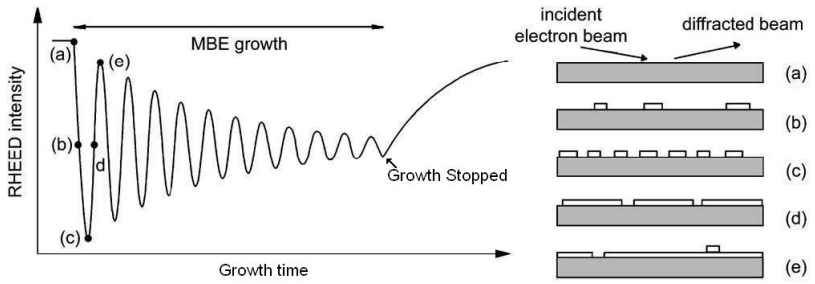

Figure 1.11 – Different stages of layer-by-layer growth by nucleation of 2D islands and the corresponding intensity of the specular diffracted RHEED beam [19].

1.3.3 Determining growth rates

As well as determining information on surface roughness and reconstruction, RHEED can also be used to determine growth rates. On starting growth, the intensity of features on a RHEED pattern can be seen to oscillate. These oscillations are damped as growth progresses and in most cases, on stopping growth, the intensity of each feature almost returns to its initial value, see figure 1.11. The observation of so-called RHEED oscillations was first reported by Harris et al. in 1981 [23]. They established two key points: first that the period of the oscillations corresponded to the time taken to deposit a single monolayer of material and second, that the period did not depend on growth temperature.

The oscillations can be qualitatively explained by relating them to the presence of 2D islands on the growing surface. The islands are assumed to be one monolayer high and thus, much higher than the wavelength of the beam electrons. The island edges (steps) behave as scattering centers that reduce the intensity of the beam diffracted in the Bragg directions. With reference to figure 1.11, at the start of growth (a), the density of 2D islands, and hence steps, increases until it reaches a maximum value and the diffracted intensity displays a minimum, (c). Islands then start to coalesce, reducing the step density (d), and so the diffracted beam intensity increases until it reaches a maximum value corresponding to a complete surface coverage (e). The process then repeats. Of course this model is only valid for 2D growth.

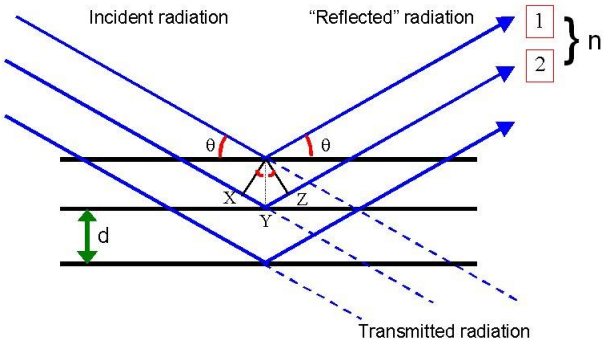

Figure 1.12 – Diffraction of a plane wave off successive planes of a crystal structure, Strong diffraction results when the angle of incidence, θ to equal that of diffraction and the path difference XYZ between the two beams is equal to $n\lambda$, leading to Bragg's law.

1.4 X-Ray Diffraction (XRD)

XRD is a powerful bulk characterization technique which is highly sensitive to crystal structure. High resolution XRD allows for rapid, non-destructive qualitative and quantitative analysis of highly ordered materials.

1.4.1 Theory

An X-rays wavelength, of a few Å, is comparable to interatomic distances and so an incident X-ray beam is scattered by individual atoms in all directions. In randomly distributed atoms, such as those in a monoatomic gas, scattered rays will have a random phase relationship relative to one another and neither full constructive, nor destructive, interference will occur. In a crystal where atoms are arranged periodically on a lattice, scattered beams will have definite phase relationships. These phase relations are such that, in most directions, destructive interference occurs giving almost zero intensity. In a few directions the scattered beams will be completely in phase and so, constructively interfere to form diffracted beams.

These diffracted beam directions are those that satisfy Bragg's law, equation 2, arguably the simplest and most familiar description of crystal diffraction. It can be understood by considering entire crystal planes as the scattering entity, rather than the individual scattering centers within the plane. Strong diffraction occurs when

$$\lambda = 2d_{hkl}sin\theta \tag{1.2}$$

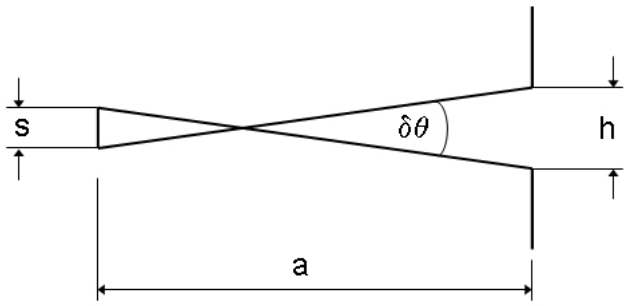

Figure 1.13 – The divergence, $\delta\theta$, of a single-axis system, where h is the source size, s is the slit size and a is the distance between source and specimen; figure adapted from Bowen and Tanner [24].

where n is an integer representing the order of diffraction, λ is the wavelength of the incoming radiation, d is the interplanar spacing and θ the angle of incidence, and diffraction, of the radiation given relative to the reflecting plane. See figure 1.12.

The Bragg law is simply a consequence of the periodicity of the lattice and makes no reference to the arrangement of atoms in the basis associated with each lattice point. In this way, the Bragg law merely represents the minimum condition for diffraction of X-rays by a set of parallel planes. The amount of radiation reflected, if any, when the Bragg condition is met depends on the structure factor; a mathematical description of how the crystal scatters incident radiation. This essentially determines the scattering at a given angle by multiplying the scattering strength of (i) an electron or nucleus, (ii) an atom, (iii) a unit cell and (iv) the total number of unit cells, all with regard to the direction of scattering and the relative phase of the scattered waves. The phases may add up or cancel, hence some reflections are not seen.

1.4.2 High resolution XRD or Double-axis diffractometry

In a real crystal, for a given plane and wavelength, diffraction takes place over a small finite range, rather than the zero angular range defined by the Bragg law. This angular range is known as a crystal's rocking curve width and can be used to assess material quality.

A single-axis diffractometer utilises a beam far from a plane wave thus, single-crystal rocking curves are broadened due to the beam divergence and spectral

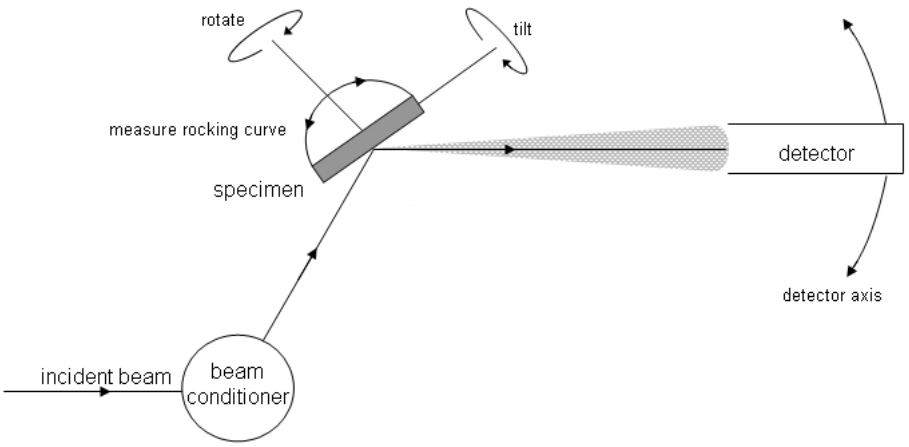

Figure 1.14 – Schematic of a high-resolution or double-axis instrument. Figure adapted from [24].

width of the X-rays. Divergence, $\delta\theta$, see figure 1.13, is a function of source size, h, slit size, s and source-specimen distance, a and is given by

$$\delta\theta = \frac{h+s}{a} \tag{1.3}$$

In a typical system, the divergence of characteristic X-rays far exceeds the rocking curve width for highly perfect crystals; 500 arc seconds cf. a few arc seconds respectively. The spectral width of X-ray characteristic lines is approximately $\delta\lambda/\lambda \sim 10^{-4}$, rising to 10^{-3} if both $K_{\alpha 1}$ and $K_{\alpha 2}$ lines are diffracted by the specimen.

In order to reduce the divergence and wavelength spread of an X-ray beam incident on a sample, beam conditioners are used. Placed between the X-ray source and the specimen, these act to collimate and monochromate the beam through a combination of diffracting elements and angular-limiting apertures; the latter also being able to control the spatial width of the beam. The specimen is carried on an axis that may be tilted to a precision of at least 1 arc second. The diffracted beam then enters a detector, which accepts all X-rays scattered off the specimen.

This is the basic high-resolution, or double-axis, setup, which is now widely used for measurements of epilayer composition, strain, thickness and crystal perfection. A schematic of a typical double-axis instrument is shown in figure 1.14. The first axis refers to the fact that the beam conditioners can be adjusted, while the second

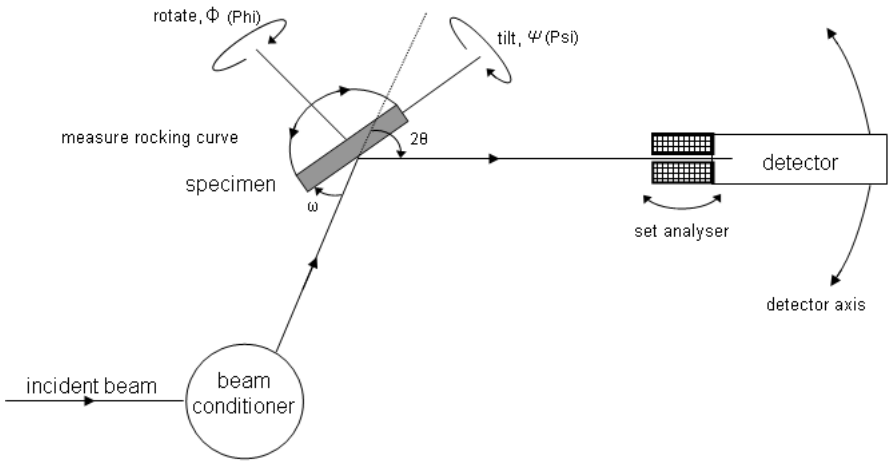

Figure 1.15 – Schematic of a high resolution triple-axis instrument. Figure adapted from Bowen and Tanner [24].

refers to the scan of the specimen though the Bragg angle. It is irrelevant to this definition that a practical diffractometer may contain a dozen or more controlled axei: for example, to tune and align the beam conditioner, to locate the specimen in the beam, to align and scan the specimen and to control slits.

What makes rocking curve measurements so powerful is that

1. The details of the rocking curve are extremely sensitive to strain and strain gradients in the specimen.
2. For a given structural model, the rocking curve may be computed to high accuracy, using fundamental X-ray scattering theory.
3. Measurements are rapid and simple.

Table 1.1 shows the information that can be obtained from rocking curves measured by high-resolution XRD, HR-XRD (and triple-axis diffractometry).

1.4.3 Triple-axis diffractometry

In the double-axis diffractometer, the detector integrates the intensity scattered by the specimen, over its acceptance angle. While this is relatively quick and convenient it can lose information in particular, scattering from bent or mosaic

Material parameter	Effect on rocking curve	Distinguishing features
Mismatch	Splitting of layer and substrate peak	Invariant with sample rotation
Mis-orientation	Splitting of layer and substrate peak	Changes sign with sample rotation
Dislocation content	Broadens peak	Broadening invariant with beam size No shift of peak with beam position on sample
Mosaic spread	Broadens peak	Broadening may increase with beam size, up to mosaic cell size. No shift of peak with beam position on sample
Curvature	Broadens peak	Broadening increases linearly with beam size Peak shifts systematically with beam position on sample.
Relaxation	Changes splitting	Different effect on symmetrical and asymmetrical reflections
Thickness	Affects intensity of peak	Integrated intensity increases with layer thickness, up to a limit
	Introduces interference fringes	Fringe period controlled by thickness
Inhomogeneity	Effects vary with position on sample	Individual characteristics may be mapped

Table 1.1 – The effect of substrate and epilayer parameters upon the rocking curve

crystals. Details such as thickness fringes or narrow peaks can also be lost or blurred. More detailed information can be obtained by placing an analyser crystal between the specimen and the detector, this restricts angular acceptance but at the expense of intensity. The analyser component is mounted on an axis concentric with the specimen and is scanned independently of the sample. This set-up is the triple-axis diffractometer, see figure 1.15, where the three axes refer to those controlling the beam conditioner (and hence the input beam), the specimen and the analyser. It is a quirk of history that it is the double-axes setup which is known as the high-resolution diffractometer and not the triple-axes.

A map of the scattering as both the specimen and analyzer are rotated (known as a reciprocal space map, RSM) can be measured. This enables the distinction of diffraction from different sources; for example, scattering due to defects occur in a different direction in space than scattering from the perfect crystal. More importantly, strain or mismatch may be distinguished from tilt or mosaic spread. To see how reciprocal space relates to the $2\theta/\omega$ and ω scans performed see figure 1.16. RSMs have axes Qx and Qy which have units of reciprocal lattice units (rlu) which are proportional to $1/d$. The following equations give the relationship between the Qx (x axis in RSM) and Qy (y axis in RSM) values in reciprocal space and the diffractometer angles ω and 2θ:

$$Qx = R\left[cos\omega - cos\left(2\theta/\omega\right)\right] \tag{1.4}$$

$$Qy = R\left[sin\omega + sin\left(2\theta/\omega\right)\right] \tag{1.5}$$

where R is the radius of the Ewald sphere.

1.4.4 PANalytical X'Pert Materials Research Diffractometer

The diffractometer used for the XRD work described in this report is a PANalytical (Philips) X'Pert Materials Research Diffractometer. It is equipped with a copper tube X-ray source, primary optics (beam conditioner) which consist of an X-ray mirror, 0.02 radian soller slits, to reduce divergence of the beam in the y direction, and a four bounce Ge(220) monochromator in order to create a parallel $K_{\alpha 1}$ beam of wavelength 0.154056 nm, with an equatorial x divergence of <12".

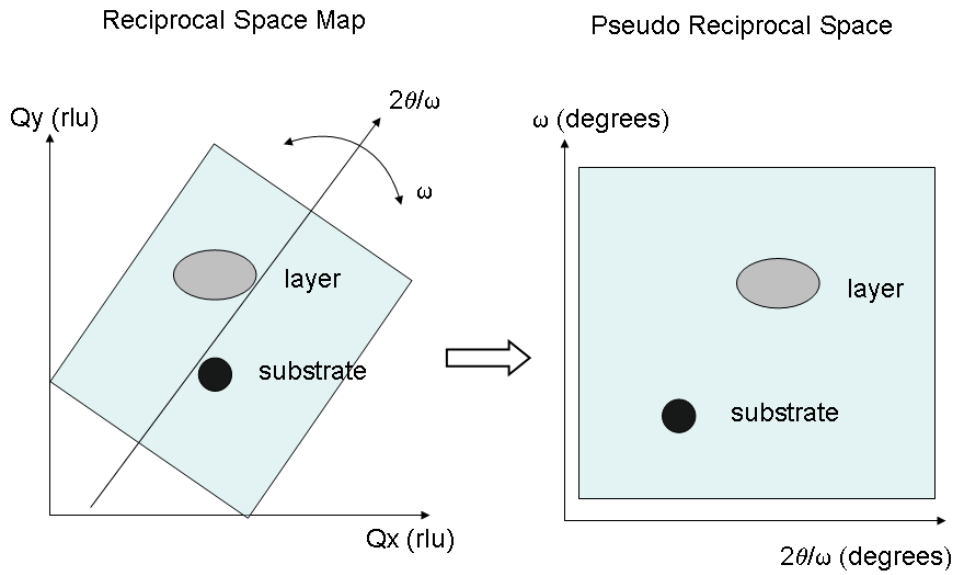

Figure 1.16 – Simple schematic showing how a $2\theta/\omega$ scans as a function of ω converts to reciprocal space with reciprocal space unit vectors of reciprocal lattice units (rlu) and axes Qx and Qy.

The X'Pert system contains both a high-resolution and a triple-axis detector, known as the upper and lower detectors respectively. The high-resolution detector is an open detector, while the triple-axis detector has a triple bounce Ge(220) analyser placed in front of it with a 12" acceptance. A third option is the use of the high-resolution detector with a slit placed in front, to give a pseudo RSM.

The sample stage is a precision goniometer; angles associated with the movements of the goniometer are shown in figure 1.15. The following resolutions are achievable in the X'Pert system: 0.01° for ϕ (tilt- rotation about an axis lying in the plane of the sample) and ψ (twist- rotation about an axis perpendicular to the plane of the sample), and 0.0001° for ω (angle between the incident beam and the sample surface) and 2θ (angle between the incident beam and the diffracted beam). In practice, these resolutions are limited by the specimen and in reality the highest sensible resolution for ω and 2θ is 0.0003°.

The fitting software used to simulate rocking curves is PANalytical X'Pert Epitaxy 4.1, which is based on dynamical theory, details of which can be found in *X-ray scattering from semiconductors* [25].

The X'Pert system was used in this work to obtain the following:

1. $2\theta/\omega$ linescans - measure peak position to identify phase and crystallinity of

material present, assess composition of alloys, determine lattice parameter (in direction perpendicular to the surface).

2. ω linescans - FWHM as a measure of material quality.

3. RSMs - assess strain of grown material with respect to the substrate, assess material quality.

4. partial pole plots (scans of ψ as a function of ϕ, further information below) - determine symmetry, degree of twinning and detect diffraction originating from small volumes e.g. identify very small amounts of additional phases present.

Pole plots (pole figures/texture measurements) are generally used to determine the orientation distribution of crystalline grains in a polycrystalline sample. A pole plot is measured at a fixed scattering angle (i.e. fix 2θ and ω to ensure a constant d spacing) and consists of a series of ϕ scans (in plane rotation of the sample) at different tilt or ψ (azimuth) angles. This is good for detecting diffraction from peaks that result in low intensities, especially where the tilt relation to the substrate is unknown. As the ϕ scan is normally over 360°, the symmetry related to diffraction peak can also be determined. This can be useful to assess whether there is twinning present within a sample and to identify material responsible for the diffraction peak (e.g. if both cubic and hexagonal polytypes of a material result in diffraction at the same 2θ angle).

1.5 Atomic Force Microscopy (AFM)

Atomic force microscopy (AFM) is a technique [26] used for imaging and measuring a surface on a nanometre scale in air. It has been used primarily in this work to calculate surface roughness as a means of assessing material quality, in order to gauge the success of different growth tactics.

The principle of a basic AFM setup is relatively simple. A cantilever with a sharp tip (radius of curvature of a tens of nm) is scanned laterally over a surface. Forces due to interaction with the surface (typically van der Waals forces) lead to deflection of the tip. The amount that the tip moves vertically is generally measured using the reflection of a laser beam, from the back of the cantilever,

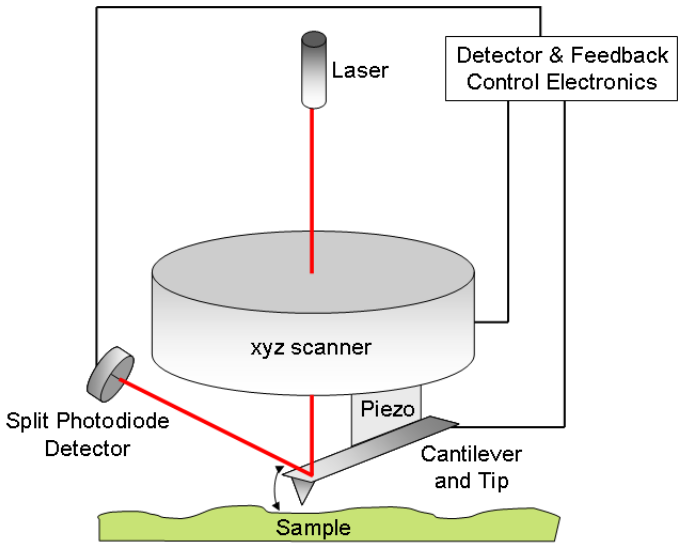

Figure 1.17 – Schematic of a typical atomic force microscopy (AFM) setup.

onto a split photodiode. The cm scale optical path of the laser beam serves to amplify the bending of the cantilever, allowing sensitivities down to Angstrom-level. Feedback mechanisms utilise the photodiode signal to control the movement of the piezo scanner in the x, y and z directions. Scanning the tip at a constant height could lead to the tip crashing into the surface, so a common method of feedback is to ensure the tip remains a constant vertical distance from the surface. The movement required to maintain a constant separation between tip and sample surface is taken as the sample topography; this is an example of a static imaging mode.

In the work presented in this thesis, the AFM was operated in tapping mode (a dynamic imaging mode). In this mode the cantilever is oscillated at, or near, the cantilever's resonant frequency, using a piezoelectric crystal. The tip is brought in close proximity with the sample where it periodically makes contact with (or 'taps') the surface. Interaction with the surface during contact leads to a dampening of the oscillation amplitude. Feedback mechanisms are employed to adjust the height of the cantilever in order to maintain a constant oscillation amplitude as it is scanned across the surface. This imaging mode has the advantage over the constant distance technique in that the tip is prevented from sticking to, and thereby damaging, the surface. Images are typically produced depicting an area ranging from 1 μm by 1 μm up to 50 μm by 50 μm.

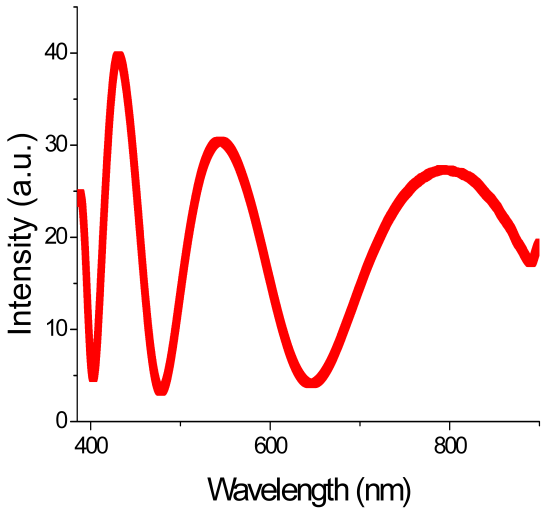

Figure 1.18 – Optical reflectance spectrum from a 250nm GaN layer grown on a GaAs substrate.

1.6 Optical Reflectance Studies (ORS)

The spectral optical reflectance of all samples has been studied in a wavelength range of 300-900 nm, see figure 1.18 for a example spectrum. The set-up consists of a white light source, which is directed at a sample, and a solid-state spectrometer, which analyses the light reflected from the sample. Computer software compares the signal with the reflected signal of a mirror surface, to produce a reflectance (or absorption) spectrum. Changes in reflectance have enabled the determination of a material's bandgap, whilst measuring the period of Fabry-Pérot oscillations has, in some cases, been used to measure a material's thickness.

Fabry-Pérot oscillations can occur in materials which consist of layers of differing refractive indices. Waves incident on multilayer media can reflect at each interface, giving rise to beams that have undergone multiple reflections, see figure 1.19. This enables constructive and deconstructive interference to occur. For example, if the transmitted beams are out-of-phase, destructive interference occurs. The minimum interference on reflection spectra occurs for $2n(\lambda)d = m\lambda$, while constructive interference conditions are met when $2n(\lambda)d = m + 0.5\lambda$, where $n(\lambda)$ is the refractive index of first encountered layer, d is the thickness of the layer, m is an integer and λ is the wavelength of incident light. For optical wavelengths, $n(\lambda)$ is approximately constant. These relationships allow for simple extraction of

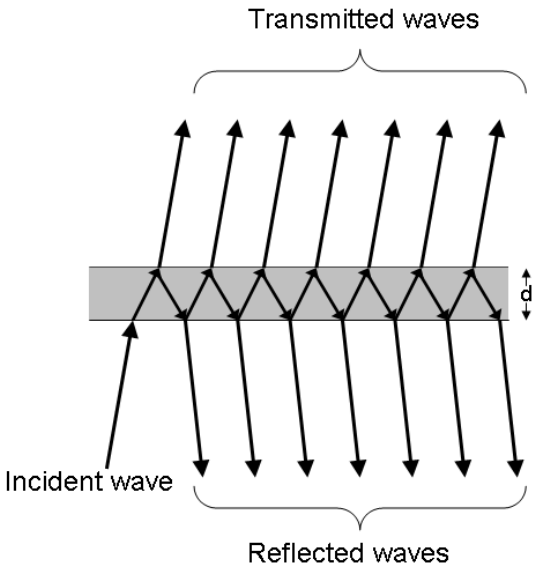

Figure 1.19 – Multiple Fabry-Pérot reflections in a thin film of thickness d.

layer's thickness from the reflectance spectra of simple bilayer structures.

1.7 Transmission Electron Microscopy (TEM)

Transmission electron microscopy (TEM) [27] has been performed on scandium containing samples (Chapter 4) by the materials science and metallurgy department at the University of Cambridge, as part of a joint project. The primary goal of this work was to assess the effects of ScN interlayers on the defect density of cubic GaN.

In the typical TEM (see figure 1.20) mode of bright field imaging, a thin sample is bombarded with electrons. A contrast image is then formed by the collection of transmitted electrons. Thicker parts of the sample and areas with a higher atomic number will appear darker, due to the absorption and scattering of electrons. Structural imperfections in a sample will also lead to a change in the intensity of transmitted electrons. The image formed is effectively an enlarged image of the sample. It is analogous to an optical microscope, but with resolution limited by the wavelength of an electron as opposed to a photon.

Electrons can also be scattered by the sample, which can lead to diffraction of electrons in the back focal plane. The use of apertures and the ability to tilt

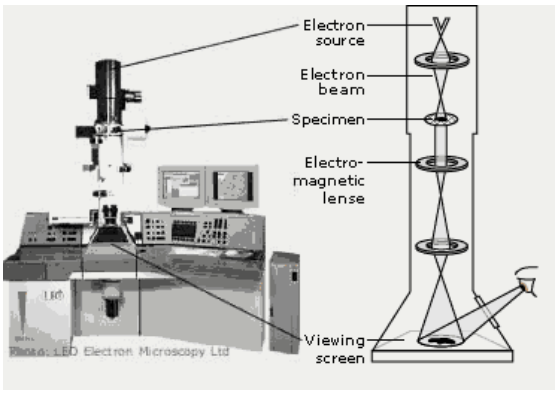

Figure 1.20 – Schematic of a typical transmission electron microscope (TEM) setup. Taken from nobelprize.org

the sample allows diffraction from different Bragg reflections to be selected and viewed. If there is no scattering at the selected conditions the image will appear dark, this is therefore known as a dark field imaging mode.

1.8 SQUID

Magnetic studies have been performed using a Quantum Design Magnetic Properties Measurement System (MPMS) superconducting quantum interference device (SQUID) magnetometer [28]. This work has been undertaken by Dr. A. Rushforth at the University of Nottingham, in order to determine the nature of magnetism in samples e.g. paramagnetic, ferromagnetic etc. and for GaMnAs samples, their Curie temperature [29].

The SQUID measures the total magnetic moment of a sample along a given direction and can operate in the temperature range of 2-400K, with an applied external field of up to ± 1 T.

1.9 EXAFS/XANES

In order to investigate the local bonding of atoms of polycrystalline GaAs grown at low temperatures (Chapter 2) EXAFS (extended X-ray absorption fine structure) and XANES (X-ray absorption near edge structure) measurements were performed.

EXAFS and XANES fall under the category of X-ray absorption whereby X-rays (as a function of energy) are directed at a material. On interaction with a sample, electrons are knocked out of an atom when the energy value of incident X-rays exceeds the ionisation threshold (edge energy/absorption edge). Analysis of the spectrum close to the absorption edge of an element of interest is then undertaken.

EXAFS is the oscillating part of the X-ray absorption spectrum that extends to about 1000 eV above an absorption edge of a particular element. The interference of these outgoing photoelectrons with the scattered waves from atoms surrounding the central atom causes EXAFS. The regions of constructive and destructive interference are respectively seen as local maxima and minima giving rise to the oscillations in EXAFS. EXAFS gives us information about

1. Distances between central and neighboring atoms.
2. The number of neighboring atoms.
3. The nature of neighboring atoms (their approximate atomic number)
4. Changes in central-atom coordination with changes in experimental conditions

The main advantage of EXAFS analysis over X-ray crystallography is that structures can be studied in non-crystalline forms (including liquid and frozen solutions).

When the energy range under inspection is extended to beyond 5 eV from the absorption edge the technique is called XANES. In EXAFS the photoelectron is scattered only by a single neighbour atom, whereas in XANES all the scattering pathways, contribute to the absorption cross section. XANES is often used in conjunction with EXAFS to provide complimentary information. Its key advantage over EXAFS is that it provides more information regarding the valence state of atoms, e.g. is able to distinguish between subtle distortions of two atoms with the same bonding co-ordination. An illustration highlighting the energy difference in the X-ray absorption edge between EXAFS and XANES is shown in figure 1.21

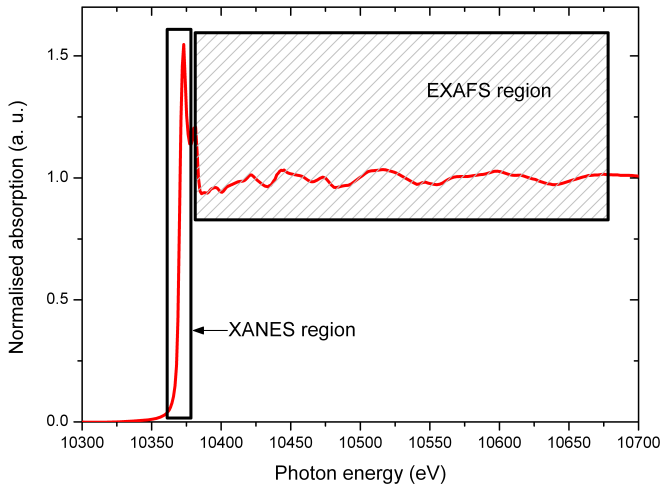

Figure 1.21 – X-ray absorption of a elements at energies near to the absorption edge, showing division into XANES and EXAFS regions.

1.10 SIMS

Secondary ion mass spectroscopy (SIMS) is a technique used to obtain compositional information about a material, as a function of thickness. It is a destructive technique (but with high sensitivity) that involves the bombardment of a surface with focused ions e.g. Cs. Resultant (secondary) ions are effectively sputtered from the surface. A mass spectrometer is then employed to analayse the mass ratio of the sputtered species and hence determine the elements present in the original material. It does not however, provide any information about an elements bonding arrangement. If the sputtering rate is known, then the distribution of elements can be directly related to their depth.

Chapter 2

Growth of GaAs at Low Temperatures

2.1 Background

Theoretical thermodynamic studies by Don Hurle of native point defects in zinc blende III-V semiconductors, suggest that GaAs should undergo a phase transition when grown at low temperatures (<200 °C) under slightly As-rich conditions [30]. This expected phase transition is driven by the coulombic attraction of high numbers of ionised As antisites and Ga vacancies, that are predicted to be present at low temperatures along the As-rich solidus. The high-concentration of said defects comes about due to an increase in the solubility of As antisites with falling temperature, owing to enhancement from Ga vacancy defects. It is believed that, in zinc blende III-V semiconductors this catastrophic number of defects at low temperatures is unique to GaAs; e.g. in GaSb, the Ga antisite defect concentration falls with decreasing temperature [31].

Semiconductors, including GaAs, are known to exist in different polytypes. GaAs phase transitions however, have only been reported in powders treated under high pressures; typically >15 GPa [32,33]. The electronic properties of pressure-induced phases are markedly different to their usual forms, but many of the intrinsic characteristics of these unusual polytypes have not been investigated. In order to exploit any properties displayed by new forms of GaAs, they will need to be in the form of thin films, which are stable under ambient conditions. This will en-

able easy incorporation into existing technology, where GaAs wafers and layers are already integrated into microelectronic technology.

At conventional growth temperatures (∼580°C), single crystal GaAs grows epitaxially on the substrate (normally GaAs). At low growth temperatures (∼150°C) however, GaAs is known to grow in a polycrystalline manner [34]. It is proposed that this may actually represent a transition from growing in a zinc blende to a rock-salt structure [35].

2.2 MBE Growth

2.2.1 Growth details

A initial set of six low-temperature (LT) GaAs samples were grown on semi-insulating GaAs(0 0 1) wafers at various temperatures. Wafers were initially de-oxidised in the presence of As at a temperature of 640 °C. A 300 nm undoped GaAs buffer layer was first grown at ∼580 °C, in order to smooth the surface. Growth was interrupted and temperature lowered and allowed to stabilise before the growth of a 500 nm LT GaAs layer, with the exception of JH06 for which a 1μm layer was grown. The LT layer was grown under conditions which were ∼1% As-rich in a substrate temperature range from 135 to 210 °C.

Growth rates were determined prior to growth, by analysing the oscillations of the specularly reflected RHEED spot on a separate piece of GaAs wafer. Fluxes were adjusted, as required, to give a growth rate of 333 ± 2 nm/hr.

The temperature was recorded throughout by the BandiT. Due to exposure to heat from the cells, an increase in substrate temperature is expected upon starting growth. It was found however, that there was no consistent increase in temperature, meaning that it is not possible to pre-program automatic temperature control during growth of LT GaAs layers.

For the first sample, JH01, a temperature of at least 200 °C was chosen as it is known, and confirmed during growth by the RHEED pattern, that the growing structure of GaAs is of high crystal quality and zinc blende [36]. During the growth of JH03, it became evident that achieving growth temperatures of <200 °C, without intervention, would be unlikely. It appears that, at these low temperatures,

Sample	T_{start}	T_{final}	Thickness	Comments	R (Ω)
JH 01	200 °C	210 °C	0.5µm		N/A
JH 02	180 °C	200 °C	0.5µm		N/A
JH 03	170 °C	200 °C	0.5µm	Substrate heater off at 30mins, T stable at 145 °C	3-5 M
JH 04	145 °C	145 °C	0.5µm	Band Edge lost 50mins RHEED: Diffuse rings	6-8 M
JH 05	153 °C	180 °C	0.5µm	RHEED: Faceting	6-8 M
JH 06	140 °C	135 °C	1.0µm	Band Edge lost 50mins RHEED: Diffuse rings	6-8 M

Table 2.1 – Growth summary of LT GaAs samples JH01-06.

the primary source of substrate heating was due to exposure from the hot Ga and As cells, as opposed to the substrate heater; the substrate heater was found to draw negligible power during growth. Since another sample had already been grown at 200 °C, the heat contribution from the cells was investigated by switching the substrate heater power off. The growth temperature was found to stabilise at 145 °C. A transition in the RHEED pattern from a 1x1 reconstruction to rings was observed, approximately 50 mins after switching the power off. This demonstrates that the growing surface was now polycrystalline and that 145 °C appears to be a growth temperature below the transition temperature.

In order to grow a LT GaAs layer at a stable temperature below 150 °C (JH04), the substrate temperature was set at ∼145 °C and upon starting growth, the substrate heater was turned off. It was found that it took approximately 10 mins for the temperature to stabilise having reached a maximum of value of ∼160 °C. JH05 represents a LT GaAs layer grown above the expected transition temperature of 150 °C, but below 200 °C, while JH06 is a repeat of JH04 (below transition temperature), but with a doubled thickness.

At temperatures below ∼300 °C, the familiar 2x4 surface reconstruction observed in the RHEED pattern is replaced by a 1x1 reconstruction, see figure 2.1(a). For growth temperatures of 200 °C or more, the 1x1 reconstruction was maintained throughout growth. For the growth of samples below 150 °C however, four different RHEED patterns are observed. The initial 1x1 reconstruction after 10 mins develops into an interesting faceting pattern, figure 2.1(b), which appears to be a precursor state to transition. At ∼30 mins, arcs start to appear, figure 2.1(c), with hints of the 1x1 pattern still present, suggesting that several orientations are

present in the sample. Over the course of 20 mins, a pattern consisting of faint rings with a diffuse background emerges, figure 2.1(d), showing that the growing sample is now fully polycrystalline with short range order. The sample grown at 180 °C, JH05, started to show faceting towards the end of the growth. This suggests that the sample was starting a transition, but that it had not fully taken place before growth was stopped. A summary of the major features of the growth of LT GaAs can also be found in table 2.1.

For samples that experienced a transition the band-edge, as recorded by the BandiT, was lost ∼50 mins later. This indicates that these samples are conducting, leading to measurement of each material's resistance. Only samples which displayed faceting in the RHEED were found to have a measurable resistance; in the region of a few MΩ. To ensure that this conductivity was related to the growth of LT GaAs, and not inherent to the GaAs substrate, the underside of the wafers were also tested; this produced no measurable readings in any of the samples.

It is worthwhile mentioning that if it were not for the use of the BandiT to monitor substrate temperature, problems with the growth temperature would not have been observed. It is feasible therefore, that temperatures low enough to witness a transition may not have been achieved.

2.2.2 XRD analysis

Initially, a Laue back reflection pattern was taken of sample JH04, measured by a Cu-target Phillips PW 1729/00 X-ray generator with a 20 kV and 40 mA configuration. It was hoped that rings relating to the LT layer could be observed and hence, a lattice parameter calculated. Only a single pattern was observed showing spots with a four-fold symmetry; representative of the zinc blende GaAs substrate. This suggests that there is not enough LT GaAs material to contribute to the pattern. Consequently, sample JH06 was grown, however up to 1µm of polycrystalline GaAs material was also insufficient to see any rings.

For HR-XRD analysis, 4 samples were compared: JH01, JH04, JH05 and JH06. These correspond to: one sample grown far above the transition temperature, one sample possibly starting a transition and two samples grown below the transition temperature. Since both the zinc blende and rock-salt structures are cubic, the same reflections are allowed. This means that a quick and easy method of structure

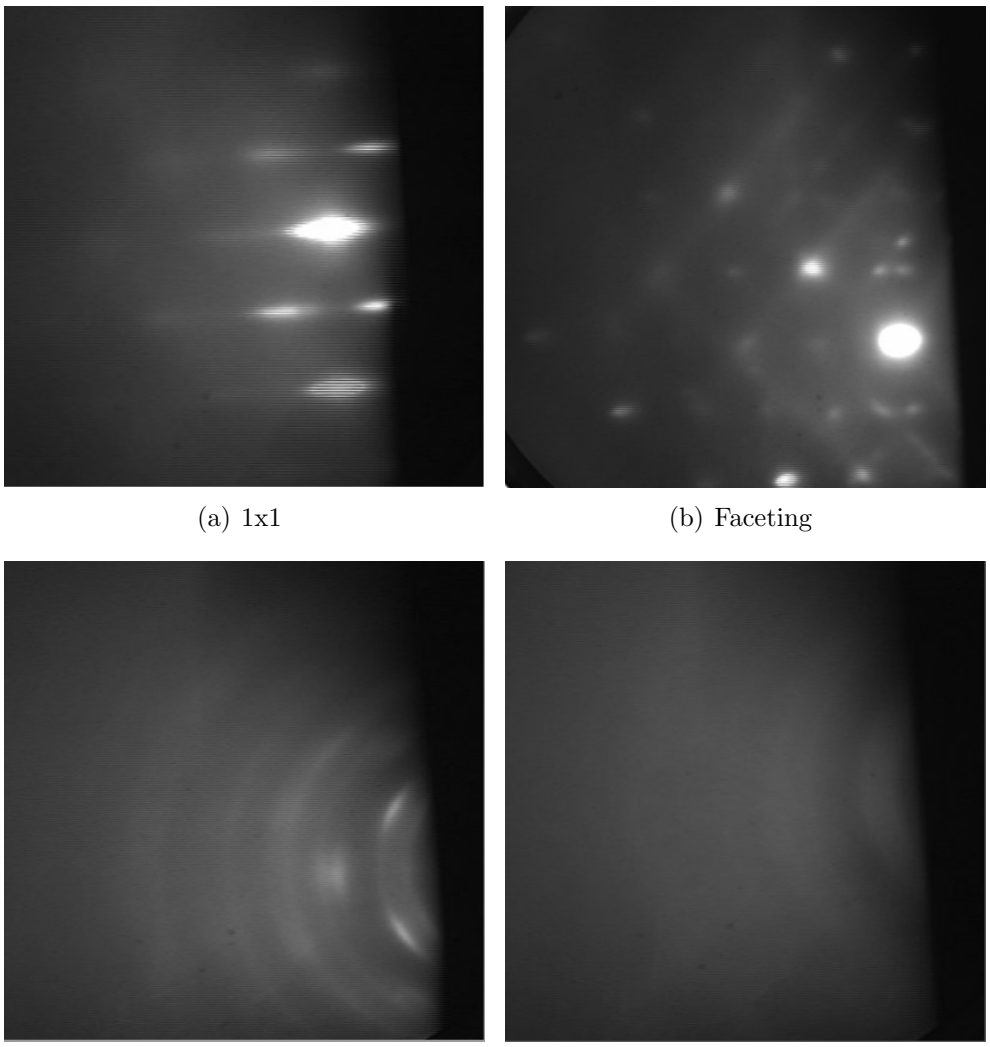

(a) 1x1 (b) Faceting

(c) Arcs (d) Diffuse rings†

Figure 2.1 – Various RHEED patterns observed during the growth of low-temperature GaAs, recorded at 12 keV primary beam energy. † For a clearer view of the faint rings, the reader is directed to a electronic version.

determination is not readily available from a simple inspection of a wide ranging $2\theta/\omega$ scan.

Symmetric 004 reflection $2\theta/\omega$ linescans were performed on each of the samples and results are presented in figures 2.2(a) and 2.2(b). Samples grown above 150 °C, figure 2.2(a), show two distinct peaks. The highest intensity peak corresponds to the GaAs substrate and includes contributions from the GaAs buffer layer. The lower intensity peak, on the LHS of the substrate peak, relates to the LT GaAs layer. These clear, separate peaks, present at a lower angle than the GaAs substrate, show that the LT GaAs layers have a larger lattice parameter than conventional GaAs. This is attributed to the incorporation of As_{Ga} antisite defects at low temperatures [37]. As expected, the GaAs grown at the lower of the two temperature shows a bigger difference in lattice parameter. Simulations yield increases in lattice constants of 0.0020 Å for the 210 °C grown sample and 0.0036 Å for the 185 °C sample with respect to the substrate; a_0(GaAs)= 5.65368 Å.

The clear interference fringes indicate that the material was epitaxially grown and that the interface between the buffer and LT GaAs layers is smooth and well defined. They also indicate that the LT GaAs layer has a different refractive index to the GaAs substrate. Analysis of the fringe separation gives thickness values of 0.50±0.02 μm for JH01 and 0.50±0.03 μm for JH05; in agreement with the thickness estimated from the known growth rate and growth time. These results show that the two samples are good quality crystalline material and possess a zinc blende structure, despite JH05 showing faceting during growth.

Figure 2.2(b) presents $2\theta/\omega$ 004 linescans of samples JH04 (145 °C, 0.5 μm) and JH06 (135 °C, 1.0 μm), which show no clear separate peak. Instead, the GaAs substrate peak is very broad and there appears to be a shoulder present on the low angle side of the GaAs substrate peak. These broad peaks with no fringes point to a more amorphous material, as confirmed by the RHEED patterns. In JH06, there is a possible peak to the shoulder. If this is taken as a peak position, since it is closer to the substrate position than JH01 and 05 LT GaAs peaks, it would indicate that polycrystalline LT GaAs has a smaller lattice constant than zinc blende LT GaAs; but both have larger lattice parameters than regular GaAs.

If a material is polycrystalline, i.e. present in all orientations, then reflections from all allowed planes are present. $2\theta/\omega$ linescans aligned on the 004 reflection were performed on all four samples over a 2θ range of 20-70° (results not presented).

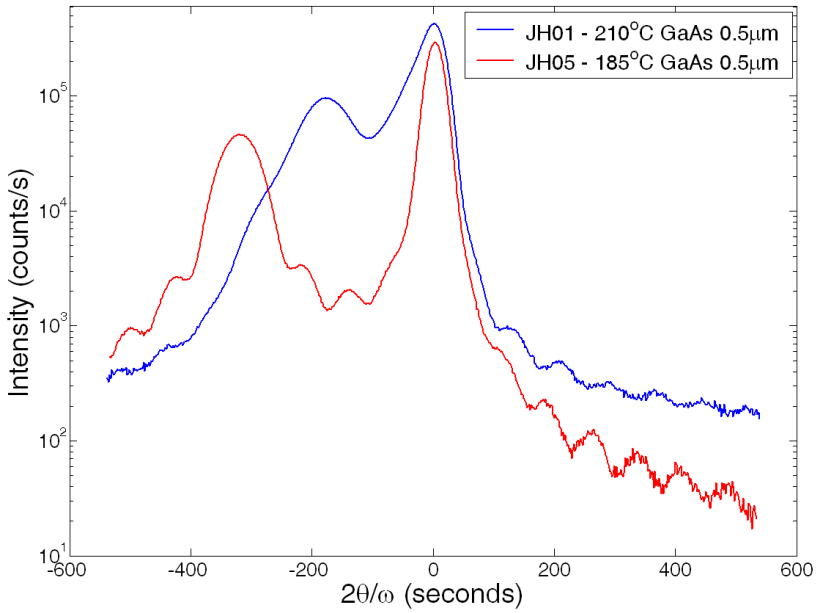

(a) LT GaAs grown above transition temperature

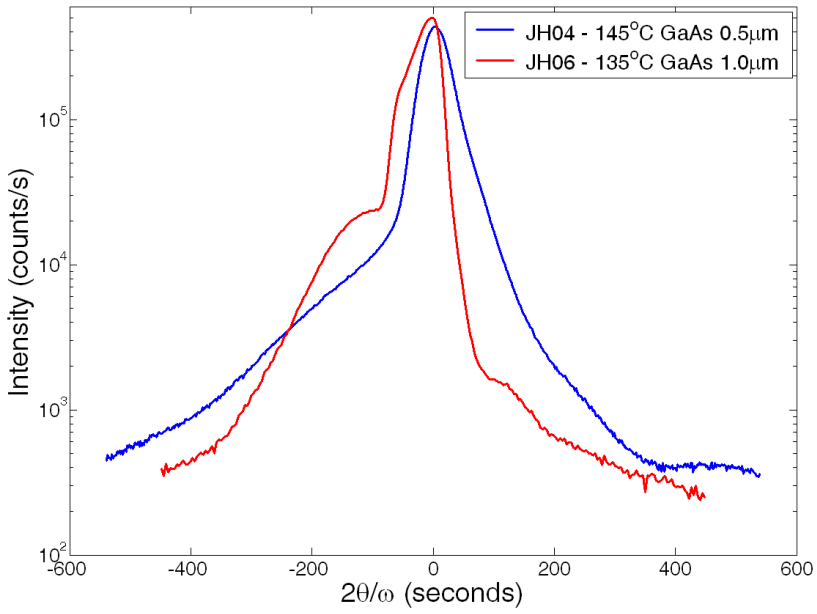

(b) LT GaAs grown below transition temperature

Figure 2.2 – Symmetric 004 reflection $\omega/2\theta$ linescans of low-temperature GaAs: grown at (a) 210 °C and 185 °C (1x1 RHEED pattern observed) and (b) 145 °C and 135 °C (transition to polycrystalline observed in RHEED pattern).

Only sample JH06 (135 °C, 1 μm) showed additional peaks, other than 002 and 004 reflections, but these were of very low intensity. Although this is evidence for long-range order arising from the polycrystalline GaAs material, the low peak intensities suggest the material is either largely amorphous or polycrystalline with limited short-range order. It would seem apparent that there is simply not enough structured material present in JH04 (145 °C, 0.5 μm) to produce significant peaks at other reflections. Given that the volume under a peak is a function of layer thickness and thin films cause peaks to broaden, this is not unreasonable. As expected, thickness fringes are not observed in the measurements of these two samples; if the material is polycrystalline then it has not been epitaxially grown.

Grazing incidence angle (0.2°) $2\theta/\omega$ linescans were also performed over a 2θ range of 20-70°(not shown), however these failed to give a reproducible lattice constant.

2.2.3 EXAFS studies

Diffraction is an assessment of long-range order, however since the lowest LT material is largely amorphous, the information that HR-XRD can provide is limited. While results indicate that the samples grown below the transition temperature are structurally different, they do not provide information as regards the detail.

In the zinc blende phase, each Ga atom is surrounded by four As atoms and vice versa, however in the rock-salt phase the co-ordination number would be increased to six. The predicted change in the number of nearest neighbours and the need to investigate short-range order, suggests that EXAFS (extended X-ray absorption fine structure) [38] would be a suitable method to confirm whether we witness a transition to the rock-salt polytype when GaAs is grown at ~ 150 °C. Since the atomic charge distribution in the two co-ordination environments is quite different, changes in the interatomic distances should be encountered. Additionally, as the site symmetry varies between four and six-fold, the K-edge XANES (X-ray absorption near edge structure) should also show marked differences between zinc blende and rock-salt structures.

For EXAFS analysis, new samples were grown using the same method outlined in section 2.2 and growth details for each sample are summarised in table 2.2. New growth was undertaken as (i) the material quality of the original samples has indications of degradation over time (as witnessed by increased mosacity from

Sample	Mean T	Thickness	RHEED	Comments	R (Ω)
JH 48	200 °C	500nm	1x1		-
JH 52	160 °C	275nm	Faceting	Growth stopped at start of transition	1.5M
JH 51	160 °C	500nm	Rings		800k
JH 54	160 °C	500nm	Rings	Si doped n^+ substrate	20k
JH 53	135 °C	500nm	Rings		1.3M
JH 49	120 °C	450nm	Rings		-

Table 2.2 – Growth summary of samples taken to the ESRF for EXAFS analysis.

XRD $2\theta/\omega$ linescans) and (ii) better temperature control had been established in the Gen III. Samples were measured on beamline BM08 at the ESRF, in the surface sensitive total electron yield mode at normal incidence. In this configuration electrons have an escape depth of <100 nm, ensuring any signal received originates from LT GaAs layer. Measurements were performed by Dr N Farley and Dr K Edmonds from the University of Nottingham's spintronic group and Dr. F d'Acapito from Grenoble.

Spectra were measured at both the Ga and As K-edge to provide complementary structural information, as shown in figures 2.3 and 2.4 respectively. The edge shapes from all samples are very similar in figure 2.3, with possibly the exception of JH49 which shows very broadened/smeared features which are attributed to disorder. These results therefore, indicate that all samples share the same site symmetry. All of the polycrystalline samples exhibit some broadening. This is more apparent in the full absorption spectra, figure 2.4, which shows increasing smearing of features with decreasing temperature.

The data were fitted with a zinc blende GaAs model and two rock-salt models[1]; one with a identical lattice parameter to conventional GaAs and one with a 15% larger lattice parameter (representing a predicted increase of cell volume, resulting from a change in first co-ordination number from 4 to 6). Fitted variables were the difference of interatomic distance between data and model (ΔR) and the Debye-Waller factor (σ^2, the mean squared displacement of interatomic distance i.e. a measure of structure disorder [39]).

Fitting results (see appendix B) show that disorder increases with decreasing growth temperature, which agrees with observations of spectral broadening. In all

[1]Models were constructed from crystallographic structures calculated using Atoms software

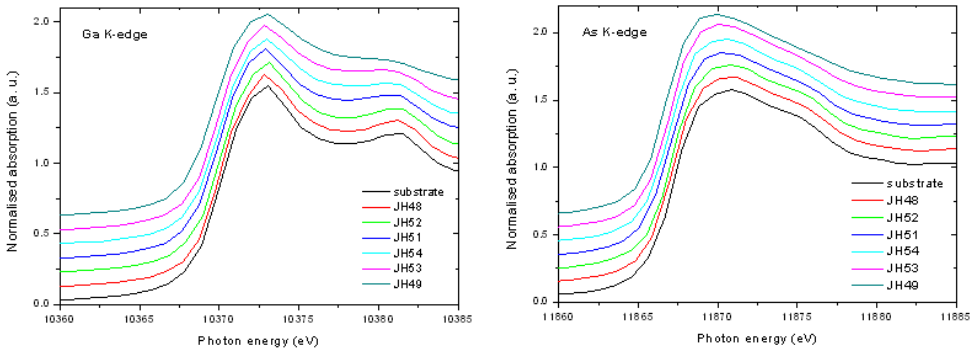

(a) Ga K edge (b) As K edge

Figure 2.3 – Absorption spectra of (i) Ga and (ii) As K edge (XANES) for LT GaAs samples grown at a variety of different temperatures and GaAs(100) substrate (as control). The spectra are plotted in order of growth temperature.

cases, the zinc blende model gives the best agreement with the results, and the larger lattice parameter rock-salt model (the more physically realistic of the two rock-salt models), the greatest disparity.

In summary, the structure of the samples are all very similar with the small differences that exist being caused by disorder. There is no evidence for the presence of rock-salt GaAs. The structure of the films vary from highly ordered to less ordered zinc blende, as a function of decreasing growth temperature and, to some extent, increasing thickness.

2.3 MEE Growth

2.3.1 Motivation

The EXAFS results ambiguously confirm that although the material is not necessarily deposited epitaxially, the structure of GaAs remains zinc blende when grown at temperatures down to 120 °C. The differing properties of LT GaAs, as compared with conventional GaAs have been attributed to incorporation of excess As into the lattice, which is known to increase with decreasing growth temperature; 0.1% for HT GaAs cf. up to 2% for LT GaAs [40]. In order to grow single crystalline zinc blende material at temperatures far below 200 °C, a method is required that allows excess As to evaporate from the surface during the growth

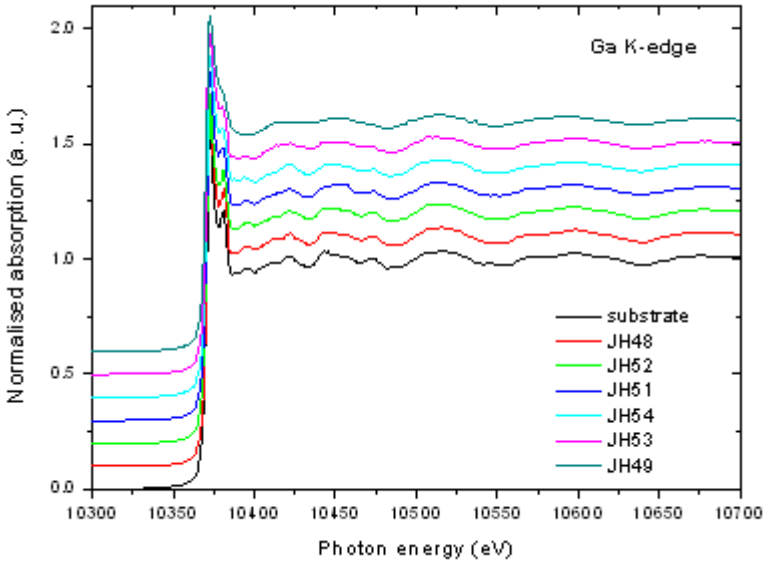

(a) Ga K edge

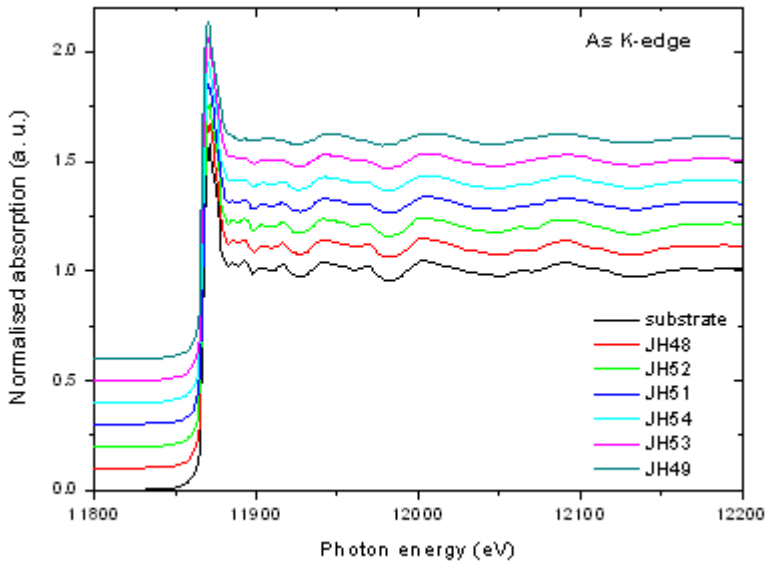

(b) As K edge

Figure 2.4 – Extended absorption spectra of (i) Ga and (ii) As K edge (EXAFS) for LT GaAs samples grown at a variety of different temperatures and GaAs(100) substrate (as control). The spectra are plotted in order of growth temperature.

process.

A way of achieving this would be to grow LT GaAs, not using the normal MBE technique (whereby all appropriate shutters are opened simultaneously), but using migration enhanced epitaxy (MEE). This method of crystal deposition involves the alternate opening of shutters. For a review of the technique the reader is referred to Horikoshi (1993) [41]. Applied to growth of GaAs, MEE could mean switching between monolayer deposition of Ga and As, with periodic growth interruptions. This would allow complete desorption of excess As from the surface during growth preserving stoichiometry and as such, permit a lower temperature limit for obtaining single crystalline GaAs. The thickness of the deposited film is determined by the Ga deposition time. Epitaxial growth of GaAs using this method has been reported for temperatures as low as 75 °C [42], although the structural properties were not discussed and the method of temperature determination was pyrometry.

If good quality LT GaAs can be obtained, then a useful application would be in the growth of GaMnAs. Mn-doped GaAs is the archetypal ferromagnetic semiconductor material, which is of particular relevance to spintronic research. This area aims to develop successors to Si-based storage and processing components by combining the charge-based properties of semiconductors with those of non-volatile magnetic recording media. Although it is predicted that GaMnAs should exhibit a Curie temperature (temperature beyond which a material stops exhibiting ferromagnetic behaviour) above room temperature [43], the current record Curie temperature is only $\sim$ 185K [1].

The Curie temperature is dependent on both the Mn content and hole concentration, as it is the interaction between hole spin and local moment on the Mn ions that leads to ferromagnetism. Due to the solubility limit of Mn, low growth temperatures are required in order to avoid Mn segregation. This in turn however, leads to the incorporation of As antisite defects, leading to a degradation of the host material's quality. The formation of Mn interstitials with increasing [Mn] is also a problem. Both the As antisite and interstitial Mn defects are double donors and thus, compensate the effects of substitutional Mn, which is responsible for the ferromagnetism. In order to further increase the Curie temperature of GaMnAs, larger mole fractions of Mn are desired, requiring growth at ever lower temperatures. The current highest Tc of 185K was obtained using a nominal [Mn] of 12% at a growth temperature of 200 °C. As well as growth temperature, the As over-

Sample	Material	T	RHEED	R (Ω)
JH 175	GaAs 333nm MBE	120 °C	Rings	1.6M
JH 176	GaAs 200nm MEE	113 °C	1x1 Spotty	1.5M
JH 177	GaMnAs 10.8nm MEE	115 °C	Amorphous	14M
JH 178	GaMnAs 12.5nm MEE	150 °C	1x2	50k

Table 2.3 – Growth summary of samples investigating MEE growth of LT GaAs.

pressure has also been found to influence [Mn] and Tc, meaning close attention has to be paid to achieving growth near stoichiometric conditions. The inherent properties of MEE should therefore be doubly conducive to achieving better quality GaMnAs material, both through allowing lower temperatures to be attained (and still produce good-quality material) and achieving stoichiometric conditions more easily.

2.3.2 Growth details

To investigate the structural effects of MEE growth on LT GaAs four samples were grown: a thick MBE grown GaAs control sample at 120 °C (JH175), a thick MEE GaAs sample at 115 °C (JH176) and two thin (∼12 nm) MEE GaMnAs films, one at 115 °C (JH177) and the other at 150 °C (JH178). Each sample was prepared for the LT layer using conditions described in section 2.2. The LT layer itself was grown under nominally stoichiometric conditions. For the GaMnAs sample a Mn flux was chosen to give a nominal concentration of 12% and so accordingly, the Ga flux was reduced from that calculated for stoichiometry for GaAs growth by 12%. The growth temperature (GT) during the LT layer was held at a constant value (±1 °C) through a combination of temperature down ramps on the substrate heater and manual control of the power supplied to the BandiT lamp. For the MEE grown layers, shutter control was automated to produce the following repeating sequence: 1½ secs (½ ML) Ga (+ Mn), 1 sec pause, 1½ secs As, 1 sec pause. The pause after the Ga exposure is designed to give the adsorbed Ga sufficient time to diffuse and hopefully, result in smoother surfaces. The pause after the As exposure is allow time for excess As to evaporate off the surface.

As expected, the GaAs sample grown by MBE at 120 °C showed a transition in the RHEED during growth, from a 1x1 reconstruction to hints of polycrystalline diffuse rings, figure 2.5(a). Faceting (the pre-cursor to polycrystallinity) had occurred by 25 mins while the transition to diffuse rings was complete by 35 mins.

The MEE GaAs grown sample (at approximately the same growth temperature) on the other hand, maintained a lattice rod pattern throughout (figure 2.5(b)), indicative of single crystalline material. It was found that while the MBE grown sample required significant and prolonged manual temperature control, the MEE grown samples did not. This is attributed to the fact that the Ga source is only exposed to the surface for a fraction of the growth time. In addition, if fewer defects are incorporated into the growing structure, then the number of free carriers is reduced with respect to MBE grown GaAs.

The first attempt at growing a LT GaMnAs (defined as below 200 °C) resulted in an almost instant diffuse RHEED pattern with faceting (in this case characteristic of Mn segregation) and rings indicated at 3 mins (figure 2.5(c)); the growth was therefore stopped at this point. For the subsequent growth, a higher substrate temperature of 150 °C was chosen. The RHEED pattern throughout this growth run remained single crystalline with hints of a 2x reconstruction, figure 2.5(d). On leaving the vacuum of the machine, the resistance of each sample was measured, results along with summary of other growth details can be found in table 2.3. Only the final sample, JH178 shows a deviation from a value in MΩ range. This is an encouraging feature as a conducting sample suggests that sample has been doped with holes. Predictions based on these resistance measurements lead to an expectation of ferromagnetism in JH178, but not JH177.

2.3.3 XRD analysis

Figure 2.6(a) shows experimental 004 $\omega/2\theta$ scans for the thick LT GaAs films grown by MBE and MEE. As expected from the RHEED pattern, the 120 °C MBE GaAs sample shows no distinct peak in addition to the substrate peak. The 115 °C MEE grown sample meanwhile, does show an additional peak, which is present on the LHS of the substrate peak. Clear interference fringes are also observed, indicating a sharp and smooth surface. These results confirm that GaAs grown at 120 °C by MBE is not deposited epitaxially and most likely has an amorphous structure. GaAs grown by MEE at 120 °C on the other hand, grows single crystalline and epitaxially on a GaAs substrate. Information provided by XRD regarding smoothness of the surfaces is corroborated by AFM measurements, which give RMS values of 3.9 nm and 0.7 nm for JH175 and JH176 respectively. Analysis of the thickness fringes present in JH176 yield a thickness of 190 ± 20

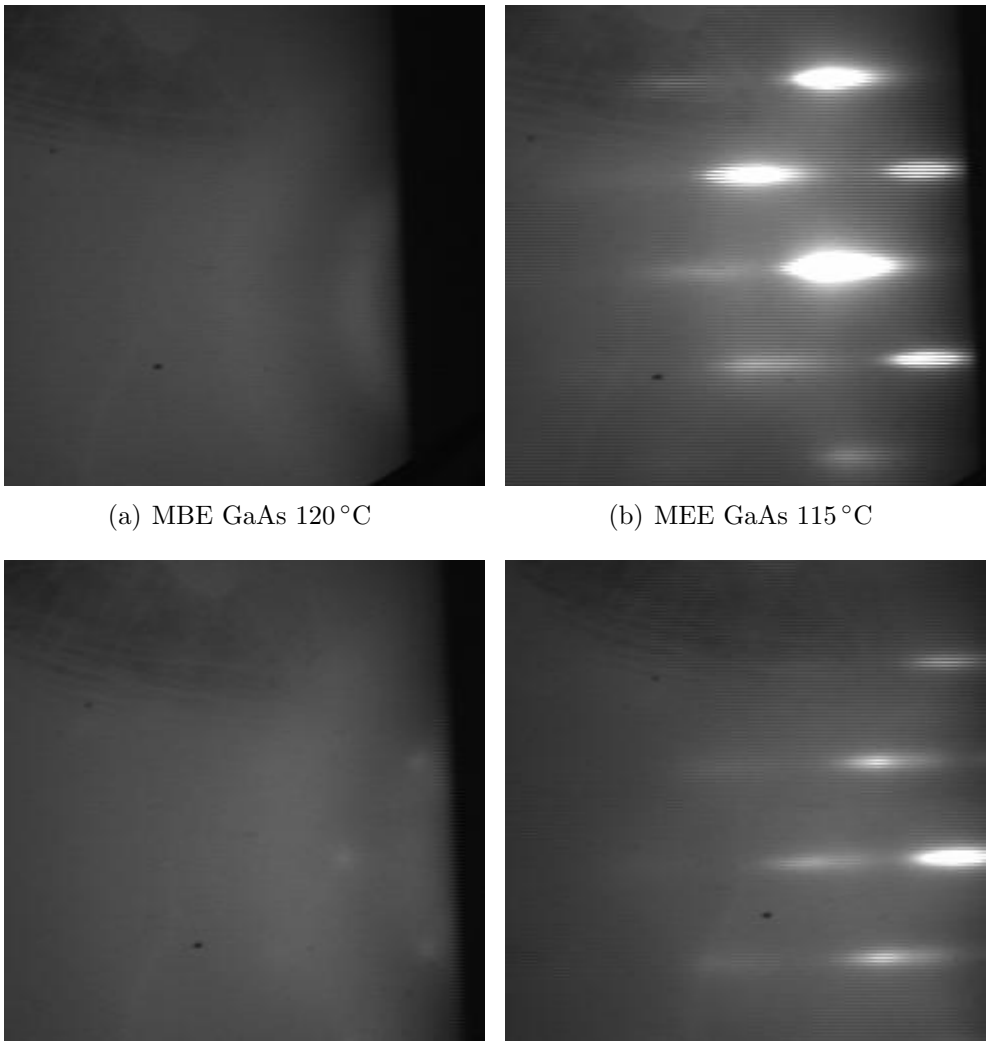

(a) MBE GaAs 120 °C

(b) MEE GaAs 115 °C

(c) MEE GaMnAs 115 °C

(d) MEE GaMnAs 150 °C

Figure 2.5 – Various RHEED patterns with 12 keV primary beam energy, observed at end of growth of low temperature Ga(Mn)As grown by either MBE or MEE.

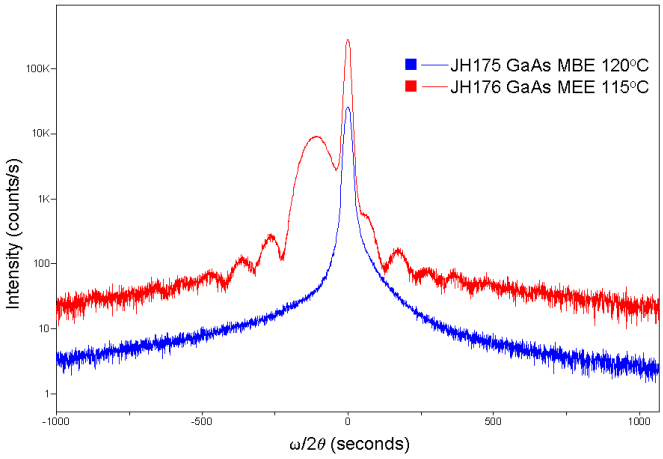

(a) GaAs grown at $\sim 120\,^{\circ}$C: MEE vs MBE

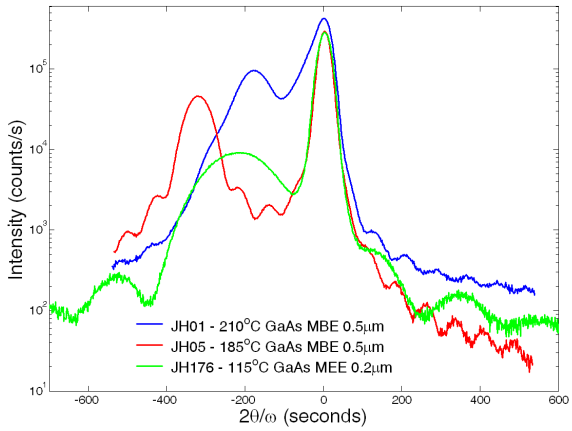

(b) Epitaxial LT GaAs: MEE vs MBE

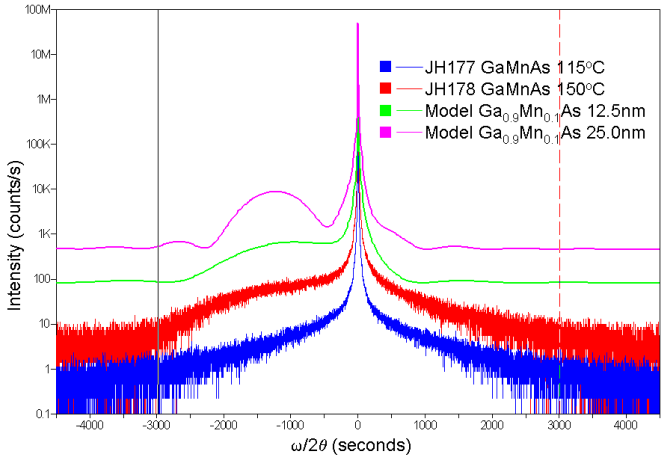

(c) GaMnAs MEE: 115 vs 150 °C

Figure 2.6 – Symmetric 004 reflection $\omega/2\theta$ linescans of low temperature Ga(Mn)As comparing the effects of growth temperature and growth methods (MEE and MBE).

nm, in agreement with the nominal value of 200 nm.

In figure 2.6(b), the MEE grown GaAs sample is compared with above transition MBE grown GaAs samples from section 2.2. The peak position from the LT GaAs in the MEE sample is seen to be close to the position expected from a 200 °C MBE grown sample. As the peak position is closer to the GaAs substrate than the 185 °C sample, this would suggest that JH176 has a lower number of As antisites than JH05. The FWHM of the MEE LT GaAs peak is considerably wider than the MBE samples, however since the sample has a much smaller thickness, this feature cannot be attributed to the lower growth temperature (or growth method). The integral time for each data point was also different between the MEE and MBE scans, which could account for the possible differing amounts of 'smoothness' between the data.

Simulated and experimental 004 $\omega/2\theta$ scans for the GaMnAs film are shown in figure 2.6(c). JH177 (GT 115 °C) shows no additional peaks to the one due to diffraction from the substrate, suggesting amorphous material. The data from JH178 (GT 150 °C) meanwhile does show additional information, the extra 'peak' though, is ill-defined and broad and appears as more of a low intensity shoulder to the GaAs substrate peak. Simulations however, show that this is due to the sample being very thin; an increase in thickness to 25 nm should be sufficient to see a distinct peak relating to the GaMnAs epilayer and to possibly witness interference fringes. Despite the GaMnAs peak being broad, the shape does match up well with the model. The position of the peak (which is hard to define) is determined by the Mn concentration, simulations suggest a [Mn] of $\sim 10\%$. This however, is a scan of an unannealed sample and will include contributions to the lattice dilation from both substitutional and interstitial Mn.

Further information can be obtained from a reciprocal space map of the asymmetric 444 reflection and results from all samples are shown in figure 2.7. The RSM of JH175 (figure 2.7(a)) shows a relatively extensive (compared with scans of other samples) low-intensity halo around the substrate peak, indicative of poor-quality GaAs material. The JH176 results on the other hand, displays an additional compact peak directly below the substrate peak. This demonstrates that the material quality of the LT GaAs film is good and that the epilayer is fully strained.

The RSMs from the GaMnAs samples (figures 2.7(c)and 2.7(d)) do not clearly show any additional peaks, most likely due to their thin nature. It is possible

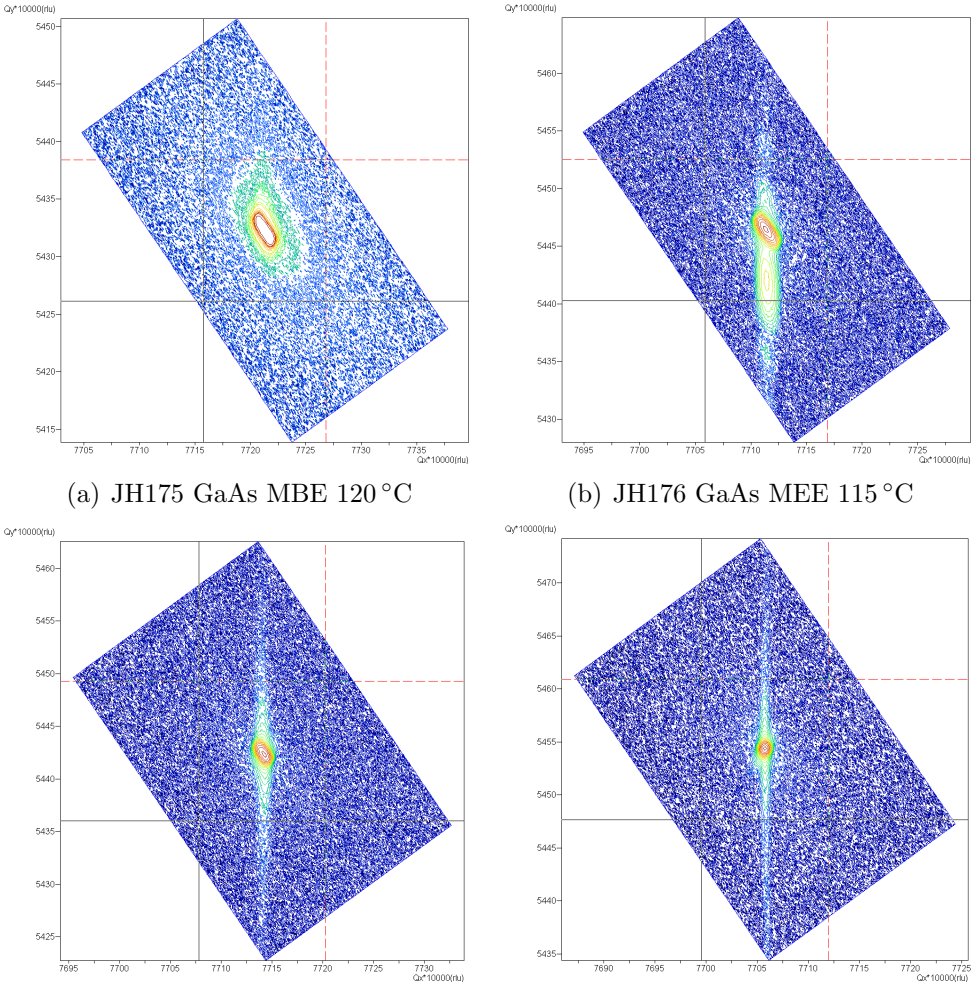

(a) JH175 GaAs MBE 120 °C

(b) JH176 GaAs MEE 115 °C

(c) JH177 GaMnAs MEE 150 °C

(d) JH178 GaMnAs MEE 115 °C

Figure 2.7 – Reciprocal space maps of the asymmetric 444 Bragg reflection of Ga(Mn)As samples. Scans were taken using the triple axis detector with the same scan range and time for each sample.

however, that the scan range was not sufficient to pick up diffraction originating from the GaMnAs layers. As the intensity from the GaMnAs layer is so small in the 004 scan of JH178, it is perhaps worthwhile waiting until a thicker GaMnAs sample has been grown, before carrying out a more in-depth XRD analysis. In both scans, an extension of the substrate peak running in the vertical direction is witnessed, evidence that the GaMnAs layers are fully strained.

2.3.4 SQUID results

The two GaMnAs thin films were submitted for SQUID analysis in order to determine their Curie temperature and degree of Mn incorporation. As expected, measurements of JH177 (GaMnAs, GT 115 °C) did not show any remnant moment, either before or after annealing. The measured temperature dependence of remnant magnetization along $[1\,\bar{1}\,0]$, $[1\,1\,0]$ and $[0\,0\,1]$ for JH178 (GaMnAs, GT 150 °C) is shown in figure 2.8. The sample was annealed to allow diffusion of Mn interstitials to the free surface. The graph is characteristic of a typical ferromagnetic GaMnAs sample, and shows that JH178 has in-plane magnetism. It can also be seen that the magnetic anisotropy is uniaxial along $[1\,1\,0]$ for temperatures above 30K, which in itself is unusual as GaMnAs is typically uniaxial along $[1\,\bar{1}\,0]$. Analysis of the data yields a respectable Tc value of 109K and a [Mn] of 6.7% (see appendix A.2). For a nominal flux of 12%, typically a [Mn] value close to 9% is expected. Considering however, this is a first attempt at growing GaMnAs by this method and that there is much room to optimise growth, through both stoichiometry and shutter sequence, these are arguably very promising results.

2.4 Conclusions and Future Work

Despite predictions that GaAs grown at low temperatures (below 180 °C) will possess a rock-salt structure, EXAFS measurements show that GaAs remains zinc blende when grown at temperatures down to 120 °C. For thickness up to 0.5 μm, it is found that when grown by MBE, GaAs is no longer deposited in a epitaxial single-crystalline manner at a growth temperature around 150 °C. Instead it is microcrystalline, with sufficient short-range order that EXAFS measures a disordered zinc blende structure, but no measurable long-range order as detected

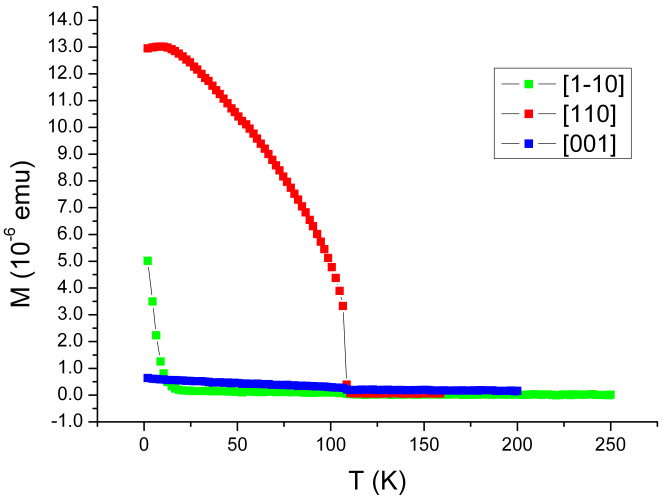

Figure 2.8 – Remanance data after field cool for annealed JH178: MEE GaMnAs 150 °C.

by XRD measurements. In line with other published material [37], single crystal LT GaAs has a larger lattice parameter than conventional GaAs, which has been shown to be due to As antisite defects, arising from a incorporation of As excess [44].

Growth of LT GaAs by MEE was undertaken to test the hypothesis that this growth method would lead to less incorporation of As antisites, as it would provide a mechanism for excess As to evaporate from the growing surface. Using MEE, GaAs was found to grow in a single-crystalline manner with smooth surfaces down to 115 °C. As this was an exploratory study, not many samples were grown. It would be interesting to see how low the growth temperature can be taken and still produce good quality GaAs. The measured out-of-plane lattice parameter for the 115 °C MEE grown sample was found to be comparable with that expected from a MBE grown sample at 200 °C, suggesting less incorporation of excess arsenic. More detailed work can also be carried out on the effects on material quality of Ga:As flux ratio and sequence shutter times e.g. longer pauses, longer/shorter Ga/As deposition times. It would be interesting to start with the growth of thicker MEE LT GaAs samples, with efforts made to perform X-ray scans using the same parameters as those used for the MBE grown samples. This would allow for a more comprehensive comparison between the effects of MBE and MEE on the growth of LT GaAs. Should I continue with this work, my first priority would be to more closely monitor the Ga:As, as I feel this important growth parameter would

benefit from experience. It may well be possibly that lower temperature growth of MBE GaAs can be achieved by this factor alone. A possible other avenue of investigation would be the use of in-situ Auger electron spectroscopy, or maybe SIMS, in order to assess Ga:As ratio of grown samples.

Single-crystal ferromagnetic GaMnAs has been grown at a substrate temperature of 150 °C using MEE. There is much scope to work on MEE growth of GaMnAs with the exploration of parameters such as: quantity of Ga material deposited in each sequence (by changing deposition time or growth rate), pause times, Mn shutter sequence (i.e. when in the sequence Mn is deposited) and III:V flux ratio. Goals would be to locate the lowest growth temperature that produces good quality GaMnAs and optimise growth conditions to yield higher Tc values than those reported here. Initial steps could include repeat growths using same conditions as those described in this chapter, but with double the thickness to help isolate the GaMnAs peak in X-ray studies. It would also be interesting to collect XRD information from both annealed and un-annealed GaMnAs material, allowing for a qualitative study on the number of Mn interstitial defects.

Chapter 3

GaAs Based Dilute Nitrides

3.1 Background

The use of the internet and technology applications involving data transmission has surged in recent years, leading to an increased demand for higher bandwidth networks. This can be achieved by bringing the optical part of the network as close as possible to the subscriber. A high-capacity optical fibre, directly connected to the location of the subscriber, would require low cost, high performance emitters and detectors that can be easily coupled to the fibres. For this, lasers are required to emit in the 1.3-1.55 μm range; the two end values of which, correspond to the optical absorption minima of silicon fibres.

Present day lasers operating in this long wavelength range are based on InP heterostructures. While GaInAsP/InP distributed feedback lasers are well established light sources for long haul fibre backbone networks [45], they are currently too expensive to meet the demand for hundreds of millions of lasers that would be required in local area networks. In addition to other problems, there exist inherent properties, such as low power output and low characteristic temperatures, which cannot be significantly improved by any bandgap engineering [46]. Low operating temperatures of ∼60K stem from poor electron confinement and mean that lasers require thermoelectric cooling in order to function. These limitations have lead to the consideration of alternative materials systems for semiconductor lasers which emit in the 1.3-1.55 μm range.

Materials are needed with bandgaps between 0.95 and 0.80 eV and a lattice parameter similar to readily available substrates, such as GaAs and InP. While InP based work continues, various GaAs based approaches have developed. These include InAs quantum dots [47], GaAsSb/InGaAs [48] and InGaAsN [49] strained quantum wells and even the quinary system GaInNAsSb [50].

The dilute nitride system has attracted considerable interest, not only as a proposed material for practical long-wavelength emitting lasers, but due to their unusual optoelectronic properties. In 1992, Weyers et al. [51] demonstrated that nitrogen incorporation in GaAs results in a narrowing of the bandgap, leading Kondow et al. [52] to propose the InGaAsN material system for long-wavelength emission.

In conventional alloys the bandgap changes almost linearly with composition, according to the virtual crystal approximation. In this model, a smaller lattice constant will lead to a increase in the bandgap. Nitrogen however, is an unusually light and very electronegative element. Despite GaN being a wider bandgap semiconductor than GaAs and possessing a smaller lattice parameter, the addition of small amounts of nitrogen to GaAs leads to a significant reduction in the bandgap energy; an effect known as giant bandgap bowing. Each one percent of N reduces the bandgap by about 150 meV, thus the addition of only a few percent should be sufficient to achieve 1.3 μm emission in GaAsN [53]; GaAs bandgap of ∼872 nm/1.43 eV.

The origin of the bandgap lowering is explained by the band anti-crossing model [54], see figure 3.1. This describes the repulsion of the GaAs conduction band (parabolic dotted line, E_Γ) with the resonant lone nitrogen localised state (horizontal dashed line). The interaction results in the lower E_- and upper E_+ bands, leading to a lowering of the conduction band in the alloy.

Since the lattice parameter of GaN is smaller than that of GaAs, GaAsN alloys grown on GaAs are under tensile strain. This limits the thickness with which epilayers of this material can be grown without dislocations or cracks. The addition of In can not only compensate the nitrogen induced strain, due to its large size, but also further lower the bandgap. In this way, it should be possible to grow $Ga_{1-x}In_xAs_{1-y}N_y$ quaternies that are lattice matched to GaAs and have bandgaps in the desired 1.3-1.55 μm spectral range. This system should be lattice matched to GaAs for x $\sim$ 3y [2].

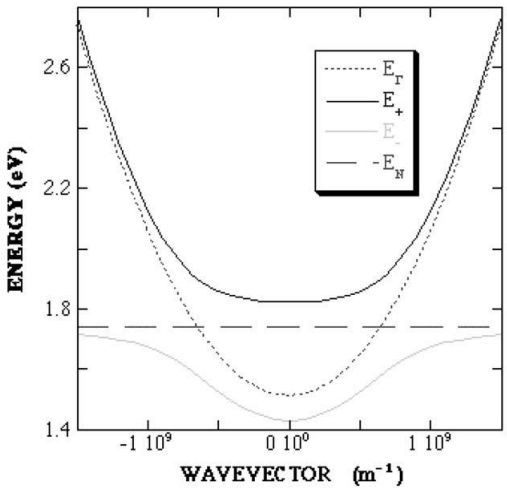

Figure 3.1 – Restructuring of the conduction band in GaAsN alloys. Figure taken from Tu et at (2006) [3].

The large local strain when N is in an As sublattice site, results in a very low solubility limit of N. As a result, phase separation into microscopic regions composed of hexagonal GaInN and cubic GaInAs can occur. To incorporate N into the zinc blende GaAs lattice, the growth temperature needs to be lowered from that typically used for GaAs. For MBE, a growth temperature of 420-480 °C for GaInAsN and GaAs capping layers is required versus ∼600 °C for conventional GaAs growth.

MBE permits accurate low-temperature growth of GaInAsN layers which are free of structural defects. Grown-in point defects however, such as interstitial nitrogen, gallium vacancies, As_{Ga} antisites and N-N complexes, mean that the optical quality of dilute nitrides deteriorates with increasing nitrogen concentration. GaInAsN samples grown by MBE commonly use a radio frequency (RF) plasma source to generate active nitrogen. The various ions produced in the plasma however, can damage the growing surface and lead to poor sample quality. Additionally, active nitrogen itself is a radical. As a result, the energy released on reaction with the surface can also be sufficient to cause damage [4].

These factors mean that epitaxial growth of good optical quality dilute nitrides remains a great challenge. The following work investigates the incorporation of nitrogen from a novel AlN powder source. Previous studies have suggested that the sublimation of AlN provides a pure flux of AlN dimers [55] and not Al and N_2, as one would generally expect from a III-V compound. This neutral source

of nitrogen could potentially provide a way to eliminate the problems associated with the use of active nitrogen, as provided by a RF plasma source.

Sublimation of AlN powder is a common method for producing bulk AlN crystals [56]. The theory concerning the species present during AlN powder sublimation however, remains unclear. In most instances, the sublimation is performed under a nitrogen overpressure. The one paper found that shows AlN sublimation fluxes under vacuum, loosely suggests that the AlN powder will require a cell temperature of ∼1400 °C [57].

3.2 Experimental Details

To investigate AlN as a source of nitrogen in dilute nitrides, the purpose built 'mini-MBE' system was used. Flux values for As and Ga were chosen to give growth rates of ∼0.3 μm however, growth-rate measurements on a separate piece of wafer cannot be performed in this system. The fluxes were checked prior to each growth and were found to be stable throughout the entire growth run. A kSA BandiT was not yet fitted to this machine, so pyrometry was used to measure substrate temperature, which works, at best, down to 550 °C. The thermocouple value for a growth temperature of 600 °C was found using a pyrometer, for all other growth temperature values described in this section, thermocouple values were calculated by extrapolation.

Samples were grown on GaAs(001) substrates which were thermally deoxidised prior to growth. Samples cannot be grown under rotation in this chamber, though manual rotation can be performed. Each wafer was orientated such that the RHEED electron gun runs parallel to the [110] direction, meaning that on conventional GaAs, the RHEED sees a 2x reconstruction pattern under normal As-rich growth conditions. The RHEED screen in the mini-MBE system has line of sight with the sample holder. Due to the high temperature of the AlN cell, the RHEED screen was exposed to considerable light flux during samples grown with AlN. As a result the ability to see the RHEED patterns was hindered.

Sets of samples were grown at a range of temperatures between 400 °C and 600 °C for 2 hrs each. Each set consisted of at least one control sample (GaAs) and at least one AlN sample (GaAs grown while exposed to a sublimed AlN flux).

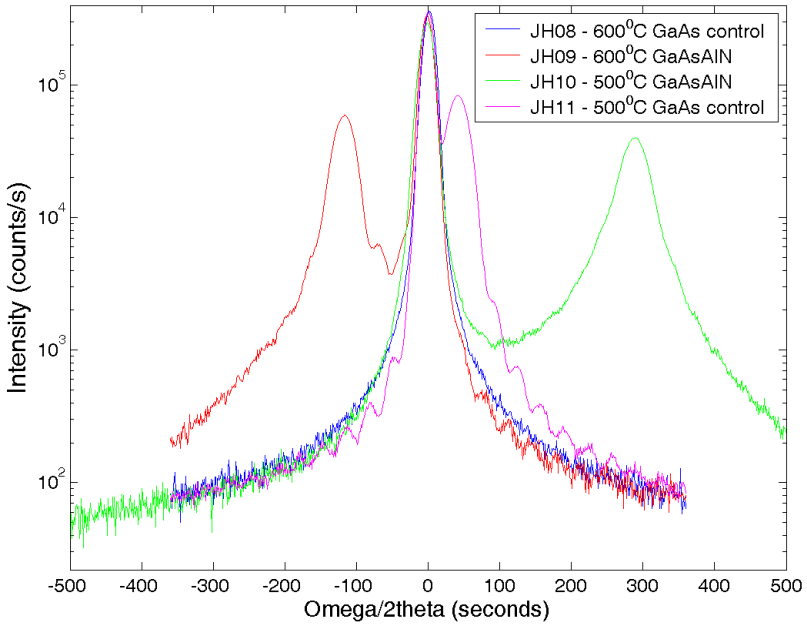

Figure 3.2 – $\omega/2\theta$ scans of the symmetric 004 Bragg reflection of samples JH08-JH11. The simulations place the thicknesses at about 0.6 µm.

Structural analysis using HR-XRD was performed on the samples. Symmetric 004 reflection $\omega/2\theta$ linescans and asymmetric 444 reflection $\omega/2\theta$:ω reciprocal space maps have been studied. To investigate any bandgap differences, absorption measurements were carried out using the kSA BandiT set-up on the Varian mod Gen II. Preliminary SIMS and EDX measurements have also been performed.

3.3 Results and Discussion

3.3.1 X-ray analysis

To start, two pairs of samples were grown at 500 °C and 600 °C, each with a control and an AlN sample. $\omega/2\theta$ linescans were performed on the 004 Bragg reflection with the open detector, results are presented in figure 3.2. The highest intensity peak corresponds to the GaAs substrate and, where relevant, includes contributions from the GaAs layer. The second, lower intensity peak (where present) corresponds to the layer grown on the substrate.

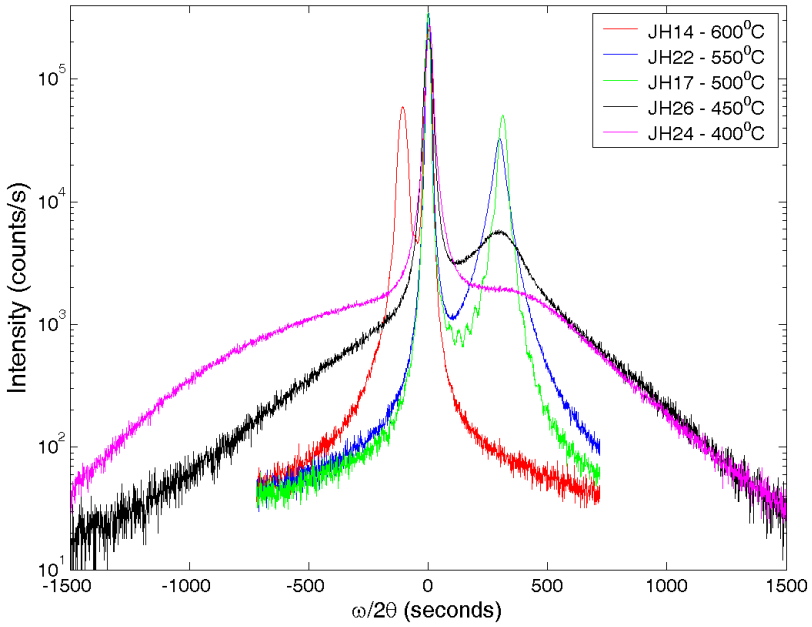

Figure 3.3 – $\omega/2\theta$ scans of the symmetric 004 Bragg reflection of GaAsAlN grown at different temperatures in the range 400-600 °C.

Regarding the 600 °C pair (JH08 and JH09), the control sample shows just one peak, as expected, due to GaAs. The AlN sample shows an additional peak on the left hand side of the substrate peak. This result however, is not what was hoped; a peak at a smaller angle corresponds to a larger lattice parameter, not smaller.

The 500 °C AlN sample (JH10) looks promising, as it shows a peak on the right hand side. This indicates a smaller lattice parameter and therefore, possible incorporation of nitrogen. The control (JH11) however, also shows a peak on the right hand side of the substrate peak, meaning the previous result should be viewed with caution. Two possible explanations for this extra peak in the control sample present themselves: (i) there is a memory effect associated with the use of the AlN cell or (ii) it is an isolated incident due to the significant outgassing the AlN cell experienced two days prior to the growth of this sample; this was the first time that the cell had been taken up to 1400 °C.

Samples JH09-11 all show clear thickness interference fringes, indicating that the interfaces are smooth and well defined and epitaxial growth of the layer occurred. Analysis of the fringe period, using the fitting software, gave thicknesses of 0.58 ± 0.03 µm, 0.60 ± 0.05 µm and 0.59 ± 0.03 µm for JH09, 10 and 11 respectively,

giving an average thickness of 0.59 ± 0.02 μm. These results confirm that we have achieved a growth rate of 0.3 μm/hr. As the GaAs layer in JH08 is structurally the same as the substrate no fringes are observed.

In order to see if these results are reproducible and investigate if there are any memory effects associated with the AlN cell, the samples were regrown with controls grown before and after every AlN sample. $\omega/2\theta$ 004 linescans were performed, as before, on the new samples. All four control samples appeared as they should, i.e. just one peak. This would appear to confirm that the extra peak observed in JH11 was a spurious result and has been attributed to the outgassing of the AlN cell. Comparison between the two AlN samples grown at 600 °C and the two at 500 °C, show that the results are reproducible, both peak position and FWHM values were found to compare well. Thickness analysis of the repeat samples gave an average thickness of 0.58 ± 0.02 μm, also in agreement with the previous results.

Compositional analysis was performed for the AlN samples. For AlN samples grown at 600 °C it was assumed that the N had evaporated from the surface, leaving behind only Al. Since Al acts to slightly increase the lattice parameter this could explain the peak being at a lower angle than the GaAs substrate. Since the inclusion of small amounts of nitrogen would act to decrease the lattice constant, this analysis represents a minimum aluminium content. In order for the lattice parameter to have increased to the value presented in the results, an Al content of ∼30% would be required. Considering the fluxes involved this value does not make physical sense (AlN flux was approximately an order of magnitude smaller than the Ga flux), suggesting other chemical processes are involved in the change of lattice parameter.

To model the AlN samples grown at 500 °C, a similar but opposite assumption was made; no aluminium present, only nitrogen. This gave a value for the nitrogen content of 0.06%. Again, the model represents a minimum composition value, for every 1% of Al present in the sample, an additional 0.01% needs to be added to the N content to retain the measured lattice parameter. In order to get absolute compositional values, calibration via another technique needs to be carried out to fix either the Al or the N value. This, of course, assumes that no additional elements are present in the films.

The effect of growth temperature on the structure of GaAsAlN was subsequently investigated. Three more pairs of samples were grown at 550 °C, 450 °C and 400 °C.

Sample	Temperature	Peak	FWHM(arc min)	FWHM ratio layer/substrate
JH14	600 °C	Substrate Layer	0.41 0.63	1.54
JH22	550 °C	Substrate Layer	0.29 0.88	3.03
JH17	500 °C	Substrate Layer	0.29 0.62	2.14
JH26	450 °C	Substrate Layer	0.42 8.02	19.1
JH24	400 °C	Substrate Layer	0.57 ∼18.5	32.5

Table 3.1 – FWHM values obtained from peaks observed in 004 symmetric Bragg reflection linescans of GaAsAlN grown at a variety of temperatures.

004 $\omega/2\theta$ linescans were performed, with results of the AlN samples presented in figure 3.3, along with the repeated 600 °C and 500 °C AlN results. XRD analysis of the control samples (not shown) all show just one peak, attributed to GaAs. The FWHM values of the GaAs peak in all the control samples were comparable, i.e. no apparent difference in crystal quality was observed.

The 004 $\omega/2\theta$ linescan of the AlN sample grown at 550 °C shows an additional peak, on the right hand side of the GaAs substrate peak, at approximately the same position as that grown at 500 °C. The AlN sample grown at 450 °C again shows a second peak on the right hand side of the substrate peak, also at a similar position, but it is not as distinct and is significantly broader than that seen in previous results. The intensity of this second peak is two orders of magnitude lower than the substrate peak, cf. an order of magnitude lower than equivalent samples grown at 500 and 550 °C. A much higher background is also observed, showing that the material has a higher level of defects than previously discussed AlN samples. Finally, the sample grown at 400 °C shows no clear additional peaks, but does show extreme broadening of the GaAs peak. This indicates that the film is almost amorphous and material grown at this temperature is no longer being deposited in an epitaxial manner. Since the control samples grown at 400 °C and 450 °C do not show a broadening of the GaAs peak, the decrease in material quality of the respective AlN samples can be attributed to the presence of the AlN flux. Thickness interference fringes are also not observed in these two AlN samples.

The relative values of the FWHM from the substrate and layer peaks can be used

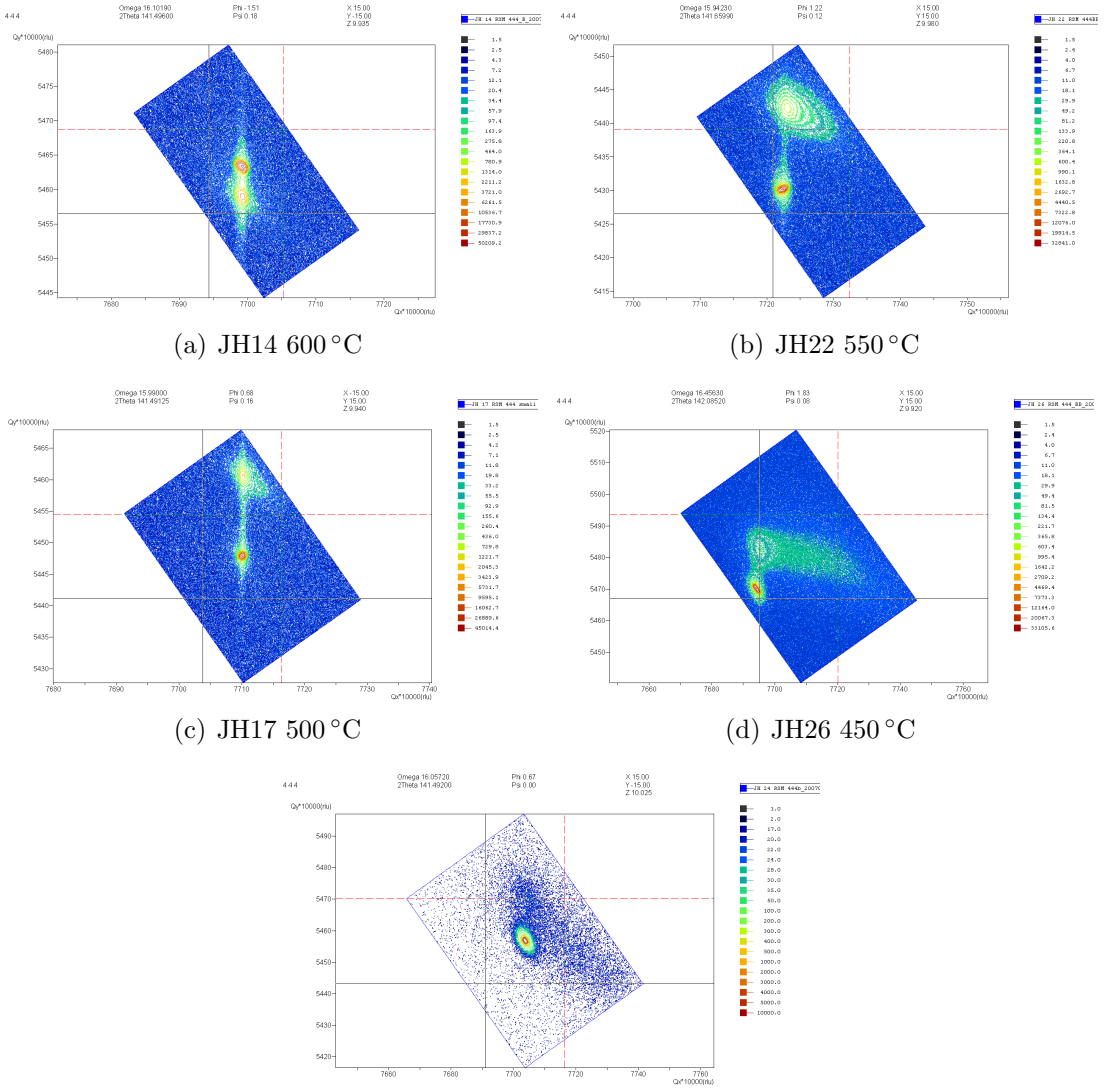

(a) JH14 600 °C

(b) JH22 550 °C

(c) JH17 500 °C

(d) JH26 450 °C

(e) JH24 400 °C

Figure 3.4 – Reciprocal space maps of the asymmetric 444 Bragg reflection of GaAsAlN grown at a variety of temperatures. Scans were taken using the triple axis detector.

to assess the quality of the layer with respect to the substrate, see table 3.1. Comparison with the substrate is undertaken, as the layer can never be of better quality than the substrate. The data shows the substrate peaks in the AlN samples all have similar FWHM values. AlN samples grown at 600 °C, 550 °C and 500 °C have epilayer FWHM values that are only slightly larger than their respective substrates, indicating that the GaAsAlN epitaxial films are of high quality. The samples grown at 450 °C and 400 °C show progressively larger FWHM values; ∼16 and ∼32 times higher than their respective substrates. Factors which increase the FWHM are the presence of mosaic blocks and strain (which broaden the peak) and defects (which introduce a extension of the peak in both $2\theta/\omega$ and ω at low intensities).

Further information can be obtained from reciprocal space maps (RSMs) of the asymmetric 444 reflection, results for the AlN samples are shown in figure 3.4. The peak widths in the Qx direction (x axis) also give an indication of crystal quality. RSMs of 600 °C and 500 °C AlN samples, figures 3.4(a) and 3.4(c), indicate that the crystal quality of the GaAsAlN layer is almost comparable to the underlying substrate. In both cases, the peak position of the layer has the same Qx value as the substrate peak, meaning that the GaAsAlN film is fully strained with respect to the substrate.

Samples grown at 550 °C and 450 °C have layer peaks which exhibit much worse mosaicity than the reference substrate peaks. The extensions in the Qx direction are much larger than the 600 °C and 500 °C AlN samples, indicating poorer crystal quality. The extensions of the layer peak in the Qx direction are clearly asymmetric, not symmetric as we normally witness. This would suggest a tilt in the phi direction i.e. the GaAsAlN planes are not parallel to the substrate planes. The layer and substrate peaks are not aligned in Qy and hence, show a small amount of relaxation. This suggests the presence of dislocations which could partly explain the poorer material quality. Estimates for the relaxation can be obtained by inputting the same model sample into the X'Pert Epitaxy software for each result. A model sample of $GaAs_{.994}N_{.006}$, thickness 0.6 μm was used, giving relaxation values of: 6% for the AlN layer grown at 550 °C and 16% for the film grown at 450 °C.

Both tilted mosaic blocks and finite size regions lead to a broadening of diffracted peaks. In reciprocal space this leads to a characteristic broad elliptical scatter-

ing shape; whereby the contribution from lateral correlation length is parallel to the surface plane, while the microscopic tilt contribution is normal to the radial direction (along an $\omega/2\theta$ scan direction). Separation of these contributions can therefore be achieved by inspection of asymmetric reflection RSMs. From visual inspection of the 444 RSM from the AlN sample grown at 450 °C, it can be seen that the extension runs mainly along Qx. This indicates that there is little contribution to the scattering from a distribution of tilts, but there is a significant contribution due to a short correlation length, i.e. the material has more amorphous content than previous results. The diffraction in the RSM of the AlN grown at 550 °C shows a greater contribution from tilted mosaic blocks with the extension spread over a smaller Qx range.

As expected from the 004 linescan, the sample grown at 400 °C shows no additional peak in the RSM, but does show a low intensity scattering background. This diffuse scattering extends over a significant area and is attributed to the presence of defects. The lack of a distinct separate peak reaffirms that this material is highly amorphous. The AlN sample grown at 450 °C also shows significant diffuse scattering, but to a lesser degree, again suggesting the presence of defects.

3.3.2 Absorption measurements

Absorption spectra were taken of all samples using the kSA BandiT setup in the Gen II. An absorption spectrum was taken twice for each sample, one whilst the sample was held at 70 °C and the other at 200 °C. This was done to differentiate between general features in the spectrum and those related to the bandgap of the material. Raw data were divided by a GaAs reference spectrum and scaled such that values ranged from $0 - 1$. Measurements were taken under a constant illumination of lamp power 25.8%.

Control structures grown above 400 °C show a typical GaAs absorption edge i.e. a distinct step. The control sample grown at 400 °C meanwhile, exhibits much broader absorption with a less defined step. This can be explained by the fact that its material quality is expected to be poorer than the other control samples, due to the increased presence of As antisites.

If there were nitrogen incorporation, we would expect a material with a smaller bandgap than GaAs. Consequently, we should see a step in the absorption edge,

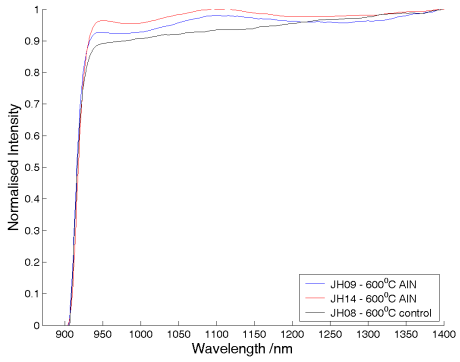

(a) Samples grown at 600 °C

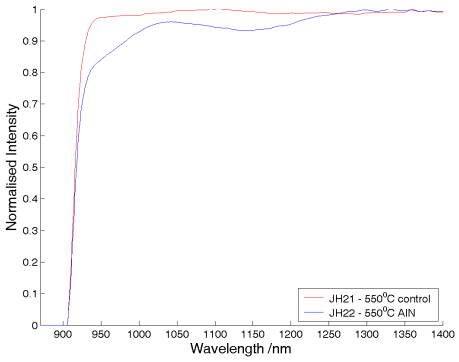

(b) Samples grown at 550 °C

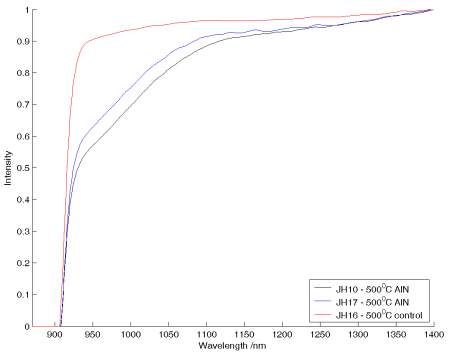

(c) Samples grown at 500 °C

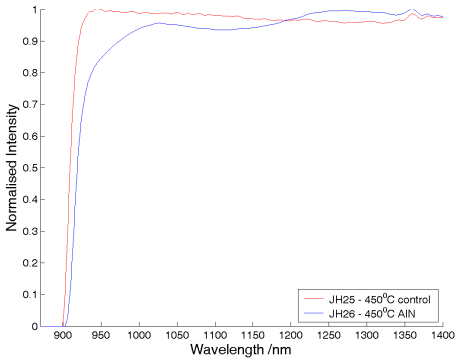

(d) Samples grown at 450 °C

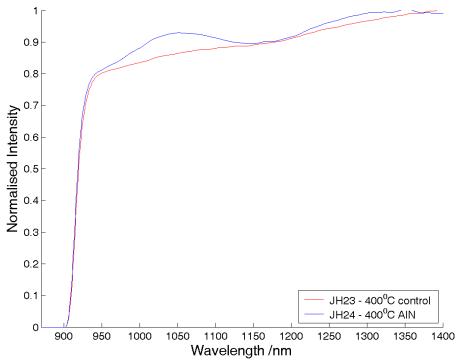

(e) Samples grown at 400 °C

Figure 3.5 – Absorption measurements of samples JH08-JH26 taken using the BandiT system in the mod Gen II system. All samples were held at ∼70 °C. Data was divided by a reference GaAs spectrum and normalised to unity.

however no clear steps were seen in any of the spectra. With the exception of the 500 °C structure, the absorption spectra of samples grown exposed to an AlN flux do show oscillations above the absorption edge. These are attributed to interference fringes, originating from light reflecting from layers of differing refractive indices. AlN exposed samples grown at 500 °C, though not showing a distinct step, appear to show the top of the absorption edge having been attenuated. The spectrum also shows absorption over a wider range (up to 1100 nm cf. 1025 nm) than other AlN exposed samples.

While the results do not provide clear information, it is evident that the samples grown exposed to a sublimed AlN flux differ from GaAs, most likely due to the presence of defects.

3.3.3 RHEED observations and EDX

RHEED monitoring of the AlN samples during growth showed the following:

Samples grown at 600 °C show a 2x4 reconstruction. For samples grown at 550 °C, 500 °C and 450 °C a 2x reconstruction could be observed, but became progressively harder to distinguish with decreasing temperature. A 4x reconstruction could not be seen. The 400 °C control and AlN exposed samples displayed diffuse streaks, with no evidence for the 2x or 4x reconstructions.

Preliminary energy dispersive X-Ray (EDX) analysis has been performed on samples JH08, 09 and 10 by the Nottingham Nanoscience and Nanotechnology Centre, in order to measure the Al content. JH08 (600 °C control sample) returned a value of 0.04%. The AlN samples grown at 600 °C and 500 °C both returned a baseline value of ∼2%, in stark contrast to the X-ray result. This again implies that other mechanisms (in addition to growth temperature and presence of AlN) are also responsible for the structural changes witnessed in GaAsAlN grown at 600 °C.

3.3.4 SIMS

SIMS measurements were performed on the AlN exposed samples by the Fraunhofer Institute for Applied Solid State Physics (Freiburg, Germany), using Cs

sputtering to obtain compositional and impurity profiles. Results confirm the presence of Al and high O contamination levels, but fail to detect N.

The returned [Al] is 6.5% for JH9 and JH17 (600 °C and 500 °C) and 15% for JH22 and JH26 (550 °C and 450 °C). This suggests that the AlN flux from the source was possibly much smaller than the corresponding Al flux. Another possibility is that the N was sputtered off during the SIMS process as another molecular species (e.g. AlN dimers), which was not measured.

While a smaller lattice constant initially suggested the incorporation of nitrogen, taking into the account the SIMS data, this may be caused by the O content (O has the same covalent radius as N, 0.074 nm). None of the control samples were measured. If the oxygen impurities are responsible for the decreased lattice parameter observed in the AlN samples, then it would be useful to compare the [O] levels in the control and the AlN samples.

3.4 Conclusions and Further Work

XRD and absorption measurements show that GaAs grown in the presence of a sublimed AlN flux are structurally and optically different to GaAs. Whether this is due to the presence of defects or the incorporation of Al and/or N is unclear.

Material grown with AlN exposure at 600 °C looks to be of good quality, but appears to contain very little, if any, nitrogen. AlN exposed samples grown at 500 °C appear to be the highest quality material and potentially have the desired composition. As the growth temperature is decreased from 500 °C material quality progressively worsens, despite equivalent GaAs samples not exhibiting material quality that deteriorates with decreasing growth temperature. The AlN exposed sample grown at 550 °C seems to have a similar lattice constant to the 500 °C grown sample, but has significantly poorer crystal quality than both the 500 °C and 600 °C AlN samples.

An explanation for the peak at a lower angle than the GaAs substrate peak has been proposed for samples grown with AlN at 600 °C. If nitrogen is evaporating from the surface at 600 °C, it leaves behind Al in a reactive state. It is conceivable that this reacts with background gas molecules containing oxygen, to form aluminium oxides. This is supported by SIMS measurements, which show that

the 600 °C sample has a [O] that is 133% higher than the value measured in other samples. The X-ray fitting software does not currently allow the modelling of layers containing oxygen.

One of the most pressing requirements is to establish what exactly is evaporating from the AlN cell. To this end, it would be useful to use a mass spectrometer which has line of sight with a AlN source. This will identify the species present in the flux produced by the sublimation of AlN. There is more scope with work involving SIMS analysis. Although a nitrogen signal was not observed in any of the sample, it is possible that the N was sputtered off as another molecular species (e.g. AlN dimers), which was not measured. There were also anomalies in the quantities of carbon and oxygen measured using different molecular species (e.g. 12C vs. 87CAs and 16O vs. 85GaO), which suggest that the GaAs SIMS calibrations used may not be correct for these samples.

Chapter 4

ScN and Related Alloys

4.1 Motivation

GaN is a well known, wide-bandgap semiconductor with many well estabilshed used and several further expected applications in areas such as high-temperature, high-power-high-frequency, high-power-high-voltage electronics and most notably, optoelectronics [7]. Despite being commercially available from the early 90's, its potential to revolutionise solid-state lighting has not yet been realised [6]. The barrier to achieving required efficiencies lies in achieving lower defect densities, which arise mainly due the unavailability of suitable low-defect density substrates.

Most research on this material has been carried out on the thermodynamically stable wurtzite phase. GaN, however, can also crystallise in the metastable zinc blende (cubic) polytype. This cubic form, c-GaN, in particular (0 0 1) oriented films, offers the prospect of increased optical efficiency over conventional wurtzite GaN (h-GaN) for some applications, due to the absence of polarization fields. Other advantages include expected higher electron and hole mobilities, excellent cleavage planes; important for laser fabrication, easier doping and contacting, and easier integration into other III-V heterostructures [7].

In the cubic form, strain relief leads to the formation of a high number of stacking faults (typically $5\text{x}10^{-9}\text{cm}^{-2}$ [58]) along {1 1 1} planes [7]. Before devices based on c-GaN can be realised, the high characteristic stacking fault density needs to be reduced to an appropriate level.

While little work has focused on reducing the defect density in c-GaN, there has been much reported on efforts to reduce the dislocation density in h-GaN. One approach involves ex-situ processing, such as the use of lithographic techniques for subsequent selected area overgrowth [59]. Another common approach is the use of interlayers and buffer layers. AlN has been employed to act as a buffer layer [60], while interlayer materials which have proven successful in blocking the propagation of dislocations include SiN_x [61] and ScN [8]. It will therefore be interesting to investigate whether of use of ScN interlayers has an effect of the number of defects in c-GaN(0 0 1).

4.2 Literature Review

Sc is the first transition element. As such, it has the same number of Valance electrons as gallium, making ScN a group III-B transition metal nitride semiconductor. It has been reported to possess a direct bandgap in the region of 2.1-2.4 eV [62] and a smaller indirect bandgap of ∼0.9 eV [63]. It has the characteristic excellent physical properties of transition metal nitrides [62], such as high hardness, mechanical strength and high temperature stability (melting temperature $> 2600\,^{\circ}C$ [64]). Partial ionic bonding leads to a rock-salt structure, with a lattice constant of 4.5 Å [65] making it lattice matched to both polytypes of GaN; ScN(111) is latticed matched to c-GaN(111) and h-GaN(0002). It is thus a potential candidate for alloying in either system. .

Compared to conventional group III-nitrides, ScN has not been well studied. Bulk growth has been achieved using a sublimination-recondensation technique under a nitrogen atmosphere by Gu et al. [66]. The resulting ScN crystals were polycrystalline, with the predominant texture dependent on the growth conditions. SEM, XRD and Raman spectroscopy were performed on the samples. Niewa et al. [67] have prepared bulk ScN single crystals and powders using three different techniques: (1) synthesis from the elements, (2) decomposition reaction from $Li_3[ScN_2]$ and (3) reaction of binary intermetallic compounds from the Sc-In system with nitrogen. They measured a bandgap of 2.1 eV, in agreement with its red/brown colour. They also showed metal-like behaviour as measured by the resistivity. This was attributed to defects (arising from a 1% nitrogen vacancy), converting the 2 eV insulator into a heavily doped semiconductor.

Epitaxial ScN films have been grown using a variety of methods on a variety of substrates. Results indicate that the best material is acquired when grown by MBE, which is also the method of choice for growth of c-GaN. Furthermore, single crystalline ScN has the same crystallographic orientation as its substrate. The smoothest growth has been obtained for the (0 0 1) orientation, which has been attributed to a decreased barrier for surface diffusion [62]. All other orientations have been reported to grow in a 3D growth mode, as determined by RHEED studies.

Dismukes et al. [68] and Moustakas et al. [69] grew ScN on sapphire(0 0 0 1) using chemical vapour deposition and electron cyclotron resonance-MBE respectively. Both methods resulted in (1 1 1) oriented rough films. Gall et al. [70] grew ScN on MgO(0 0 1) using reactive magnetron sputtering, which initially resulted in films having mixed (0 0 1) and (1 1 1) orientations. The (1 1 1) orientation was found to be increasingly dominant with increasing thickness. Increasing the substrate bias resulted in a single (0 0 1) orientation, but these films were also rough. Further increases of sample bias led to the incorporation of N_2 gas bubbles and highly compressed layers. Over 100 ScN films were synthesized by plasma-assisted physical vapor deposition and RF-sputtering by Bai et al. [64] on quartz, sapphire and Si substrates. XRD showed that polycrystalline films could be obtained for both methods, but that amorphous films were produced when reactive sputtering was performed below 300 °C. The optical absorption coefficient and IR refractive index of the samples were measured; the IR refractive index was found to be 2.46. metal-organic vapour chemical deposition (MOVCD) growth has proven to be difficult due to the low vapour pressure of available Sc metalorganic precursors.

Al-Brithen et al. [71] reported the growth of smooth ScN films using RF-MBE at substrate temperatures of 800 °C. Films were all single-crystalline with either (0 0 1), (1 1 1) or (1 1 0) orientation depending on the starting substrate and its own orientation. They grew on sapphire(0 0 0 1) to achieve (1 1 1) oriented ScN, while for ScN(1 1 0) and ScN(0 0 1) they used MgO(1 1 0) and MgO(0 0 1) respectively. It was found that (1 1 1) and (1 1 0) oriented films grew in a 3D growth mode, while (0 0 1) can be grown in a 2D growth mode, resulting in atomically smooth surfaces (as measured by AFM and STM). The same group later reported a more detailed growth study of ScN(0 0 1) [62] investigating the effects of changing Sc:N flux ratio. For nominal N-rich conditions epitaxial films were found to grow with a surface morphology consisting of densely packed arrays of square shaped plateaus

and four faced pyramids, with atomically smooth terrace steps. Films were stoichiometric and transparent with a direct optical transition observed at 2.15 eV. Sc-rich conditions however, led to a surface morphology characterised by spiral growth mounds, attributed to increased Sc diffusion. These films were found to be non-stoichiometric, with N vacancies acting as donors. The increased carrier density led to a reduction in the optical reflection edge to 1 eV with absorption below the bandgap and a drop in resistivity.

Moram et al. [72] have investigated the growth of ScN on Si substrates using NH_3-MBE. If growth was initiated on Si(1 1 1) using a deliberate pre-nitridation of the surfaces, films were produced with a poorly defined orientation. Films having a mixed (111) and (100) orientation were produced if growth was initiated using significantly more, or less, than 1-2 ML Sc. For optimum growth conditions, single crystalline ScN(111) grew on Si(111). In a separate paper [73], RF-MBE growth of ScN(001)//Si(001) carried out at a growth temperature of 800 °C, for a range of Sc flux values, was reported. Though the RHEED pattern was initially streaky, all films showed polycrystalline rings and evidence of a 3D growth mode after $\sim$ 30 mins. A set of RF-MBE grown ScN(111)//Si(111) samples were also grown for comparison. The growth rate and FWHM of ω rocking curves were found to steadily increase and decrease respectively, with increasing Sc flux. The roughness of the surfaces, as measured by AFM, was found to remain fairly constant at $\sim$ 4 nm until high Sc flux values, where a rapid rise to $\sim$ 45 nm was observed.

4.3 Experimental Procedure

Samples were grown in a custom built MBE machine with an ultimate base pressure of $\sim$ 1x10^{-9} mbar. Activated nitrogen was supplied using an Oxford Applied Research CARS25 RF source, while conventional elemental sources were used for Ga, Sc, Mn and As. 99.995% Sc (HEFA Rare Earth Ltd.) was placed in a refractory tungsten crucible and heated in a standard high temperature cell. The Sc flux was calibrated for effusion cell temperatures from 1270-1390 °C using the in-situ beam monitoring ion gauge to measure the beam equivalent pressure. The relative sensitivity for the Sc flux relative to Ga was calculated to be 0.5 (see appendix A.1). The arsenic flux, if used, was kept constant to give a beam equivalent pressure (BEP) of 4x10^{-6} mbar. The nitrogen flux for all N containing samples

was also kept constant, providing a pressure in the growth chamber of $\sim$3.5x10^{-5} mbar with an applied RF power of 450W. The growing surface was monitored in-situ by RHEED, samples were not grown under rotation.

Films were grown on semi-insulating GaAs(100) substrates, which were thermally deoxidised prior to growth at a temperature of 650 °C. If a GaAs buffer layer was grown, then the substrate was deoxidised in the presence of an excess flux of arsenic. GaAs buffer layers were deposited at 600 °C with thicknesses $\geq$ 225 nm, this ensures subsequent growth was undertaken on a high-quality crystalline surface. RHEED studies on the buffer layer showed the conventional (2x4) arsenic stabilised reconstruction.

XRD analysis can be complicated by the fact that there is a relationship between the cubic and wurtzite GaN lattice constants, resulting in many peaks from both materials occurring at the same 2θ positions. Unique 2θ angles for each phase do exist; e.g. the 002 reflection from c-GaN ($2\theta \sim 40°$) and the 105 reflection from h-GaN ($2\theta \sim 105°$). These can therefore be used to identify the phase of GaN present. Analysis is further complicated by the fact that ScN and c-GaN are both cubic structures with near identical lattice parameters. This means that they both have the same allowed reflections and that diffraction peaks occur at the same 2θ values, i.e. XRD cannot distinguish between ScN and c-GaN.

The crystallographic orientation of the films was determined using $2\theta/\omega$ linescans. Partial pole plots (ϕ-ψ maps) have been obtained where required, around (i) 105 h-GaN Bragg reflection to determine whether wurtzite GaN was present and (ii) 111 c-GaN Bragg reflection to investigate the symmetry of the sample. In some cases RSMs have also been obtained in order to assess crystal quality.

The films were subjected to further characterisation by AFM, ORS, TEM (performed by University of Cambridge) and transport measurements (performed by University of Warwick).

4.4 ScN/c-GaN

Bonds in a rock-salt structure run along $\langle 1\,0\,0 \rangle$, compared to $\langle 1\,1\,1 \rangle$ in zinc blende materials. If ScN(1 0 0) can be grown on c-GaN(1 0 0), potentially no bonds would cross the interface, providing a mechanism to prevent stacking faults formed in

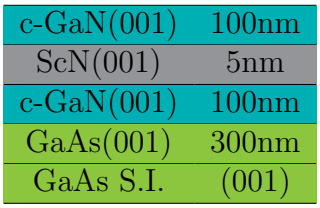

Figure 4.1 – Schematic of proposed ScN interlayer in c-GaN structure

c-GaN propagating through to ScN. Further growth of c-GaN atop a thin (lattice matched) ScN layer should provide a GaN layer vastly reduced in strain and consequentially defects. The prospect for ScN to be used as a stacking fault blocker in c-GaN is investigated in this work.

The overall aim consisted of growing a thin ScN(0 0 1) interlayer (a few nm) in thick c-GaN(0 0 1), represented by figure 4.1. In order to confidently assign XRD peaks, optimise growth conditions and assess structural parameters of each layer, the growth was carried out in three stages; whereby each stage represented incremental growth adding layers sequentially to generate the final structure.

4.4.1 Growth details, results and discussion

c-GaN(100)

A set of five c-GaN samples were grown for 2 hrs at a substrate temperature of 680 °C with varying Ga:N flux ratios, in order to find the point at which optimal structural growth occurs [74]. The Ga effusion cell temperature was set to give BEP in the region of $1.8 \times 10^{-7} - 9.0 \times 10^{-7}$ mbar.

On completion of a GaAs buffer layer (using Ga flux of 1.8×10^{-7} mbar), the gallium shutter was closed and the nitrogen plasma source was struck at 200W and allowed to stabilize for a few minutes. GaN growth was initiated following a 15 sec pre-nitridation of the GaAs surface. Following the start of GaN growth, the plasma source was tuned to 450W, the As shutter closed and source cooled, and substrate temperature increased to $\sim$ 680 °C. After 18 mins the Ga cell temperature was raised to give the required flux value. This process, of initiating growth under nitrogen-rich conditions in the presence of As, is carried out to ensure that the cubic GaN polytype is obtained, and not the wurtzite form [75].

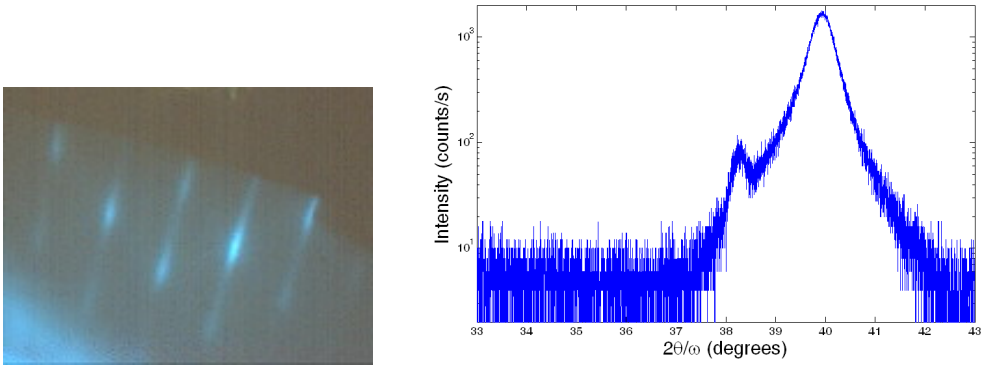

(a) RHEED (b) $2\theta/\omega$ linescan

Figure 4.2 – (a) RHEED pattern after growth and (b) $2\theta/\omega$ linescan for c-GaN(001)/GaAs(001) (JH31).

RHEED studies at the end of growth showed all samples had four-fold symmetry, demonstrating that cubic material has been formed; h-GaN has no planes which would give rise to four-fold symmetry. Determining whether growth was performed under nitrogen or gallium-rich conditions was done by visual inspection. Gallium droplets can be seen on the surface if growth is performed under gallium-rich conditions. These films are characterised as possessing a 'milky' appearance.

Optimised growth conditions were established for a Ga flux of 4.0×10^{-7} mbar (sample JH31). This represents the highest flux for a sample obtained that is visibly clear of Ga droplets and also, the only film to display a streaky RHEED pattern at the end of growth (figure 4.2(a)), indicating that c-GaN layer had grown in a 2D growth mode. FWHM values from peaks in rocking curves and $2\theta/\omega$ linescans taken aligned on the 002 c-GaN(100) reflection, along with surface roughness values, can be found in figure 4.3. These also show that a cell temperature of $\sim 1005\,^{\circ}$C (flux 4×10^{-7} mbar) gives optimal structural properties for c-GaN(001). Thickness measurements performed by analysing ORS results, give a growth rate of ~ 230 nm/hr. Unless stated otherwise, this Ga flux was used for all further samples containing GaN. Sample JH31 is used as a reference for c-GaN growth on GaAs(001) substrates.

Figure 4.2(b), shows a $2\theta/\omega$ XRD linescan taken between 2θ values of 33° and 43°. A peak at $\sim 40°$ confirms that cubic GaN(0 0 1) [76] material has been achieved. The smaller peak at $\sim 38.4°$ originates from the aluminium sample stage. Since wurtzite inclusions are a known problem in the growth of c-GaN [77], a partial plot

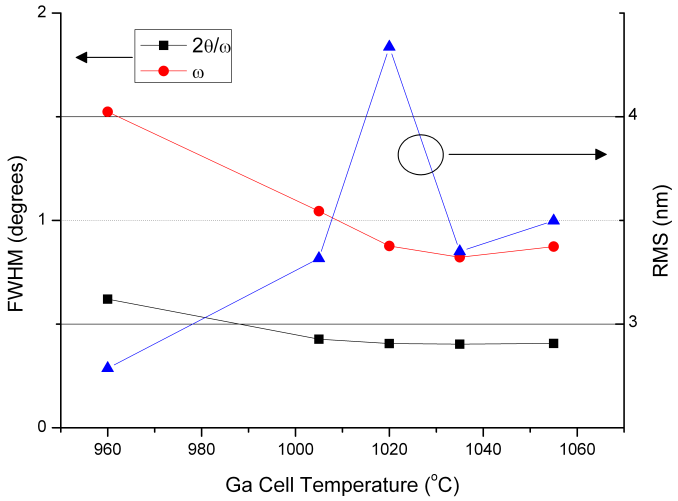

Figure 4.3 – RMS surface roughness values (from AFM) and FWHM values from (i) ω rocking curves and (ii) $2\theta/\omega$ XRD scans of the 002 reflection of c-GaN(001)/GaAs(001), shown as a function of gallium cell temperature.

around GaN (1 0 5) reflection was also performed. The scan (not shown) shows no additional peaks compared to a scan of GaAs, demonstrating that the GaN layer has a negligible wurtzite content as determined by XRD.

Figure 4.4(a) shows a RSM aligned on the symmetrical c-GaN 002 reflection. The GaN(0 0 2) peak is as expected, significantly wider in both ω and $2\theta/\omega$, indicating reduced crystal quality with respect to the substrate and a high degree of mosacity. In addition, there are low intensity extensions directed along $y = x$ and $y = -x$. The $y = x$ diagonal streak is attributed to instrumental effects, due to the use of the open detector (as opposed to the analyser crystal) in obtaining the data. A streak running along $y = -x$ can be seen if no monochromator is used, however since this is not the case, the feature is attributed to the c-GaN layer. Further support for this assumption arises from the fact that the streak is asymmetrical, a feature suggesting the presence of tilted planes. Looking at a stereographic projection for the cubic (001) orientation system (figure 4.5), it can be seen that the streak is running towards the 111 reflection, possibly indicative of stacking faults in this direction.

A RSM aligned on the asymmetrical c-GaN(1 1 1) reflection, figure 4.4(b), shows the c-GaN peak vertically aligned to the GaAs peak. This means that GaN has grown strained, such that, it is apparently latticed matched to the GaAs substrate,

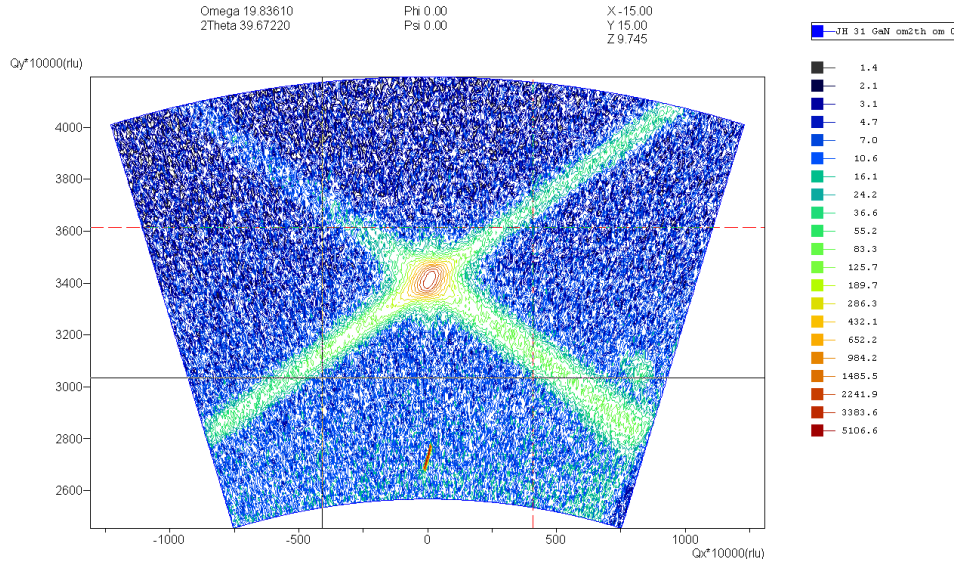

(a) c-GaN(0 0 2)

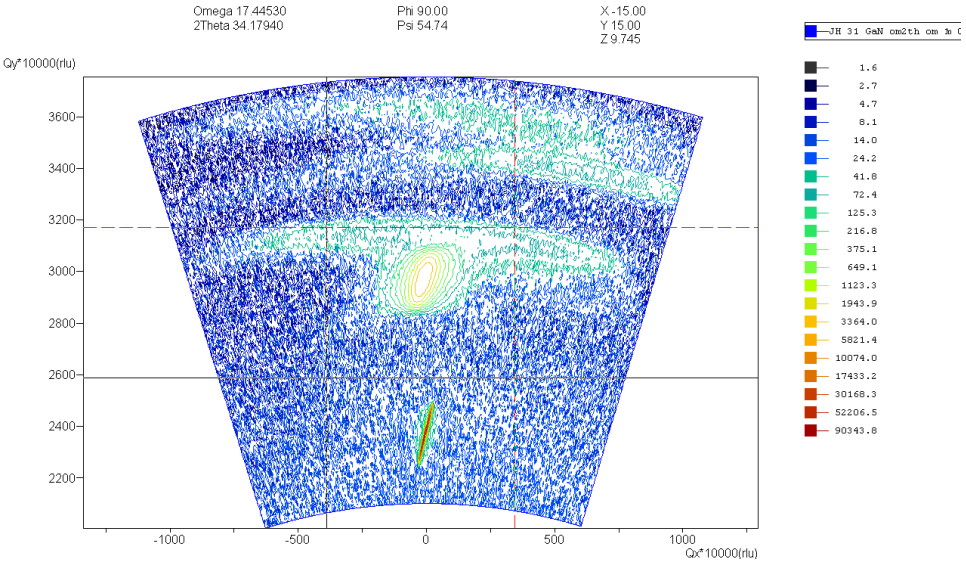

(b) c-GaN(1 1 1)

Figure 4.4 – Reciprocal space maps of the symmetric c-GaN 002 and asymmetric c-GaN 111 Bragg reflections of c-GaN(0 0 1) /GaAs(0 0 1) (JH31). Scans were taken using a high-resolution detector with a 1° slit placed in front.

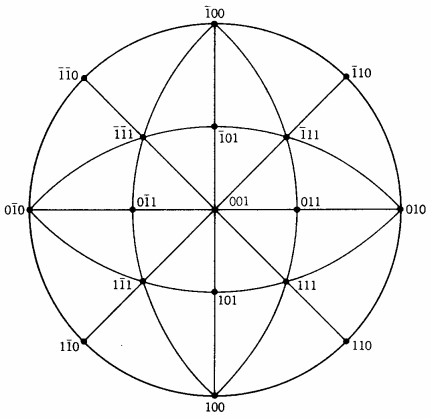

Figure 4.5 – Stereographic projection for the cubic system (001) orientation.

i.e. the in-plane lattice parameters appear identical. Three additional peaks can be seen at 2θ values (found by a projection to the x axis) of 36.75°, 40.32° and 42.76°. These peaks are attributed to the presence of gallium droplets on the surface, and are assigned to $Ga_{cubic}(211)$, $Ga_{tetragonal}(002)$ and $Ga_{cubic}(220)$ respectively. The gallium peaks are of low intensity and exhibit a wide ω spread. This is to be expected; the integrated intensity is a function of material volume, and there is no reason for gallium droplets to be a uniform size.

ScN on c-GaN(001)

To investigate how the growth of ScN on c-GaN(001) depends on Sc:N flux ratios, a series of 2 hr ScN films were grown at 680 °C, using Sc BEP in the range $6 \times 10^{-8} - 4.5 \times 10^{-7}$ mbar (requiring cell temperatures > 1300 °C). The c-GaN layer was grown for 1 hr, using conditions described in the previous section, ScN growth was initiated by simply switching Ga and Sc shutters. A bulk ScN layer was grown to ensure there was sufficient material for characterisation.

RHEED studies at the end of growth showed that all films had, unexpectedly, a six-fold symmetry, implying that on c-GaN(0 0 1), ScN grows with a twinned (1 1 1) orientation and not (0 0 1), as the literature would suggest. The RHEED pattern obtained was characteristic of rock-salt ScN [78], with bright spotty diffraction features (figure 4.6(a)), indicative of growth in a 3D mode. The optimum Sc cell temperature was ascertained, from visual inspection of the samples, to correspond to a flux of 2×10^{-7} mbar (sample JH35), which was used for all further Sc con-

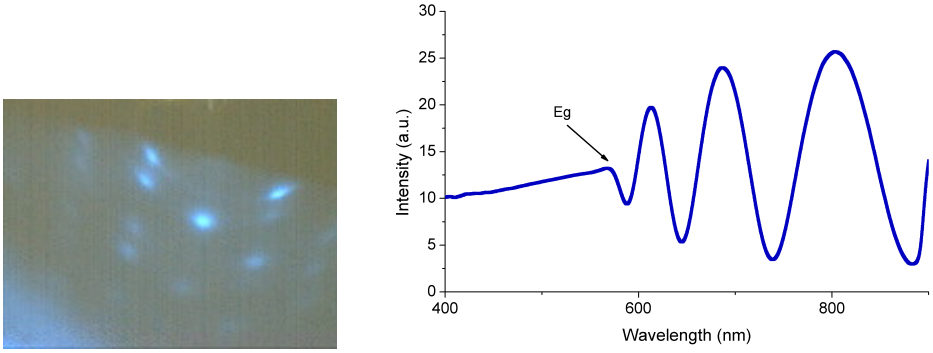

(a) RHEED (b) ORS

Figure 4.6 – Typical RHEED pattern after growth (a) and a typical example of an optical absorption measurement (JH163) (b) for ScN/c-GaN/GaAs (JH44). The onset of absorption is used to determine the bandgap, E_g.

taining samples, unless otherwise stated. It is notable that this value is half the optimum Ga value, supporting a calculated gauge sensitivity factor of 0.5 for Ga to Sc.

Another series was grown, investigating whether growth temperature has an effect on the orientation of ScN deposited on c-GaN(0 0 1). ScN films were again grown for 2 hrs, at substrate temperatures ranging from 480-680 °C. All ScN layers were initiated at 680 °C, the substrate temperature was then immediately lowered to the required value. Material quality was found to worsen with decreasing growth temperature, as witnessed by the RHEED pattern showing an increasingly polycrystalline character. All samples however, retained a six-fold symmetry, indicating a (1 1 1) orientation of ScN on c-GaN(001), invariant to growth temperature or flux ratio.

ORS were performed on all samples, with a typical ScN result shown in figure 4.6(b). Results give a bandgap value for ScN between $2.13 - 2.19$ eV, in agreement with the literature [62]. Since the refractive index for ScN is not well known, ORS studies cannot be used for growth rate determination.

A typical XRD result for ScN/c-GaN/GaAs is shown in figure 4.7. The $2\theta/\omega$ linescan, shows with respect to c-GaN samples, the presence of an additional peak at a 2θ position of $\sim 34.5°$, corresponding to a (1 1 1) reflection in c-GaN and hence also in ScN. A partial pole plot, with 2θ positioned to access the $\langle 1\,1\,1 \rangle$ set of planes, see figure 4.8(a), was performed to illustrate the symmetry and assess

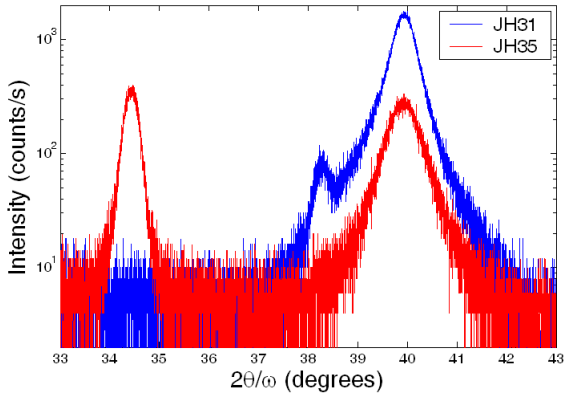

Figure 4.7 – $2\theta/\omega$ linescans of JH31 - GaN/GaAs (blue) and JH35 ScN/GaN/GaAs (red).

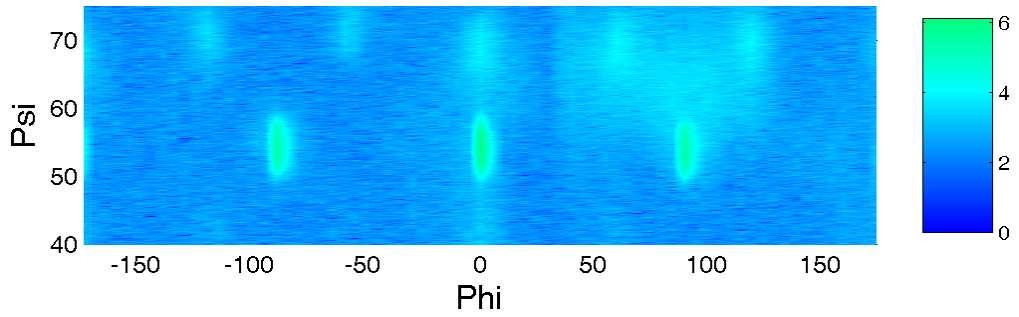

(a) JH35 - ScN(1 1 1)/c-GaN(0 0 1)/GaAs(0 0 1)

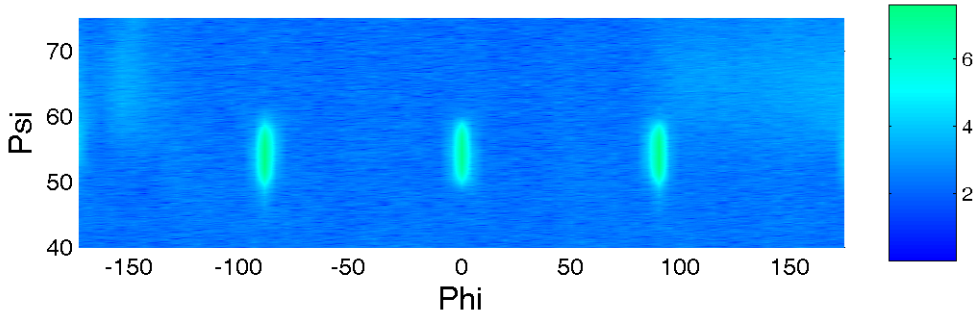

(b) JH31 - c-GaN(0 0 1)/GaAs(0 0 1)

Figure 4.8 – Partial pole plots (ϕ-ψ maps) of the c-GaN 111 Bragg reflection. Scans were taken using a high-resolution detector with a 1° slit placed in front.

the degree of twinning. For cubic (0 0 1) oriented material, this scan should show four-fold symmetry, while for (1 1 1) it should show three- or six-fold, depending whether there is twinning present. A scan for comparative purposes was also performed on JH31 and is shown in figure 4.8(b). In the partial pole plot for JH35, two distinct symmetries can be observed, a four-fold symmetry along $\psi \sim 55^\circ$ and a six-fold along $\psi \sim 70^\circ$. Since the peaks aligned along $\psi \sim 55^\circ$ are present in both the JH31 and JH35 scans, the six peaks aligned along $\psi \sim 70^\circ$ can be confidently assigned to the ScN layer. Integrated intensities were calculated to determine the degree of twinning, the volume fraction of the two twins was found to occur in the ratio 1:1. The four-fold symmetry was confirmed as originating from the c-GaN layers by performing a scan on GaAs (not shown), which showed no peaks of significant intensity.

This information confirms that ScN has grown with a twinned (1 1 1) orientation on c-GaN(0 0 1); the reasons behind which remain unclear. This appears to be the first instance of single crystalline ScN not inheriting its texture from the layer it was grown on.

At the request of the University of Warwick, a series of ScN films with varying thicknesses were grown, in order to asses whether there is a relationship between the number of free carriers, n, and thickness. Thin films (order of a few nm's) were also requested for XPS measurements. Summary of results from these films are displayed in table 4.1. Only RMS surface roughness (RMS) and FWHM values from the ScN(111) peak in a $2\theta/\omega$ linescan were found to significantly change with thickness, these results are plotted in figure 4.9. As expected, with increasing thickness surface roughness is seen to increase, while $2\theta/\omega$ FWHM decreases, in agreement with results reported by Moram et al. [73]. Resistance and carrier concentration values were found to be in the region of a few kΩ's and 10^{19}cm^{-3} respectively. The thin samples gave no measurable resistance or carrier concentration, and no peaks due to ScN in the $2\theta/\omega$ X-ray scans were observed.

ScN interlayers in GaN

Growth of GaN on thin layers of ScN(1 1 1) grown on c-GaN(0 0 1) was investigated, with varying thicknesses of ScN from 1-15 nm. This is the ScN interlayer in a GaN structure proposed earlier (page 73). Both GaN layers were grown for 1 hr and all growth conditions have been described previously.

Sample	Growth time	R $\pm$100 (Ω)	RMS	n (cm^{-3})	FWHM (°)
JH 165	45 secs	-	1.5nm	-	no peak
JH 166	60 secs	-	1.6nm	-	no peak
JH 167	1 hr	1800	2.0nm	$4.8x10^{19}$	0.34898
JH 159	1 hr 30	5400	2.5nm	$7.3x10^{18}$	0.34731
JH 163	2 hrs	900	6.3nm	$4.7x10^{19}$	0.2952
JH 169	2 hrs 30	2900	6.9nm	$1.1x10^{19}$	0.2459
JH 168	3 hrs	1300	10.0nm	$7.3x10^{19}$	0.25629

Table 4.1 – Results summary of ScN films (of varying thickness) grown on c-GaN(001)/GaAs(001).

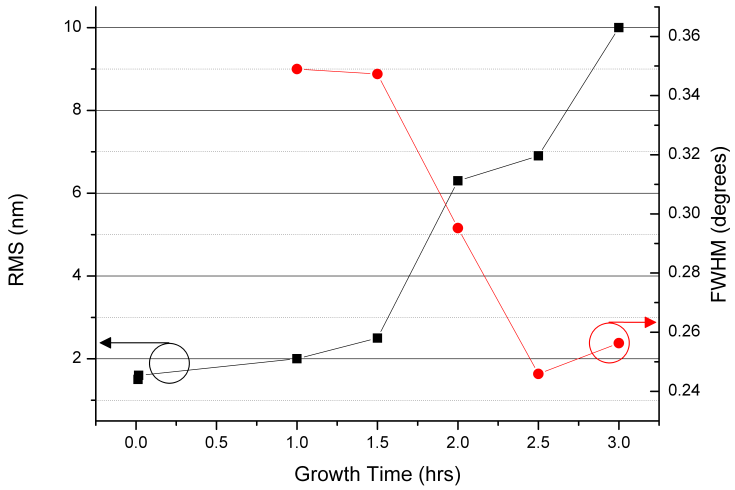

Figure 4.9 – RMS surface roughness values from AFM (black squares) and FWHM values (red circles) of the ScN(111) peak in $2\theta/\omega$ linescans of ScN$(1\,1\,1)$/c-GaN$(0\,0\,1)$/GaAs$(0\,0\,1)$, shown as a function of ScN thickness.

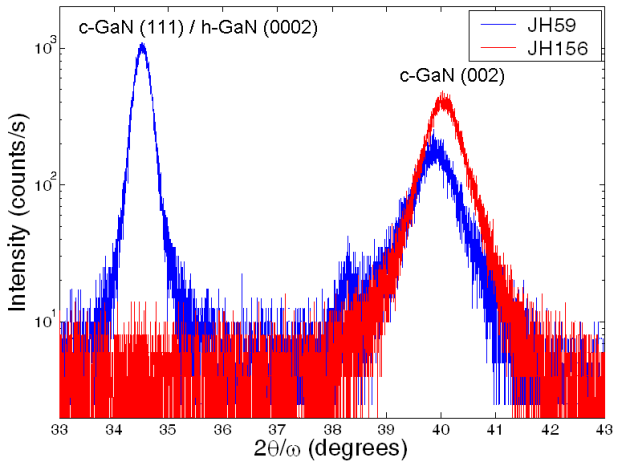

Figure 4.10 – A $2\theta/\omega$ linescan of GaN/ScN/c-GaN(0 0 1)/GaAs(0 0 1) for ScN thickness of 5 nm (JH59) blue curve and 1 nm (JH156) red curve.

For samples of interlayer thicknesses greater than or equal to 5 nm, the RHEED displayed a six-fold symmetry at the end of growth. A $2\theta/\omega$ linescan of JH59 (ScN 5 nm) (figure 4.10) shows the presence of a strong peak at $2\theta \sim 34.5°$. This is attributed to diffraction from the top GaN layer, since the ScN layer is very thin. However, it could be assigned as either c-GaN(111) or h-GaN(0002). A 105 partial pole plot, see figure 4.11(a), highlights an additional set of six peaks (compared to JH35, figure 4.11(b)) along $\psi \sim 20°$, showing that GaN grown on ScN(111) grows in the wurtzite polytype. The 5 peaks which are seen to repeat four times are attributed to GaAs; this was confirmed by performing a 105 partial pole plot on a piece of GaAs substrate, figure 4.11(c).

A TEM image along a $\langle 1\,1\,0 \rangle$ direction of JH59 is shown in figure 4.12(a). Stacking faults formed in the c-GaN layer can be seen running along $\{1\,1\,1\}$ planes. The scan clearly shows that these stacking faults terminate at the ScN interface and are not transmitted through to the subsequent GaN layer. The top GaN layer however, is very defective material which exhibits a columnar structure, a feature characteristic of h-GaN grown under nitrogen-rich conditions [35]. The scan also highlights the highly defective nitrogen-rich region of c-GaN and shows that the ScN layer has a significant degree of 'waviness'.

Interlayer structures of thicknesses greater than 5 nm where (i) the Ga shutter was left open during growth of Scthe ScN layer and (ii) arsenic was present during second GaN layer, were also grown. These samples showed no structural improvement, as assessed by the RHEED pattern after growth, and will not be discussed

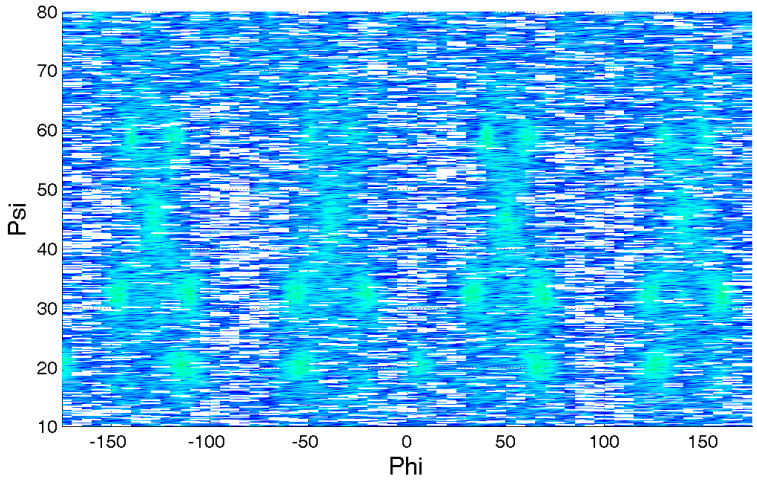

(a) JH59 GaN/5 nm ScN(111)/c-GaN(001)/GaAs(001)

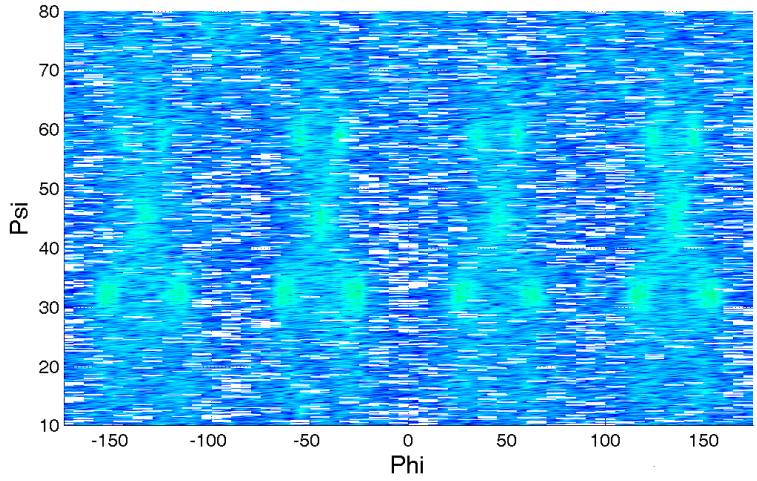

(b) JH35 500 nm ScN(111)/c-GaN(001)/GaAs(001)

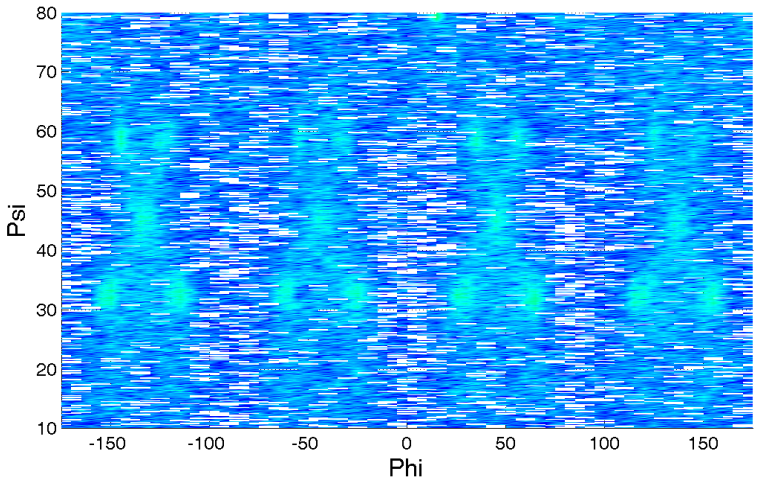

(c) GaAs(001)

Figure 4.11 – Partial pole plots from 2θ and ω aligned on the 105 Bragg reflection of h-GaN. Scans were taken using a high-resolution detector with a 1° slit placed in front.

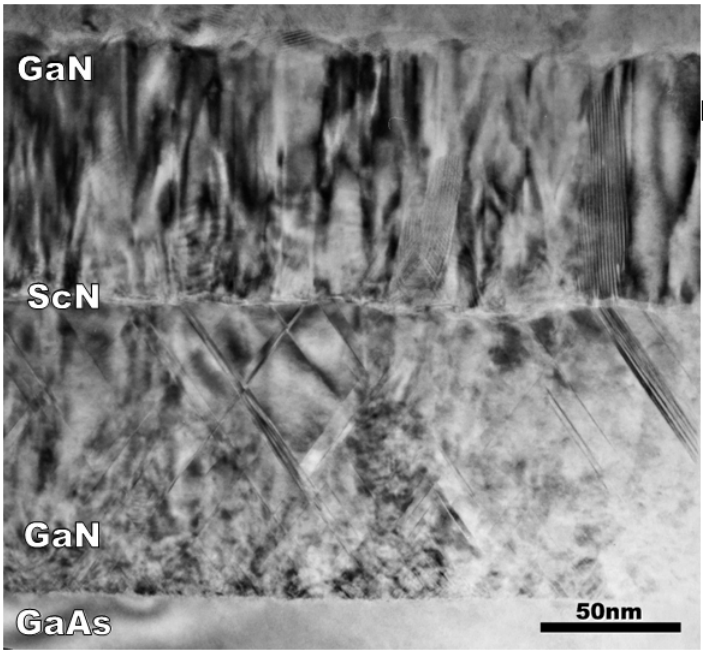

(a) JH 59 ScN 5 nm

(b) JH 156 ScN $\sim$ 1 nm

Figure 4.12 – TEM bright field 004 images taken along $\langle 1\,0\,0 \rangle$ direction of GaN(100 nm)/ScN(x)/c-GaN(100 nm)/GaAs(001) for (a) $x = 5$ nm and (b) $x = 1$ nm.

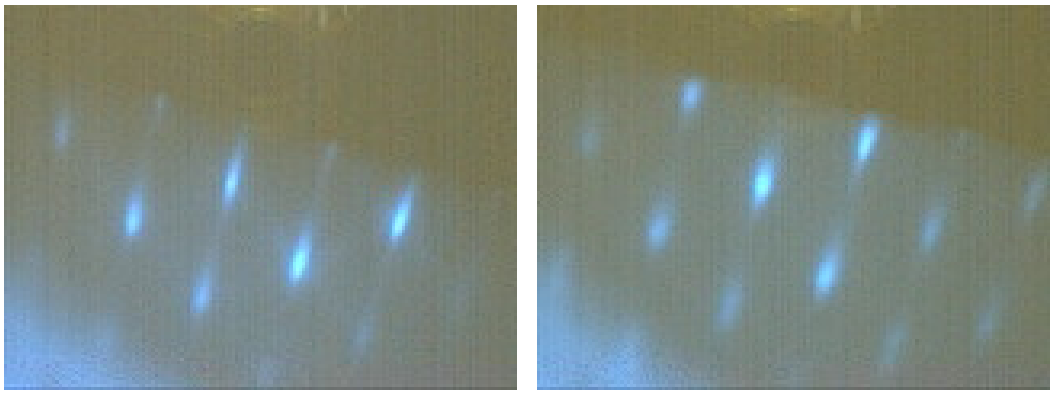

(a) [1 1 0] azimuth (b) [1 $\bar{1}$ 0] azimuth

Figure 4.13 – RHEED pictures taken after growth of JH156 (1 nm ScN interlayer in c-GaN(0 0 1)), showing cubic symmetry and a spotty pattern with streaky extensions. Azimuths are with respect to GaAs(0 0 1).

further.

Interlayer samples with ScN thicknesses in the order of 1nm were grown. In this case incomplete ScN layers should form, allowing the subsequent GaN layer to nucleate on the exposed c-GaN underlayer, and hopefully inherit its registry. The four-fold symmetry observed in RHEED (figure 4.13) and a peak at $2\theta \sim 40.0°$ in XRD (figure 4.10) both confirm that the final surface of these structures is c-GaN(0 0 1). TEM analysis (figure 4.12(b)) however, shows the top GaN layer has no significant improvement in defect density compared to the bottom GaN layer. Surface roughness was also found to be unchanged at 3.4 nm cf. 3.3 nm for JH31 (2 hr c-GaN on GaAs). By growing a stacked interlayer sample with increasing ScN thickness, the transition for the top GaN growing cubic or wurtzite was found to occur between ScN interlayer thicknesses of 3.3 and 5 nm.

4.5 ScN/GaAs(0 0 1)

In order to achieve growth of c-GaN(0 0 1) on top of ScN, it was assumed that ScN would be required in a (0 0 1) orientation. With this in mind, growth of ScN on different materials was investigated, initially on GaAs.

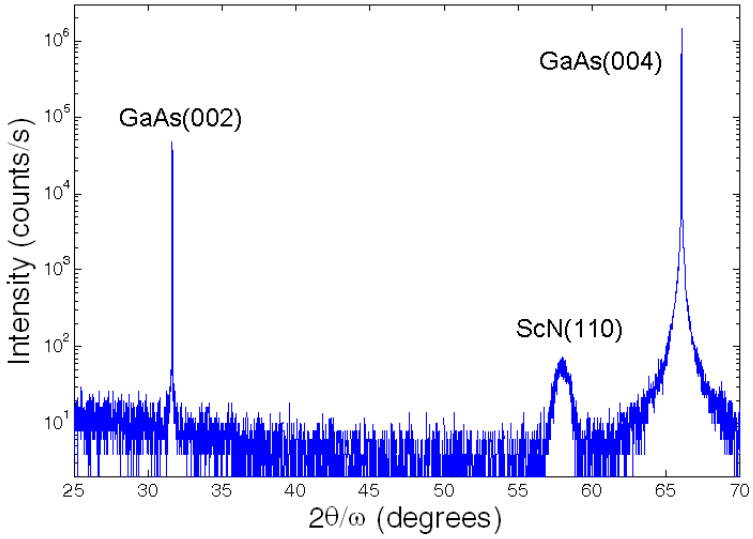

Figure 4.14 – A $2\theta/\omega$ linescan of ScN/GaAs(001) showing ScN has grown in a (1 1 0) orientation.

4.5.1 Growth detail, results and discussion

A series of films with varying initial nucleation conditions was investigated for the 2 hr growth of ScN on GaAs (with and without GaAs buffer layers and hence with or without an arsenic background). The substrate temperature was raised to $\sim 680\,^{\circ}\mathrm{C}$ following the start of ScN growth. Growth of ScN was initiated with varying times of either pre-nitridation or deposition of Sc onto the GaAs surface.

Most films had a six-fold symmetry at the end of growth, but with poorly defined RHEED patterns. XRD analysis also shows the material quality of these films to be poor. $2\theta/\omega$ linescans showed small intensity peaks at a variety of ScN reflections, indicating an almost amorphous material with some degree of polycrystallinity. For one sample however (ScN initiated with a 10 sec deposition of Sc), the RHEED pattern showed a peculiar four-fold symmetry following growth. It was found by XRD, figure 4.14, that the ScN layer had grown with a (1 1 0) orientation. Growth of a subsequent ScN(1 1 0) sample was attempted using the same nominal conditions, the final orientation however, was (1 1 1). This would suggest that a narrow window of conditions exist for growth of ScN in a (1 1 0) orientation on GaAs(0 0 1).

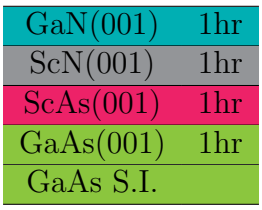

Figure 4.15 – Schematic of modified proposed structure for achieving growth of ScN(0 0 1).

4.6 ScN/ScAs

Further attempts at achieving growth of c-GaN(0 0 1)/ScN(0 0 1) centered on growing ScN on a ScAs buffer layer. A cursory literature survey reveals very little information on ScAs, with no consensus between theory and experiment on whether ScAs is in fact a semiconductor or a semimetal. Growth by vapor phase epitaxy was performed in 1971 by Yim et al. [79] on Si substrates. They reported that ScAs was a rock-salt semiconductor with a bandgap of 0.7 eV and a lattice parameter of 5.464 Å(cf. GaAs 5.653 Å). It was also found to have a n-type carrier concentration in the order of 2-6 $\times 10^{21}$ cm^{-3}, with mobilities in the range of 10-30 cm^2/Vs and a metallic grey appearance. MBE growth of ScAs on GaAs(0 0 1) was performed at a nominal substrate temperature of 430 °C in 1994 by Lepine et al. [80]. RHEED oscillations were observed, while the RHEED pattern itself, showed a 1x1 reconstruction after deposition of about 3 ML. As the films were for X-ray photoelectron diffraction studies, thicknesses were less than 5 ML. Though the authors state that bulk epitaxial film growth can be achieved without difficulty, despite the 3.3% lattice mismatch, no information regarding such films appears.

Recent theoretical studies on Sc containing compounds, calculate that ScAs has a rock-salt structure with a lattice mismatch to GaAs of $\sim$ 3.3% ($a_0 \sim 5.46 - 5.49$ Å) [81–83], in agreement with experimental studies. They also however, consistently calculate that ScAs is a semi-metal. It is worth noting though, that until very recently, these studies also predicted that ScN was a semi-metal.

The growth model was modified from section 4.4 such that, a ScAs layer replaces the first c-GaN layer in the initial proposed structure, figure 4.15. The growth was once again split up into three stages, in order to analyse the structure layer by layer. For samples discussed after this point, the substrate temperature was monitored by a kSA BandiT system.

4.6.1 Growth details, results and discussion

ScAs

ScAs was deposited for 1 hr (sample JH170) after which, RHEED studies showed a streaky 1x1 reconstruction with four-fold symmetry (figures 4.16(a) & 4.16(b)). Upon starting ScAs growth, the substrate temperature was found to rise rapidly from 570 °C to 710 °C in less than 7 mins. Once the substrate temperature reached 700 °C, the heater power was manually controlled in order to stabilise the temperature and prevent evaporation of the GaAs substrate. The temperature evolution of the substrate during growth is shown in figure 4.17. Such an increase in temperature is not unexpected, considering ScAs is predicted to possess a high carrier concentration and a narrow bandgap. The sample was found to have a metallic appearance with a resistance of 50Ω, indicating that the sample is highly conducting. This was confirmed by Hall bar measurements performed at the University of Warwick, which gave a carrier concentration of 6×10^{21} cm^{-3} and a mobility of 15 cm^2/Vs, in agreement with the literature.

A $2\theta/\omega$ linescan of JH170 about the symmetric GaAs 004 reflection, shown in figure 4.18, shows two distinct peaks. The high intensity peak corresponds to the GaAs substrate and includes contributions from the buffer layer. The lower intensity peak at a 2θ angle of $\sim 68.7°$ relates to the ScAs layer. Analysis of the peak positions yields perpendicular lattice constants for GaAs and ScAs as 5.654 Åand 5.460 Årespectively, in agreement with the literature. A RSM taken about the asymmetric GaAs 444 reflection, figure 4.19, shows that the ScAs layer has almost fully relaxed. The $2\theta/\omega$ and ω FWHM's of the ScAs peak are significantly wider than those of the GaAs substrate.

Unfortunately, no XRD or AFM data has been found in the literature that can be used for comparison. There has been a SEM image presented with dimensions 100 x 100μm, which showed well oriented growth of four-sided pyramids [79]. No analysis of surface roughness was presented.

AFM shows relatively rough surfaces for ScAs, with a RMS surface roughness of 4 nm, despite the streaky nature of the RHEED pattern. This combined with the fact the ScAs is not fully strained demonstrates that there may be room for improvement in the growth method. This is not surprising considering the

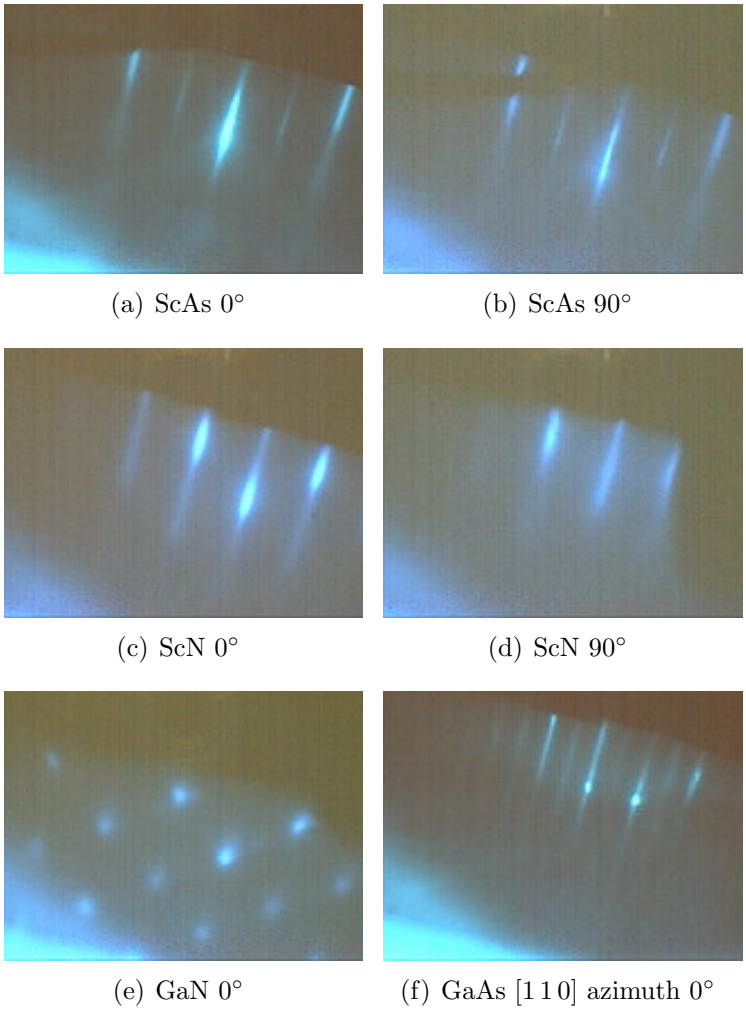

(a) ScAs 0° (b) ScAs 90°

(c) ScN 0° (d) ScN 90°

(e) GaN 0° (f) GaAs [1 1 0] azimuth 0°

Figure 4.16 – Various RHEED patterns, 12keV primary beam energy, observed during the growth of JH173 (GaN/ScN/ScAs/GaAs). Angles are measured with respect to the [1 1 0] azimuth

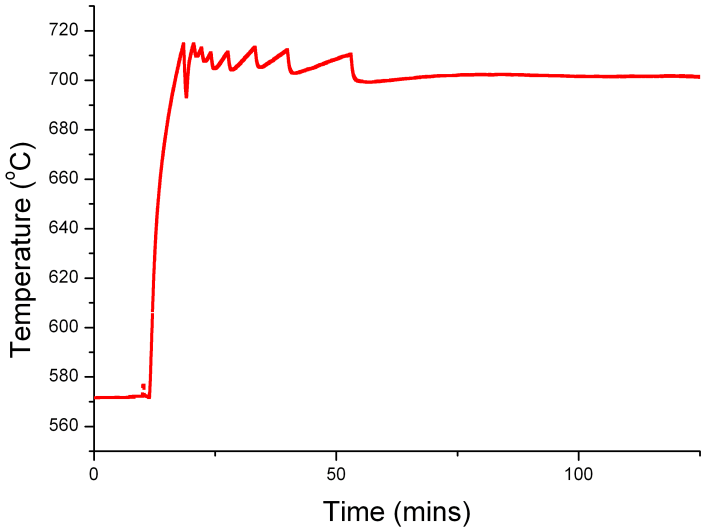

Figure 4.17 – Temperature evolution during the growth of JH170 (ScAs/GaAs$(0\,0\,1)$), as measured by kSA BandiT.

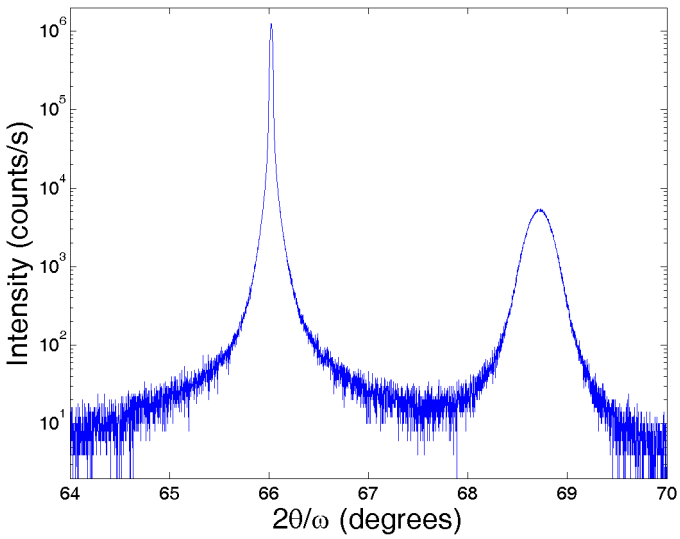

Figure 4.18 – A $2\theta/\omega$ linescan of ScAs/GaAs$(0\,0\,1)$ about the symmetric GaAs 004 Bragg reflection

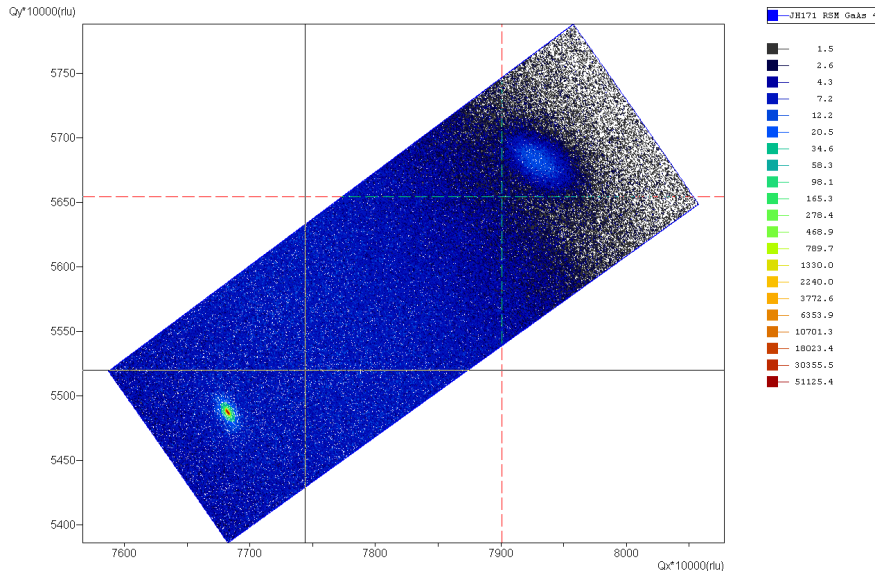

Figure 4.19 – Reciprocal space map of the asymmetric GaAs 444 Bragg reflection of ScAs/GaAs(0 0 1), taken using the triple-axis detector.

growth temperature and Sc flux used were relatively arbitrary and that no growth parameters were explored.

Resistance measurements taken of the ScAs sample at room temperature and 77K, give values of 12 and 15Ω respectively. For a semiconductor, resistance is dominated by free carriers. Decreasing the temperature leads to these carriers freezing out, so you typically expect the resistance to increase with decreasing temperature. In a semi-metal however, the resistance is dominated by phonons, and is expected to remain relatively unchanged with changing temperature. The resistance measurements would therefore suggest, that ScAs is a semi-metal, in agreement with the theoretical publications.

ScN on ScAs(001)

A 1 hr growth of ScN (JH171) on ScAs(0 0 1) was carried out. Nitride growth was initiated using the same conditions described for c-GaN (section 4.4.1), except that a nominally stoichiometric Sc flux was used throughout. As following the growth of ScAs the substrate temperature was already at 700 °C, it did not need to be raised. It was found that, if left unsupervised, the temperature during the growth of ScN decreased gradually over time; a small amount of manual control was required to keep the temperature stable. On completion, the RHEED screen

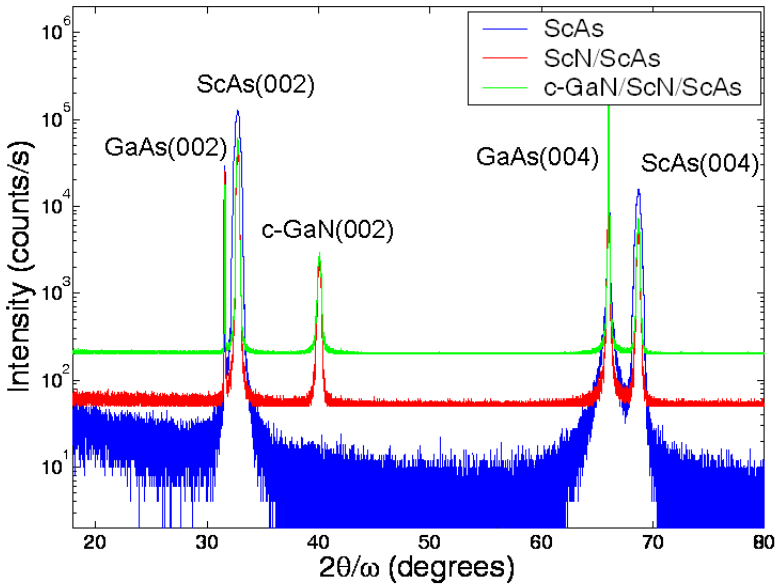

Figure 4.20 – $2\theta/\omega$ linescans of samples representing sequential growth of GaN/ScN/ScAs/GaAs.

showed a streaky pattern with a very promising, four-fold symmetry, figures 4.16(c) & 4.16(d).

A wide-range $2\theta/\omega$ linescan of JH171 is displayed in figure 4.20 and shows, in addition to the GaAs and ScAs related peaks, a peak at $2\theta \sim 40°$ confirming that ScN has finally been grown in a (0 0 1) orientation. ScN grown in this manner is the only method investigated which shows growth in a 2D mode, in agreement with the literature [71]. The RMS surface roughness of JH171 was found to be 1.5 nm Although not a surface consisting of atomic steps as reported by Al-Brithen and Smith [71], for a un-optimised growth system, it is a respectable start. Analysis of XRD and AFM results also show that ScN(0 0 1) has better crystallinity than ScN(1 1 1); with values for $2\theta/\omega$ FWHM of 0.35° and 0.31° and RMS surface roughness of 2.0 nm and 1.5 nm for ScN(1 1 1) and ScN(0 0 1) respectively.

GaN on ScN(001)

Finally, the growth of GaN/ScN/ScAs/GaAs (JH173) was investigated, using a gallium flux of 3.8×10^{-7} mbar. All layers, including the GaAs buffer layer, were grown for 1 hr. A four-fold symmetry in the RHEED pattern was observed

throughout, the pattern itself was spotty, indicating cubic but 3D growth, figure 4.16(e). A $2\theta/\omega$ X-ray linescan, shown in figure 4.20, shows no additional peaks to those witnessed during growth of ScN(0 0 1)/ScAs(0 0 1) demonstrating that both the ScN and GaN layers have grown with a cubic (001) orientation. The FWHM of the c-GaN(002) peak is identical to that of ScN(0 0 2) from JH171, i.e. XRD does not detect a deterioration in material quality. 1μm by 1μm AFM images however, do show a reduction in material quality between the layers with a RMS surface roughness value increasing from 1.5 nm (JH171) to 4.5 nm on completion of the c-GaN layer. It is however expected that better c-GaN(0 0 1)/ScN(0 0 1) material quality can be obtained with some exploration of growth parameters.

Partial pole plots (not shown) around the 105 reflection of h-GaN and the 111 reflection in c-GaN, have been taken for both JH171 and JH173. Results from the 105 pole plot show no additional peaks other than those due to diffraction from GaAs. Despite the worsening quality of c-GaN(001) grown on ScN(001) cf. GaAs(001), there is still no evidence for the presence of wurtzite inclusions. The 111 pole plots both show the same four-fold pattern witnessed in the scan of c-GaN(0 0 1)/GaAs(001) confirming that both samples have cubic symmetry.

4.7 ScGaN

One of the most obvious ways of producing efficient solid-state white lighting, is the combination of individual efficient red, green and blue LEDs. For this approach to work however, the efficiency of deep-green LEDs, which is much less than that of red and blue LEDs, must be significantly improved. A common way of producing green light is the addition of In to GaN; materials which are already used in the production of blue LEDs. The difficulty in achieving desired efficiencies from green LEDs is commonly referred to as the 'green gap' [6] problem. Though the problem is not fully understood, it is attributed to poor material quality. Growth issues which lead to poor material quality include the low growth temperatures required to incorporate In (due to the low dissociation temperature of InN) and increased strain (due to the lattice mismatch between InN and GaN). The result being that green LEDs produced are too dim to be used.

The addition of Sc into GaN would decrease the bandgap. As the bandgap of ScN is wider than In, smaller amounts of Sc would be required in order to achieve green

emission in GaN. ScGaN therefore offers possible advantages as an alternative to the InGaN material system. Also, the higher growth temperatures and good lattice match could reduce the tendency for phase separation. The inherent physical properties of ScN and GaN, such as good strength and durability, should lead to an increased range of applications for ScGaN cf. the InGaN material system [84].

4.7.1 Previous studies of ScGaN

Although ScN has a rock-salt structure, Takeuchi [85] predicted that a metastable wurtzite phase (w-ScN) at an energy 0.34 eV higher than the rock-salt structure should exist. Farrer and Bellaiche [86] however, found that w-ScN should be unstable and calculated instead that a layered hexagonal phase having nearly five-fold co-ordination (arrived at by flattening the bilayer of the wurtzite structure) should be metastable. GaN is known to crystallise in two polytypes; the thermodynamically stable wurtzite structure and the metastable zinc blende phase.

Adli et al. [87] performed a first principle study of cubic ScGaN ternaries and calculated that a transition between rock-salt and zinc blende should occur rapidly after incorporating just a fraction of Ga of the order of 1%. However, ab initio calculations performed by Zerroug et al. [88] predict that, with Sc concentrations of 0, 25 and 50%, zinc blende is the most stable configuration, whereas for Sc concentrations of 75 and 100%, rock-salt is the most stable. Moreno-Armenta et al. [84] calculated that for Sc concentrations less than 65%, the favoured structure is a wurtzite-like one, while for Sc concentrations greater than 65%, a NaCl-like structure is favoured. These theoretical results indicate that ScN can potentially be used to fabricate superlattices with GaN, AlN and InN which crystallise in the zinc blende or the wurtzite phase [87].

As ScN and GaN have different structures, they may form a heterogenous mixture as apposed to an alloy. It has also been suggested by Dismukes and Moustakas [89] that GaN will have a higher solubility limit in ScN than ScN in GaN due to the high stability of the rock-salt structure.

Successful experimental growth of ScGaN alloys has however been reported. Little and Kordesch [90] grew ScGaN using a sputter deposition technique samples clustered around Sc concentrations of 0, 20, 70 and 100% onto quartz substrates at temperatures ranging from 300-675K. XRD showed no strong diffraction features

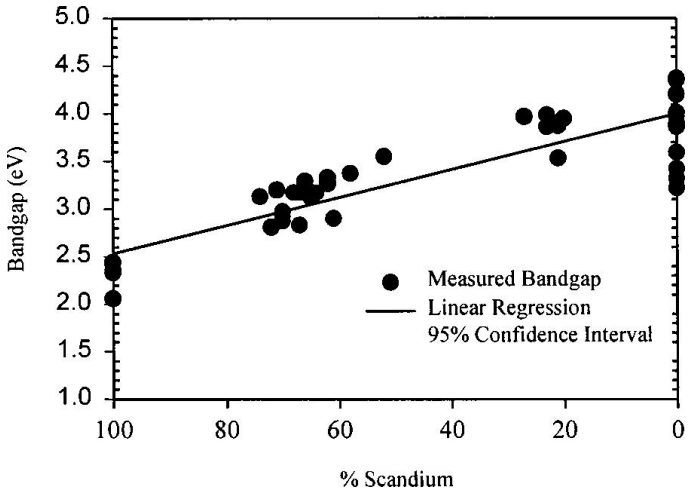

(a)

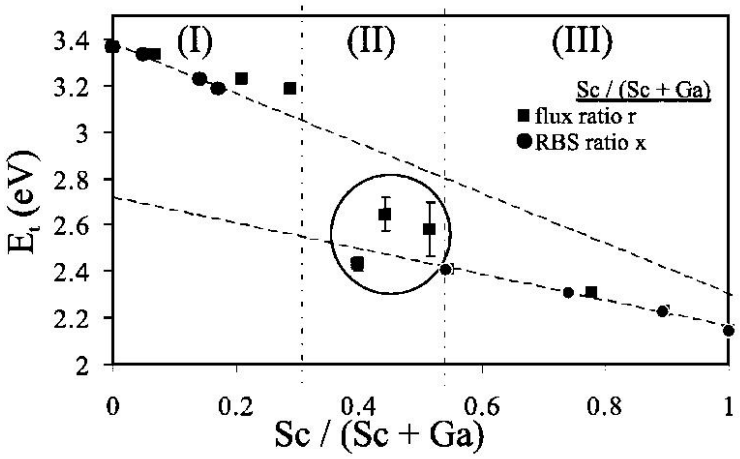

(b)

Figure 4.21 – Optical band gap of ScGaN as a function of Sc concentration as reported by (a) Little and Kordesch [90] and (b) Constantin et al. [78].

indicating that the films were amorphous or microcrystalline; this was attributed to the low growth temperatures. ORS was used to determine the bandgap and energy dispersive X-ray spectrometry for composition determination. The authors concluded that the bandgap varies linearly with composition, figure 4.21(a). Further inspection of the spread of the data at each composition cluster, suggests that determining the behaviour is actually somewhat difficult. If the average bandgap at each composition cluster point is plotted, little difference in the bandgap is observed for Sc concentrations of 20% and 0%. In addition, the extrapolated bandgap for GaN of 3.9 eV is much higher than the accepted literature value of 3.4 eV. The authors do however acknowledge, that the amorphous structure of their films led to extra features in the absorption spectra, making determination of bandgap problematic.

Constantin et al. [78] have also grown ScGaN over the whole composition range. Their compositions were more widely spread than those reported by Little and Kordesch. The deposition method was RF-MBE onto sapphire(0 0 0 1) substrates, at a growth temperature of 650 °C, under N-rich conditions, following a 15 min nitridation of the substrate surface. RHEED studies showed that for [Sc] less than 30%, a hexagonal based structure is observed while for [Sc] greater than 54% a rock-salt based structure is obtained, in agreement with the prediction by Moreno-Armenta et al. [84]. All of the Sc-rich samples showed polycrystalline character, with the exception of ScN. Lattice constants were measured using RHEED and XRD, analysis of which led to the conclusion that, for high Ga concentrations, ScGaN has a wurtzite structure with large bond distortions. This was said to support the prediction by Farrer and Ballaiche [86] of a metastable layered hexagonal phase for ScN. Compositional analysis using Rutherford backscattering consistently found lower than expected Sc values in the hexagonal regime, but good agreement in the Sc-rich regime. This suggests that the sticking coefficients of Ga and Sc differ in the two regimes, most likely due to lower surface diffusion barriers. ORS measurements, figure 4.21(b), do not show a linear dependence but rather highlight three regions of growth: low (I), intermediate (II) and high (III) Sc fractions. Regions I and III did however, show linear behaviour, indicating that in these regimes alloying is observed.

4.7.2 Outline of work

Two series of ScGaN alloy films were grown with compositions changed in nominal 20% steps: set A (or h-ScGaN) on the GaAs substrate native surface and set B (or c-ScGaN) on a 1 hr c-GaN buffer layer (grown as described in section 4.4.1). Set A was designed to give the wurtzite GaN polymorph, while growing set B was an attempt to get the c-GaN polymorph. The aims of this work were to investigate the variation of bandgap with composition and locate the composition at which switching between the two non-isocrystalline structures occurs, e.g. for h-ScGaN, h-GaN is wurtzite while ScN is rock-salt. For the cubic series, there was also the possibility that the measured perpendicular lattice parameter could change with composition. For the hexagonal series, both ScN(1 1 1) and h-GaN(0 0 0 1) give rise to X-ray peaks at the same 2θ position, therefore we expect the alloy series to have the same perpendicular lattice parameter at each composition. The cubic and hexagonal series were grown for 2 and 3 hrs respectively, at a substrate temperature of 730 °C.

4.7.3 Results and discussion

Inspection of the RHEED patterns after growth, shows that, with the exception of h-GaN, all compositions of h-ScGaN exhibit some degree of polycrystallinity. The ScN and $Sc_{0.8}Ga_{0.2}N$ samples, both show a typical rock-salt ScN pattern. The $Sc_{0.4}Ga_{0.6}N$ and $Sc_{0.2}Ga_{0.8}N$ samples meanwhile, show a rock-salt like pattern, but the non-integer features differ in their relative positions, possibly indicating an intermediate structure. The $Sc_{0.6}Ga_{0.4}N$ sample on the other hand, shows very weak features representative of a more amorphous structure. The pattern of h-GaN however, indicates a single-crystalline structure albeit grown in a 3D growth mode. The structural symmetry of the samples was either six-fold or was not possible to ascertain (e.g. pattern invariant to rotation or diffraction feature too weak).

Samples in the cubic series showed six-fold symmetry for Sc compositions down to and including 40%, which coincides with when the resistance becoming unmeasurable. The RHEED results mirror the h-ScGaN case. ScN and $Sc_{0.8}Ga_{0.2}N$ show rock-salt patterns, the $Sc_{0.6}Ga_{0.4}N$ sample indicates an amorphous structure (which is not entirely unexpected at high intermixing compositions), $Sc_{0.4}Ga_{0.6}N$

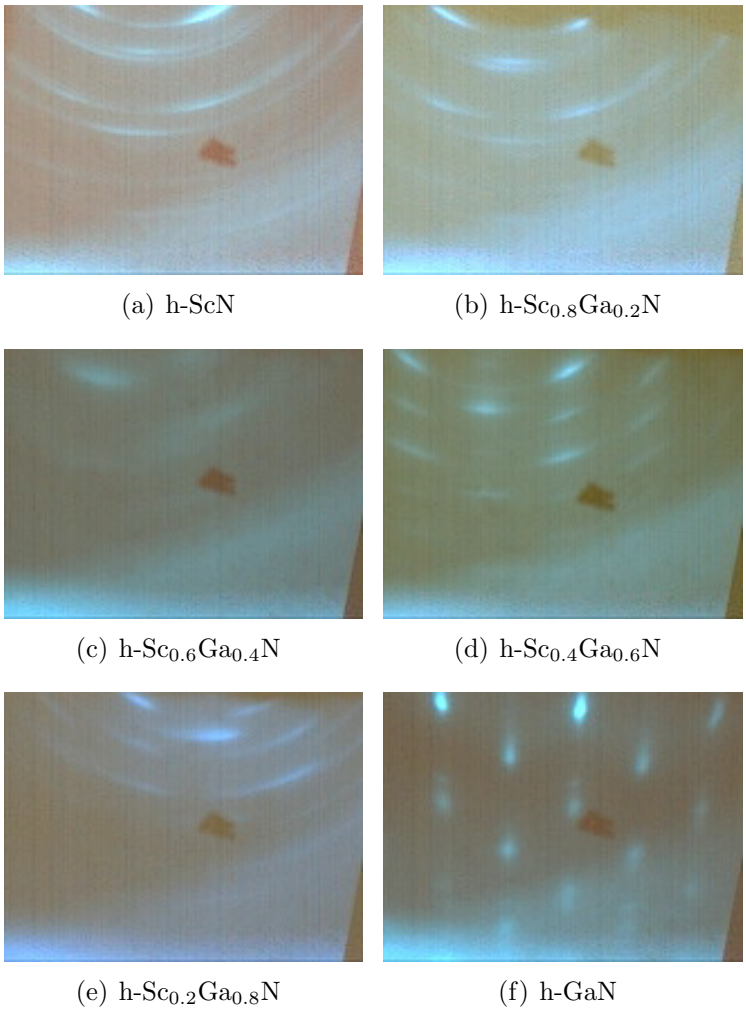

(a) h-ScN (b) h-$Sc_{0.8}Ga_{0.2}N$

(c) h-$Sc_{0.6}Ga_{0.4}N$ (d) h-$Sc_{0.4}Ga_{0.6}N$

(e) h-$Sc_{0.2}Ga_{0.8}N$ (f) h-GaN

Figure 4.22 – RHEED patterns after growth of h-ScGaN/GaAs(0 0 1) for various Sc compositions, taken using 12 keV primary beam energy.

(a) c-ScN

(b) c-$Sc_{0.8}Ga_{0.2}N$

(c) c-$Sc_{0.6}Ga_{0.4}N$

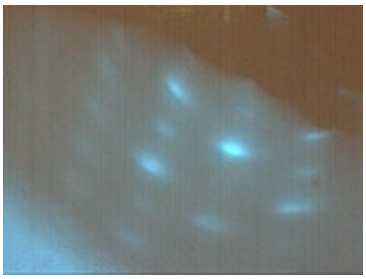

(d) c-$Sc_{0.4}Ga_{0.6}N$

(e) c-$Sc_{0.2}Ga_{0.8}N$

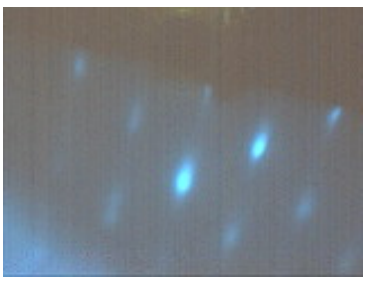

(f) c-GaN

Figure 4.23 – RHEED patterns after growth of c-ScGaN/c-GaN$(0\,0\,1)$/GaAs$(0\,0\,1)$ for various Sc compositions, taken using 12 keV primary beam energy.

and $Sc_{0.2}Ga_{0.8}N$ show an intermediate pattern in between the pure ScN and GaN patterns, while the GaN sample exhibits a single crystalline structure with a spotty pattern and streaky extensions.

From inspection of the $2\theta/\omega$ linescans of h-ScGaN, figure 4.24(a), samples with Sc compostions of 100, 80 and 60% have highly amorphous or microcrystalline structures. Low intensity peaks are observed corresponding to grains of ScN(1 1 1) and ScN(0 0 1). The [Sc] = 40% sample shows a very strong peak at $\sim 34.5°$, but it cannot be determined from a linescan whether this originates from ScN(1 1 1), h-GaN(0002), an alloy or a mixture of all three. Further analysis of scans such as pole plots around h-GaN 105 reflection will be required, in order to determine identity and volume of various fractions. The linescan of [Sc] = 20% shows diffraction peaks at $\sim 34.5°$ (which could be assigned as either ScN(111) or h-GaN(0002)) and $\sim 40.0°$ (which could be assigned as either ScN(002) or c-GaN(002)). This is an unexpected result which probably originates from a mislabeling of samples/scans. Further work will be required to investigate whether this is a real result or not. Since the results however, show that the material quality of Sc-rich ScGaN is poor, there is little motivation to do this. Before detailed work investigating the structure of ScGaN and locating the composition at which a cross-over between a predominantly rock-salt and wurtzite structure occurs is undertaken, high-quality growth of both h-GaN and ScN using the same method should be achieved.

In the cubic series, figure 4.24(b), $2\theta/\omega$ linescans of ScN and $Sc_{0.8}Ga_{0.2}N$ show two well defined peaks at $\sim 40°$ and $\sim 34.5°$, consistent with ScGaN(1 1 1) grown on c-GaN(0 0 1). It is considered unlikely that the c-GaN(002) peaks also contain contributions from the ScGaN, e.g. either due to polycrystallinity or phase separation. The GaN and $Sc_{0.2}Ga_{0.8}N$ samples show just one peak at $\sim 40.0°$, however in these cases it is believed that this includes contributions from the c-ScGaN(0 0 1), in addition to the c-GaN(0 0 1) buffer layer. As expected from the RHEED pattern, the linescan of the sample with 60% Sc indicates an amorphous film. There is no peak at 34.5° and the peak at $\sim 40.0°$ has a lower intensity than the corresponding peak in the Ga-rich ScGaN samples.

In neither the cubic nor the hexagonal series are there any peaks in addition to those that occur due to ScN(111), ScN(002) and the Al sample stage. If alloys are produced with a differing structure to either zinc blende or rock-salt, then the change in lattice parameter is not sufficient to be witnessed by XRD.

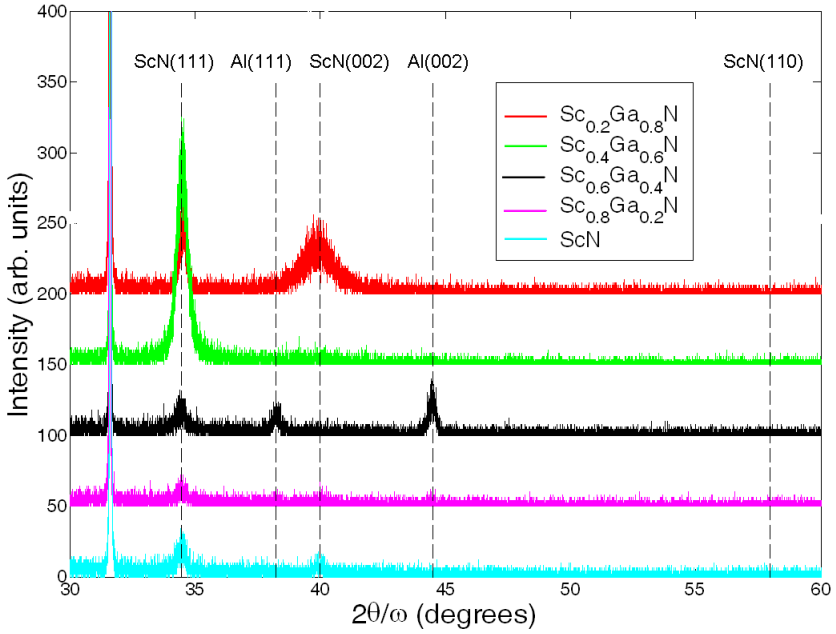

(a) hexagonal ScGaN

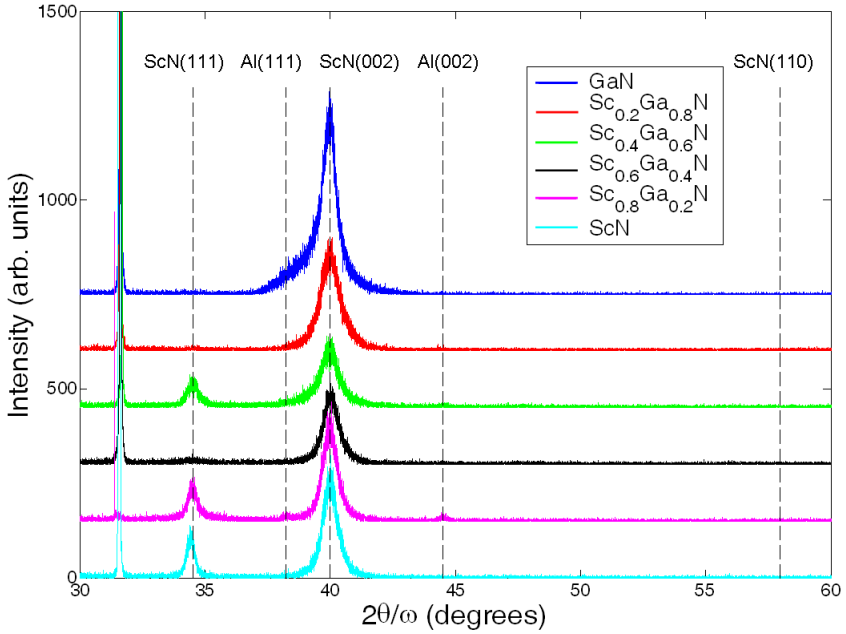

(b) cubic ScGaN

Figure 4.24 – $2\theta/\omega$ linescans of various compositions of ScGaN grown on (a) native GaAs substrate surface and (b) a 100 nm c-GaN(001) buffer layer. Graphs (top to bottom) plotted in order of increasing scandium content

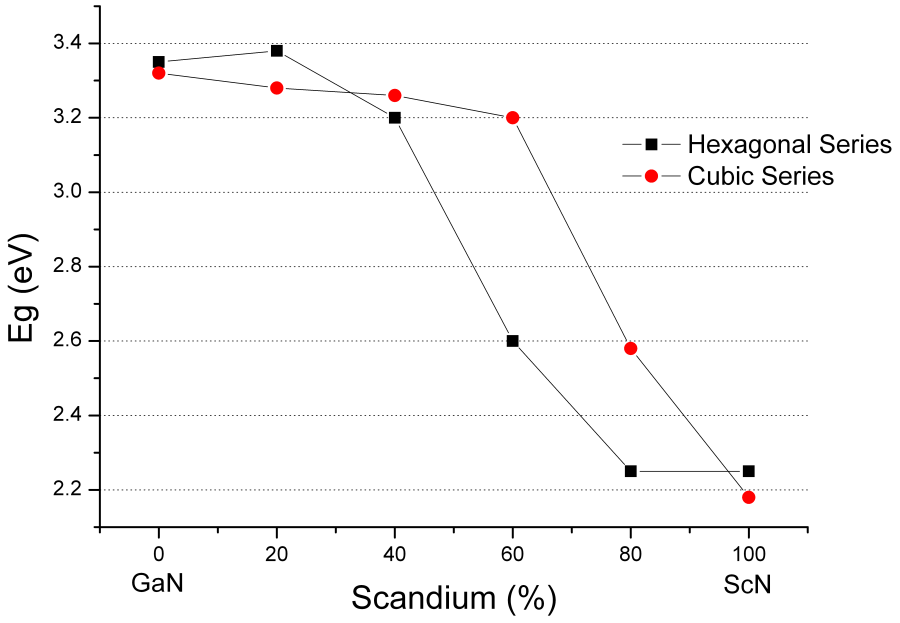

Figure 4.25 – Bandgap of nominally cubic and hexagonal ScGaN films as a function of composition. The bandgap was determined by the onset of absorption measured by ORS.

In all intermediate composition cases, XRD cannot confirm whether ScGaN films are single-crystalline or have undergone phase separation, due to the complication that peaks from both ScN and GaN can occur at the same $2\theta/\omega$ positions. The ScN(111) peaks could be a mixture of ScN(1 1 1) and h-GaN(0002), while the c-GaN peak could contain contributions from the ScGaN layer as well as the buffer layer. Additionally alloy phases (with either zinc blende or rock-salt structure) will also give diffraction peaks at the same 2θ positions. Even alloy phases with metastable structures could be present, if their lattice constants are similar to the stable polytypes. Initially, the aim was to make an assessment of the volume fraction of cubic and hexagonal material in ScGaN, by performing pole plots. The samples however, were not of sufficient quality. This also does not preclude the possibility that other similar phases are present in addition to perfect wurtzite and rock salt/zinc blende structures. XRD does, however, have its uses as a quick means of determining whether the materials have long-range order, i.e. they are not polycrystalline or amorphous. The use of other methods will be required in order to sufficiently analyse the structure of ScGaN films.

ORS studies have been used to determine the bandgap as function of composi-

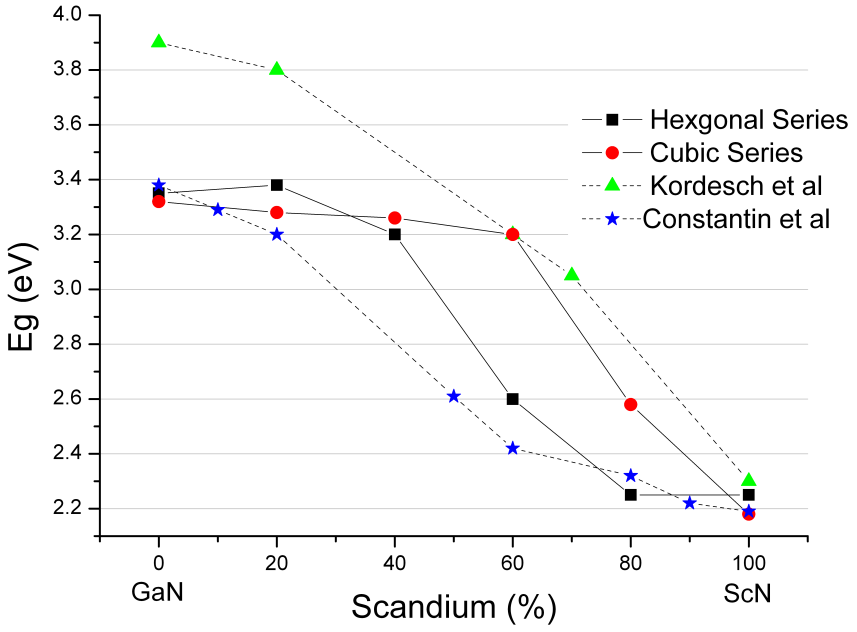

Figure 4.26 – Comparing the bandgap of ScGaN measured in this work and that reported in the literature.

tion for both series and results are shown in figure 4.25. In neither the cubic nor hexagonal case is there is a linear dependence on bandgap over the whole composition range. For Ga-rich compositions however, there does appear to be a linear dependance, albeit with a small slope that if extrapolated to ScN would yield a bandgap of 3.1 eV. At high Sc concentrations, a large decrease in bandgap to an intermediate value between ScN and GaN is witnessed. There is also some evidence of a linear dependence for the very Sc-rich regime (Sc$>$ 80%). The switching between high and low bandgaps could be a indication that the structure of the alloy changes from a predominantly rock-salt (ScN) to cubic or hexagonal (GaN). This three regime behaviour of bandgap with composition, is in agreement with results reported by Constantin et al. [78]. Note however, that the high number of free carriers in ScN, mean that measurements of the bandgap could be affected by the Burstein-Moss shift.

Since the bandgap does not appear to vary linearly with composition, efforts were undertaken to assess how the refractive index varies with composition. Ellipsometry measurements were performed, however without definite thicknesses, there were too many unknown parameters to produce self-consistent results.

4.8 ScMnN

It has been predicted that Mn-doped ScN will form a dilute magnetic semiconductor (DMS), with a Curie temperature (Tc) of 400K for 3% Mn [9]. Despite room temperature predictions for Tc in materials such as GaMnN and GaMnAs, the highest Tc currently reported is $\sim$ 185K [1] in GaMnAs. A typical problem in the growth of DMS's is the low solubility limit of the transition metal elements typically used for doping (Mn and Cr). This can lead to the precipitation of Mn and the formation of secondary phases, such as Mn_xN_y and MnAs. In order to avoid Mn precipitation, low growth temperatures are employed. These however, generally lead to a degradation of the host semiconductor crystal. A proposed contribution to the low solubility limit is the fact that the crystal structure of the likely precipitated phases differs from the host semiconductor [9, 91], e.g. MnAs exhibits two phases, one with a hexagonal and the other a orthorhombic structure, while the host, GaAs, has a zinc blende structure. MnN also has a orthorhombic structure. A characteristic of the dissimilar bonding configurations (non-isocrystallinity), is that the lattice parameter of alloys does not follow Vegards law, such as in the case of GaMnN [92].

Since ScN and MnN have closely related rock-salt structures and a lattice mismatch of 6%, mutual solubility should be enhanced and alloying be facilitated. In addition to predicting that Mn-doped ScN favours ferromagnetic coupling, calculations show that the unintentional n-type doping of the host material is also expected to be useful in spintronic applications [9].

4.8.1 Literature review

Smooth ScN(0 0 1) growth has been reported on Mg(0 0 1) substrates at 800 °C by RF-MBE [62]. Growth of MnN(0 0 1) has also been reported on MgO(0 0 1) substrates by RF-MBE [93] over a range of substrate temperatures from 250-450 °C. RHEED studies indicated that smooth surfaces could be obtained for growth performed at 450 °C.

Growth of ScMnN has been reported by Al-Brithen et al. in 2004 [91], however magnetic measurements were not performed, despite the motivation being to investigate the potential to form a DMS. Two sets of samples were grown: (A) ScN

doped with 19% Mn over a range of substrate temperatures from 330-612 °C and (B) ScN doped with different Mn concentrations ($10 - 26\%$) at a fixed growth temperature of 518 °C. All samples were grown on a ScN buffer layer deposited at 800 °C using MgO(0 0 1) substrates. For sample set A, all RHEED patterns had streaky behaviour, but also present were faint rings attributed to surface accumulation, presumably of Mn. The sample grown at 330 °C showed the most spotty character, while the sample grown at 518 °C had the most streaky pattern with a marked reduction in spot size (compared to other samples) and the faintest rings. This sample also showed the largest incorporation of Mn, as indicated by the largest shift in XRD peak position, relative to the ScN peak. The sample grown at 612 °C showed the lowest incorporation of Mn with a peak position very close to the ScN buffer layer. AFM images highlighted the presence of dots on the surface for all samples, except for the one grown at 612 °C. XRD analysis of sample set B, found a linear decrease in the out-of-plane lattice parameter with increasing Mn flux. Analysis of the spacings in the RHEED pattern also showed a linear decrease with increasing Mn concentration for the in-plane lattice parameter. These results indicate that both the a and c lattice parameters of ScMnN follow Vegards law. They also extrapolated well to expected MnN bulk lattice constant as reported by Yang et al. [93]. This suggests that Mn can be incorporated into ScN relatively easily, over a range of compositions, but for growth temperatures below 600 °C.

A magnetic study of ScMnN has been found in the thesis of Constantin [94]. 300 nm ScMnN films were grown on ScN(0 0 1)/MgO(0 0 1) at substrate temperature of $\sim$ 520 °C for 3 and 5% Mn. SQUID measurements showed that the samples containing 3% Mn exhibit ferromagnetic behaviour with a Curie temperature of $\sim$ 50K. No hysteresis however was observed in the samples doped with 5% Mn. No follow-up work has been reported by the group.

4.8.2 Growth details and results

A set of three samples were grown for 2 hrs at $\sim$ 700 °C for nominal Mn concentrations of 0, 3 and 6%. Films were grown on GaAs substrates and growth was initiated following a 1 min nitridation of the native GaAs surface at $\sim$ 650 °C. The substrate temperature was found to initially increase, following the opening of the Sc and Mn shutters, so manual temperature control was used to stabilise the growth temperature. Once growth was established, the manual control was

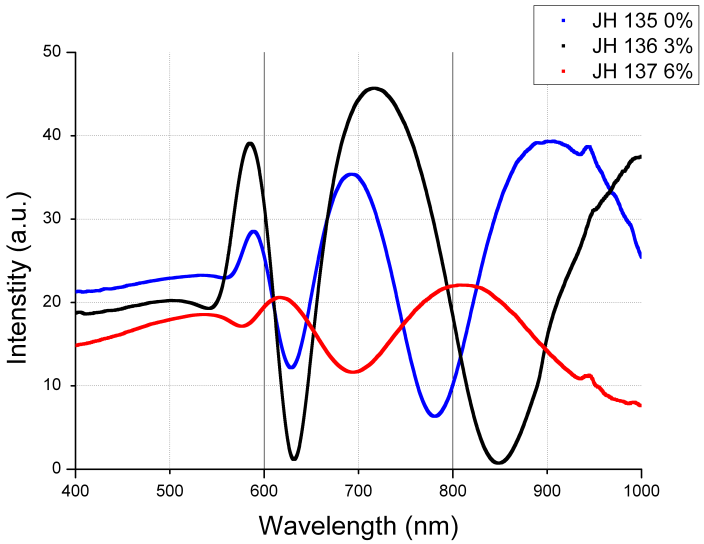

Figure 4.27 – ORS of ScMnN for nominal Mn concentrations of 0, 3 and 6%.

required to prevent the growth temperature drifting down. The RHEED pattern after all growths displayed bright diffuse arcs, indicating that all samples have a structure with a high degree of polycrystallinity.

ORS results displayed in figure 4.27 show good oscillations with a bandgap value for all samples of $\sim$ 2.25 eV. Assuming a growth rate of 250 nm/hr for all samples, optical refractive index is calculated to be 1.61 for ScN and 1.77 for the ScMnN samples.

Magnetic measurements performed by SQUID show typical paramagnetic behaviour for both Mn containing samples; as indicated by the absence of any magnetic moments at zero field and a characteristic 1/T dependence when field cooled, figure 4.28. Remanance data shown in figure 4.29, suggests that a fraction (approx 1/10th) of the moments are in superparamagnetic clusters, which can be frozen below a characteristic blocking temperature ($\sim$20K for JH136 and $\sim$40K for JH137).

In all samples, XRD data from $2\theta/\omega$ linescans show very low intensity nitride peaks, suggesting that the material is microcrystalline. All three samples show some polycrystalline structure: JH135 exhibits (1 1 1) and (0 0 1) grains, JH136 (0 0 1) and (1 1 0) grains while JH137 has (1 1 1) and (0 0 1) grains. Other peaks in the linescan of JH137 are attributed to the Al sample stage. The high intensity peaks in all scans originates from diffraction from the GaAs substrate. The

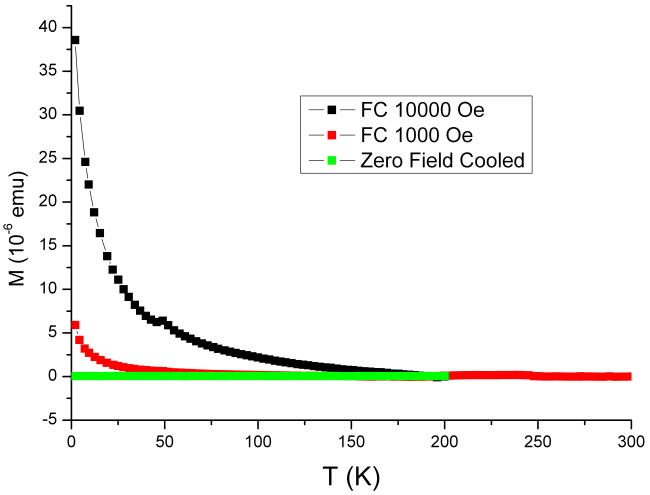

(a) 136 3% Mn

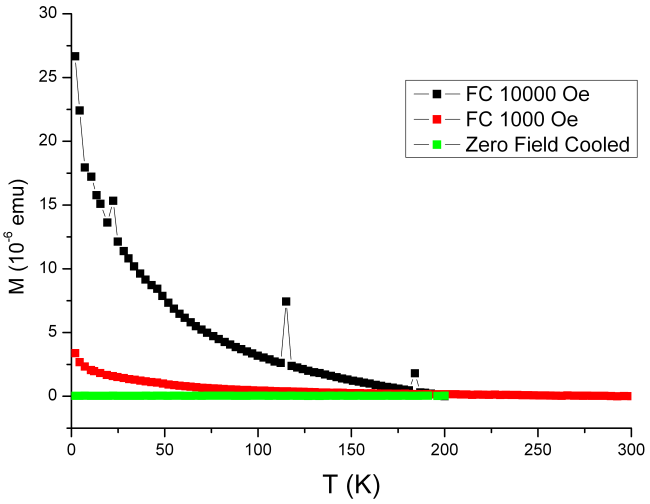

(b) 137 6% Mn

Figure 4.28 – Temperature dependence of magnetization under zero and external applied fields of 1000 and 10000Oe for nominal (a) $Sc_{0.97}Mn_{0.03}N$ and (b) $Sc_{0.94}Mn_{0.06}N$.

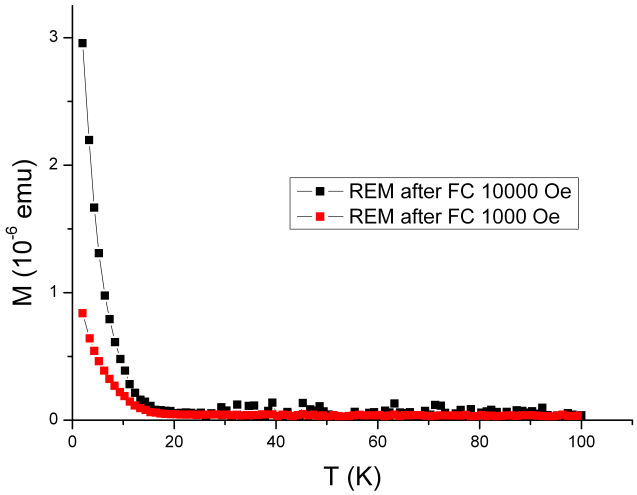

(a) REM 136 3% Mn

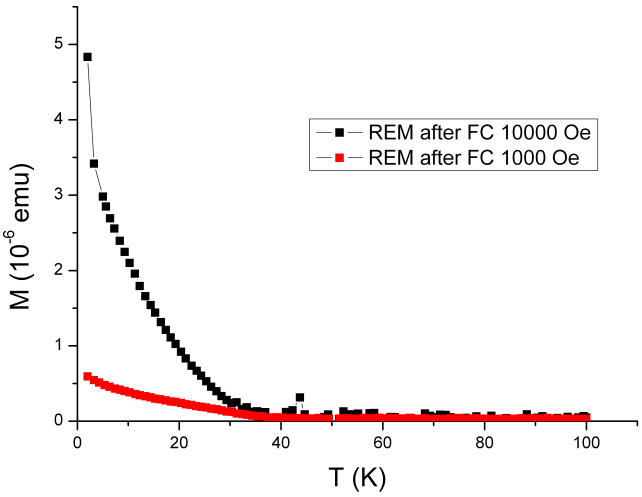

(b) SQUID 137 6% Mn

Figure 4.29 – Temperature dependence of remnant magnetization after external applied fields of 1000 and 10000Oe for nominal (a) $Sc_{0.97}Mn_{0.03}N$ and (b) $Sc_{0.94}Mn_{0.06}N$.

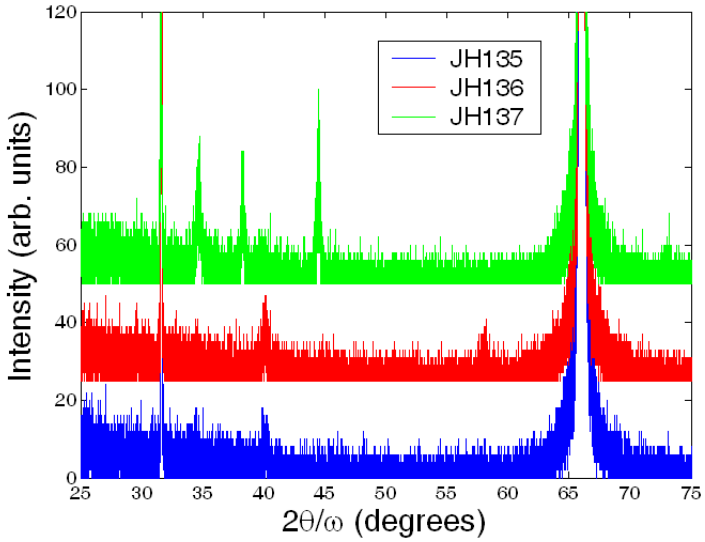

Figure 4.30 – $2\theta/\omega$ linescans of ScMnN with varying Mn composition.

poor material quality is not attributed to the incorporation of Mn, but rather that the host semiconductor material itself has poor structure. Since theoretical calculations are for semiconductor materials with long-range order, it is possible that ScMnN is ferromagnetic, but material quality is not of sufficient quality to produce this effect.

4.9 Potential for Further Work

The most pressing requirement in work involving Sc is to investigate how the Sc source behaves. The main problem encountered in carrying out this work was that the Sc source material was found to quickly evaporate, sometimes only providing enough material for 10 growths. It is possible that Sc adversely reacts with arsenic or oxygen. Before more detailed investigations are carried out, finding a solution which produces a stable Sc source is highly desirable.

Additionally before more growths are performed, further TEM analysis is desired in order to determine thicknesses and assess material quality of samples so far obtained. These results are expected to influence the direction of future work.

One of the most obvious areas for further work is to optimise the growth system of GaN/ScN/ScAs at all stages, as so far, very few growths have been performed.

This could be done by changing growth temperatures, flux ratios and initial nucleation conditions of the nitride layers (such as pre-nitridation or a Sc deposit of varying times). Investigations into the properties of ScN, e.g. n as a function of thickness, should really be carried out on the highest-quality material that can be obtained. Properties such as carrier concentrations and PL responses can be severely affected by material quality.

As so little information has been published regarding ScAs, a stand-alone investigation into this material should provide new information, such as confirming its nature (semi-conducting or semi-metallic). Although the RMS surface roughness and FWHM (from XRD) were disappointing, this is thought to be due to the growth chamber not being sufficiently clean. This is supported by comparisons between the FWHM from the ScAs, and even GaAs, peaks in the $2\theta/\omega$ linescans which show an improvement between JH170 (ScAs) and subsequent samples, JH171 and JH173. This suggests that RMS surface roughness and FWHM obtained are not indicative of typical ScAs material. After growth has been optimised, it would be worthwhile carrying out more RSM about the asymmetric GaAs 444 Bragg reflection. The samples grown so far, show that ScAs has almost fully relaxed, suggesting the presence of mismatch dislocations. Thinner samples and/or better growth conditions could lead to fully strained films, indicating increased material quality. This could potentially lead to better overgrowth of ScN. It would also be interesting, and relatively quick, to investigate the growth of GaAs on ScAs to see if GaAs can be grown with a rock-salt structure.

When performing further XRD analysis, it would also be useful to collect ω scans. This would lead to a better assessment of material quality of samples with respect to each other (e.g. mosacity) and make it easier to compare with results reported in the literature (these are often FWHM of rocking curves, cf. $2\theta/\omega$ linescans). Preliminary linescans were carried out in this work, as there was a more pressing requirement to identify phases and orientation of material present and to gain a quick estimate of material quality.

It is puzzling that ScN fails to grow with a (0 0 1) orientation on c-GaN(0 0 1). It could be interesting therefore, to investigate why this happen; possibly by carrying out DFT structure calculations.

Growth of h-ScGaN and ScMnN was carried out on GaAs, due to the issues regarding the Sc cell. By growing on GaAs native substrates, heating up the

arsenic source could be avoided. It was not however, known at the time, that this produces poor quality ScN material. If work is continued, re-growths should be carried out on different surfaces. Now that growth of ScN(0 0 1) has been achieved, c-ScGaN should be grown on ScAs, meaning that c-GaN and ScN have the same orientation. XRD cannot be used for structural analysis of ScGaN due to the fact that it cannot differentiate between c-GaN and ScN, in addition to difficulties in differentiating between c-GaN and h-GaN. Generally, this means that it is not possible to detect if phase separation has occurred. Therefore, if good growth of ScGaN is achieved other methods will be required in order to analyse the structure of the alloys as a function of composition. Methods could include energy dispersive X-ray spectroscopy, Rutherford backscattering, selected area diffraction or TEM. Analysis of the bandgap as a function of composition, shows that more more data points are required in order to better assess the relationship, eg. growing samples in nominal 10% intervals (vs. 20%). ScMnN growth on ScN(001)/ScAs(001), should be carried out for a range of growth temperatures from $500 - 700\,^{\circ}\mathrm{C}$, as literature suggests that Mn is difficult to incorporate for substrate temperatures higher than $600\,^{\circ}\mathrm{C}$ [91].

4.10 Conclusions

Epitaxial growth of ScN on c-GaN(0 0 1), GaAs(0 0 1) and ScAs(0 0 1) has been reported for the first time. Despite the lattice match, ScN grows in a 3D growth mode with a twinned (111) orientation on c-GaN(100), for a variety of Sc:N flux ratios and growth temperatures (up to $\sim 700\,^{\circ}\mathrm{C}$). This appears to be the first incidence in the literature, of the orientation of ScN not being pre-determined by the material it was deposited on; the reasons for which remain unclear. The volume ratio of the two twin components has been calculated to be 1:1. ScN(1 1 1) was found to have n-type carrier concentrations in the region of low $10^{19}\mathrm{cm}^{-3}$ and resistance readings of a few kΩ's. As a function of thickness, surface roughness was found to increase from 2 nm (for ~ 250 nm) - 10 nm (for ~ 750nm).

TEM analysis shows that for ScN interlayers with thicknesses greater than 5 nm, stacking faults running on 111 formed in c-GaN(100) terminate at the c-GaN/ScN interface. GaN grown atop ScN(1 1 1) however, crystallises in the wurtzite polymorph. ScN thicknesses of $\sim 1 - 2$ nm result in overgrowth of GaN in the cubic

phase, however no significant reduction in stacking fault density or surface roughness is observed. This leads to the conclusion that the use of ScN interlayers is not a suitable method for reducing the defect density of c-GaN(0 0 1). The critical thickness for GaN growing cubic or wurtzite on ScN(1 1 1) was found to be between a nominal Sc thickness of 3.3 and 5 nm.

Growth of ScN on GaAs(1 0 0) mostly results in ScN with a twinned (1 1 1) orientation, though a (1 1 0) orientation can be obtained under certain conditions. The ScN(1 1 1) films were found to be of poor quality with either an amorphous or microcrystalline structure.

ScN grown on ScAs(0 0 1) was found to result in a (1 0 0) orientation. RHEED indicated growth took place in a 2D growth mode with surface showing a 1x1 reconstruction. AFM analysis yielded a surface roughness of 1.5 nm representing a 25% reduction compared to ScN(1 1 1). The FWHM value of the ScN peak in a $2\theta/\omega$ linescan, comparing the 1 hr growth of ScN(1 1 1) and ScN(0 0 1), also showed a reduction from 0.35° to 0.31°. No investigation into Sc:N flux ratio, growth temperature or nucleation conditions took place, so it is possible that further improvements in material quality can be obtained. ScAs growth was also found to result in smooth surfaces with a 1x1 reconstruction. Parameters measured so far, such as the carrier concentration and lattice parameter agree with values published in the literature. Evidence has been presented which suggests that ScAs is a semi-metal.

GaN grown on ScN(0 0 1) surfaces was found to result in c-GaN(0 0 1) films, despite the reverse not being true. Although cubic GaN material was produced when grown on a rock-salt material, the GaN surface was rough (RMS surface roughness= 4.5 nm cf. 3.3 nm for c-GaN/GaAs). This is attributed to the growth process not being optimised. Further investigation will be required to ascertain whether growing on a ScN(0 0 1) buffer layer can lead to an improvement in material quality for c-GaN(0 0 1).

Growth of nominal hexagonal and cubic ScGaN on GaAs has taken place across the whole compositional range in nominal 20% intervals. RHEED analysis showed rock-salt like structures for Sc compositions greater than 70%, amorphous structures for $Sc_{0.6}Ga_{0.4}N$, intermediate structure for $Sc_{0.2}Ga_{0.8}N$ and $Sc_{0.4}Ga_{0.6}N$ and cubic or wurtzite for GaN. XRD analysis however, showed material quality of Sc-rich samples in the hexagonal series to be microcrystalline. Although relatively

good-quality c-ScGaN was obtained, it was not possible to confirm whether the material had a cubic (001) orientation, as the peak position that this would lead to also contains contributions from the c-GaN(0 0 1) buffer layer. The bandgap of all samples was measured using ORS, whereby it was found that there was not a linear dependence with composition. For Ga-rich compositions, the bandgap was found to vary linearly. There is some evidence for confirmation of 3 regimes of growth for (I) high Ga, (II) intermediate Ga and (III) low Ga compositions, as reported by Constantin [78].

Initial investigations into the growth of ScMnN found resulting films were paramagnetic rather than ferromagnetic, as predicted by Herwadkar and Lambrecht [9]. This is possibly due to the poor-material quality of the host semiconductor, which itself is due to growth nucleating directly on GaAs.

Chapter 5

In-rich InGaN

5.1 Background

5.1.1 Motivation - solar cells

The idea of getting 'free' electricity from the sun, continues to tantalise people's imagination, driving research towards the fabrication of ever more efficient solar cells with lower production costs. The conventional single-gap solar cell however, is already achieving efficiencies near the theoretical maximum [95], set by the Shockley-Queisser limit [96], of $\sim 30\%$ (or $\sim 40\%$, depending on concentration of light). In order to obtain higher efficiencies of solar cells therefore, different approaches are required.

The two most significant losses in a single bandgap solar cell arise from (i) its inability to absorb photons with less energy than the bandgap and (ii) thermalisation of photon energies exceeding the bandgap. Attempts at utilising this unused energy typically fall into one of three categories:

(a) increasing the number of absorbing levels e.g. tandem (multijunction) cells and intermediate band solar cells.

(b) multiple carrier pair generation per high energy photon *or* single carrier pair generation with multiple low energy photons. e.g. relying on impact ionisation events to form multiple carriers close to bandgap energy from

high energy photons or modulation of the incoming spectrum through up/down conversion.

(c) capturing carriers before thermalisation e.g. hot carrier cells.

For a more detailed review of these modern approaches to solar cell fabrication the reader is referred to reference [97].

Of these approaches, implementation of strategy (a) is the most common. In particular, tandem cells are the most developed, being the first type of cell to achieve efficiencies greater than 40%. Tandem, or multijunction, cells consist of several p-n junctions in a single structure. Different semiconductor materials of increasing bandgap are stacked on top of each other, such that the widest bandgap intercepts the sunlight first. Each type of semiconductor will absorb light efficiently at a certain part of the spectrum. By selecting the compositions of each layer carefully, nearly all of the solar spectrum can be used to generate electricity. Usually the different junctions are connected in series, placing the constraint that the same current must flow through each cell. This makes them less flexible than their parallel connected counterparts and also very sensitive to spectral variations. Nonetheless, being easier and cheaper to construct makes it the design of choice. Other problems arise from the requirement that different layers are lattice matched to each other, in order to avoid dislocations.

The intermediate band solar cell (IBSC) was proposed as a realistic approach to high efficiency solar cells by Luque and Martí [15] in 1997. The increased theoretical efficiency of the cell relies on the introduction of one or more energy levels within the bandgap such that, photons are absorbed in parallel with the normal operation of the single bandgap cell. It consists of an intermediate band (IB) material, sandwiched between two conventional semiconductors of p and n type, figure 5.1. The concept follows on from the impurity photovoltaic cell, but with the need for an intermediate 'band', rather than a collection of discrete energy levels introduced by impurities. In both devices, two below bandgap photons can be absorbed to create one electron-hole pair of bandgap energy. The advantage of the IB is that photons do not have to be absorbed by the same electron. This leads to much longer lifetimes in the IB due to the overlap of wavefunctions supressing non-radiative recombination, allowing more time for absorption of a second photon. To maximise this advantage, the IB should be half filled with electrons, such that absorption of an electron from the Valance band, or emission of an electron

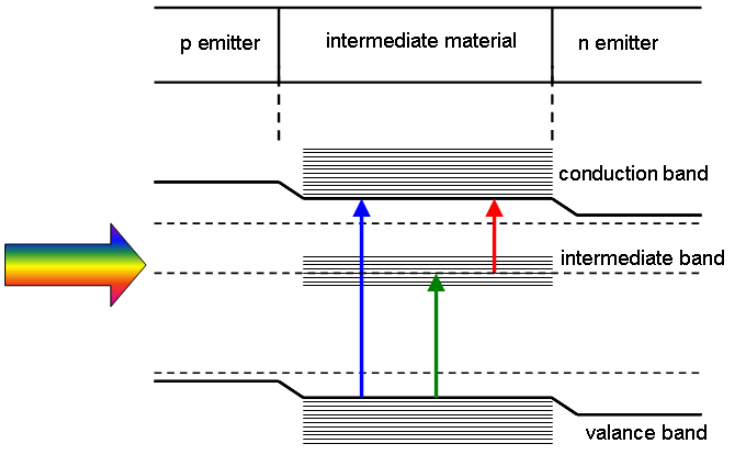

Figure 5.1 – Simplified schematic of a solar cell with an intermediate band.

to the conduction band are equally likely. A limiting efficiency, as high as 63.2%, has been predicted for IBSCs, compared to 55.4% for a tandem of two cells and 40.7% for single gap cells.

Several material systems have been identified as possible candidates for IBSCs. These include: quantum dots [98], diluted II-VI oxide semiconductors [99], GaNAsP [100] and Ti inserted into GaAs, GaP and $CuGaS_2$ [101] [102]. Experimental attempts have largely focused on the GaInAs/GaAs QD superlattice system. Although devices based on this system have demonstrated indicators of true IBSC operation proving some of the basics of IBSC theory (references within [103]), they have not yet shown any efficiency advantage.

Recently, $In_xGa_{1-x}N$ doped with Mn has also been suggested as a possible intermediate bandgap system [14]. InGaN is desirable as the host semiconductor, due to the potential ability to tailor its bandgap over the whole visible spectrum. The inclusion of Mn is predicted to introduce deep centers within the InGaN bandgap. Additionally, Mn is attractive as it is has been reported that substitutional Mn can be incorporated at high concentrations in GaN [104], InAs [105], GaAs [1] and $In_{0.845}Ga_{0.154}N$ [106], suggesting that the same can be achieved in InGaN. The minimum amount of Mn calculated to create a band is $6 \times 10^{19}\,cm^{-3}$, representing a $\sim 0.25\%$ concentration in InN and GaN. The maximum photovoltaic conversion, for concentrated energy, of a cell operating at a temperature of 300K has been calculated to be $\sim$ 53.4% when the gallium content is $\sim$ 0.22, corresponding to a bandgap of 1.11 eV. This breaks down into 40.7% from transitions

from the valance band to the conduction band (maximum single bandgap solar cell efficiency), 4.08% from transitions from the intermediate band to the conduction band and 8.55% from transitions from the valance band to the intermediate band.

The aims of this work were to:

(i) demonstrate alloy control of InGaN

(ii) demonstrate insertion of Mn into $In_{0.8}Ga_{0.2}N$

(iii) investigate whether there is phase boundary for Mn-doped $In_{0.8}Ga_{0.2}N$; i.e. produce a plot highlighting maximum Mn concentration that can be incorporated into $In_{0.8}Ga_{0.2}N$ as a function of growth temperature

5.1.2 InN and InGaN

It has now been accepted that InN has a bandgap of ∼0.7 eV, as opposed to the previously assumed value of 1.9 eV. Alloying with GaN (bandgap 3.4 eV) therefore, produces a material system with the potential to span the whole optical wavelength range. This makes it particularly attractive for solar cells and optoelectronic applications. It is also being considered for use in optical communications, targeting telecommunications with emitters of $\lambda = 1.5$ µm, as a way of achieving arsenic-free technology [11].

Of all the III-nitrides, InN has the smallest electron mass and the highest electron drift velocity, leading to expected applications in areas requiring good transport properties [107]. GaN is most famous for its excellent electrical properties, particulary its high efficiency luminescence. This suggests the potential for InGaN to have both excellent transport and optical properties. In keeping with other nitrides, InN has a low chemical reactivity and is resistant to damage by high-energy radiation [108], rendering InN and related alloys suitable for space applications.

InN is known however, to have a very high concentration of background carriers, N, and exhibit an electron accumulation layer at the surface. Initial reports placed N in the region of $2 \times 10^{20} - 8 \times 10^{21}$ cm^{-3}. Generally good-quality growths (as indicated by RHEED studies) now produce N values around mid 10^{18} - low 10^{19} cm^{-3} [107], with best mobility values reported for very thick InN

films; a sample with $N = 3.5 \times 10^{17}\,\mathrm{cm}^{-3}$ currently has the best mobility value of $2200\mathrm{cm}^2/\mathrm{Vs}$ [109].

An electron accumulation layer has been found to be present in both n and p-type InN. As Hall measurements are not able to differentiate between the n-type electron accumulation layer and bulk p-type material, many researchers speculated that p-doped InN material could not be achieved. With capacitance-voltage measurements however, bulk p-type conductivity can be detected as in the case of Mg-doped InN [10]. Electron concentrations in the accumulation layer of clean InN have been simulated to be $\sim 3 \times 10^{20}\,\mathrm{cm}^{-3}$, with a thickness of less than 1 nm [110] for a sample with a bulk N value of $3.3 \times 10^{19}\,\mathrm{cm}^{-3}$. In contrast, n and p-type GaN displays electron and hole depletion regions at the surface respectively. The electron accumulation layer in $\mathrm{In_xGa_{1-x}N}$ has been calculated to a first approximation, to start at $x = 0.43$ [111], with the surface charge density decreasing with increasing gallium content. A few groups [112,113] have measured N in InGaN, in the In rich regime (approx $x = 0 - 0.25$), giving values of the order of low 10^{19} cm^{-3}, which were similar to the authors measurements of their InN. Since these measurements will also be sensitive to the electron accumulation layer, they are likely to represent a slight over-estimate. The presence of an electron accumulation layer in In-rich InGaN will naturally, have an impact on what type of devices can be manufactured.

The main difficulty in achieving high-quality InN aries from the relatively low growth temperatures required which is reported to be between 500 and 600 °C cf. 680-850 °C for GaN. This originates from the high equilibrium vapor pressure of $\mathrm{N_2}$ over InN which leads to a low decomposition temperature for InN. The need for low growth temperatures makes MBE a more suitable growth method than metal-organic vapour phase epitaxy (MOVPE). MOVPE generally requires high temperatures for the nitrogen precursors, whereas in MBE, nitrogen can be supplied by a plasma source whose power can be set without consideration of the growth temperature.

An additional problem is that good-quality InN has been found to exist within a very narrow range of growth conditions. The growth temperature should be set as high as possible, with V/III ratio as close as possible to stoichiometry (approached from N-rich side). If either growth parameter is not controlled carefully enough, then In droplets may form, which do not evaporate from the surface

and reduce film quality. Furthermore, growth under N-rich conditions leads to poor-quality structural material, which exhibits columnar growth. A study into RF-MBE growth of InN by Nanishi et al. [12] highlights the extreme sensitivity of InN to growth conditions. They found that a change in RF power of 20W was enough to cause a transition from a clean surface to one with a high density of In droplets. Equally, a difference of 20-30 °C was enough to cause a change in the predominant texture of InN. The authors also suggested that the smoothness of the surface that InN was grown on was a crucial factor in obtaining high-quality InN.

The difference in growth temperatures of GaN and InN, coupled with the 10% lattice mismatch, leading to a expected large miscibility gap, means that the growth of single crystalline In-rich and InGaN with large mole fractions of both In and Ga is expected to be even more challenging. There have been many reports whereby attempted growth of InGaN has led to phase separation and/or low structural quality [114–116]. Reports of single-phase InGaN however, for a wide range of InGaN compositions, have been published and are becoming increasingly common [12, 117, 118].

As in the case of InN, low growth temperatures are required ($450 - 550\,^{\circ}\mathrm{C}$), not only to avoid InN decomposition, but in order to prevent phase separation. This however, comes at the expense of crystal quality [13]. Growth rates and growth pressure have also been found to be factors in obtaining good-quality InGaN [119]. Higher growth temperatures can be used, but this has to be compensated by a higher nitrogen flux [13], which can lead to a degradation of the surface e.g. due to ion damage.

Unlike InN, where growth takes place very close to stoichiometry, growth of InGaN occurs under deliberately nitrogen-rich conditions. Thermal decomposition of InN leads to In droplets, which 'trap' impinging In atoms. This reduces the amount of In available for incorporation, leading to fluctuations in composition throughout the film. The presence and composition of In droplets on the surface can be assessed by SEM and EDX. The literature suggests that compositional control of InGaN grown by MBE (found to be simply a function of Ga:In flux ratio) is relatively easy, with good agreement with nominal and measured compositions [12, 120].

Most reports of the growth of InN and InGaN have been carried out on GaN buffer

layers grown on sapphire substrates. There have however, been some instances of growth taking place on InN or GaN buffer layers grown at low temperatures [12]. InN has been grown on GaAs substrates. Guo et al. [121] reported that the pre-treatment of the substrate with a exposure to nitrogen plasma was essential in obtaining epitaxial growth. They also found that the crystal quality was significantly affected by the exposure time. A review of InN grown on GaAs substrates is presented in reference [122].

The lattice parameter of InGaN is often assumed to vary according to Vegards law. HR-XRD $2\theta/\omega$ linescans are almost exclusively used for determination of lattice parameters, however the assumption of Vegards law is only valid for relaxed films. For thin InGaN films grown on GaN, where strain is expected to exist, this leads to a systematic over-estimation of the In content [112, 119].

The composition dependence of the $In_xGa_{1-x}N$ bandgap, over the entire composition range, has been experimentally determined to satisfy equation 5.1; which has the form of a standard bowing equation with a small bowing parameter of 1.43 eV [123].

$$E_g(x) = 3.24(1-x) + 0.7x - 1.43x(1-x) \tag{5.1}$$

PL measured at 77K by Nanishi et al. [12] and 10K by Moret et al. [113] has been observed in In-rich InGaN. Moret et al. found that the PL intensity was sensitive to both N and composition and also witnessed a rapid collapse in signal with increasing temperature. Modelling was performed to demonstrate that chemical alloy fluctuations are not expected to significantly impact the lineshape of PL, but rather that the carrier concentration is the dominant factor. The PL signal was found to rapidly decrease with increasing gallium concentration, which was attributed to the onset of recombination via non-radiative recombination centers. XRD results however, show FWHMs that do not drastically change with composition, meaning that the PL killing centers are not visible in XRD. Relaxation was found to occur for a InGaN thickness of ~ 100 nm, as witnessed by reduction in the measured c parameter. Nanishi et al. measured PL at 77K for all their samples. For InN, they also reported a typical XRD ω FWHM of 300 arcsec and N of $3 \times 10^{19}\,\mathrm{cm}^{-3}$ for a thickness of ~ 250 nm and a root mean squared (RMS) surface roughness between 1.5 and 3.6 nm. By growing a very thick sample (~ 1.5

µm) they obtained a best value for N of $4.8 \times 10^{18}\,\mathrm{cm}^{-3}$ was obtained, with a associated ω FWHM of 236.7 arcsec and a $2\theta/\omega$ FWHM of only 28.9 arcsec. XRD results of InGaN showed poor-quality material for samples with large amounts of both In and Ga ($x = 0.37 - 0.68$), which was attributed to the low growth temperature.

The solubility of doping elements in a semiconductor is related to the growth temperature and the melting point of the host material. In general, the solubility of a dopant is expected to increase with decreasing temperature [124, 125], with very little material being incorporated into the host matrix, at temperatures close to its melting point [125].

Mn-doped GaAs is known to require particularly low growth temperatures ($\sim$ 200 °C for GaMnAs vs. $\sim$ 580 °C for GaAs) [1] in order to avoid segregation and precipitation of MnAs secondary phases. However, there is the additional factor that Mn segregation is driven by the need for self-compensation; substitutional Mn acts a acceptor in GaAs introducing a hole concentration. Doping GaN with Mn meanwhile, can be achieved at growth temperatures of 700 °C [126,127], compared to growth temperatures in undoped GaN up to $\sim$ 1000 °C. As the decomposition temperature of InN is not well known, it cannot be determined *a priori* which growth temperatures will be required to incorporate Mn into InGaN, though it is expected to be between 200 and 700 °C, most likely at around 500 °C. It is predicted however, that the amount of Mn that can be incorporated, will be a function of growth temperature.

When selecting a growth temperature for InN or InGaN, caution must be taken. Most measurements of temperature reported in the literature use pyrometry. This method can give widely varied results from machine to machine and is dependent on the state of the surface. In addition, the emissivity of the alloy series will be unknown, meaning that most temperatures given in the literature are, at best, a relative measure. As the highest growth temperature which can achieve good-quality InGaN material is a function of III:V flux ratio, obtaining good-quality InGaN in this work will require a methodical exploration of growth parameters.

5.2 Experimental Procedure

Samples were grown in a custom built MBE machine with an ultimate base pressure of 1×10^{-9} mbar. Activated nitrogen was supplied using a CARS25 RF source, while conventional elemental sources were used for In, Ga and Mn. The nitrogen flux was kept constant at a growth chamber pressure of 3.5×10^{-5} mbar, using a N_2 flow of 1.11 sccm and an applied RF power of 450W. Films were grown on either semi-insulating GaAs(1 0 0) or GaAs(1 1 1) substrates.

Prior to growth the native oxide layer was thermally removed at 650 °C. The heater power was then reduced to the required setting and sample temperature allowed to stabilise. The surface was nitrided for 1 min and growth commenced by opening the In, Mn and/or Ga shutters. Note that there was no arsenic present during any stage of the growths. For samples grown to measure the rise in film temperature during growth, the heater remained supplied with constant power without any feedback control. For samples grown at a controlled temperature, a near-constant temperature before and during growth was maintained by manually altering the heater power.

As discussed previously (section 1.2 on page 8), the UHV environment in MBE can make measurement of the sample temperature difficult. To avoid this problem, growth on this project has been undertaken on GaAs substrates. This allows utilisation of a kSA BandiT system, in order to study changes in temperature during growth. To recap, the BandiT measures the temperature dependent bandgap of the substrate in order to provide an accurate method of temperature determination. It is assumed that the substrate and growing layer (epilayer/film) are at the same temperature. The advantages of this method over more conventional temperature measurements, is its non-dependence on composition and emissivity of the growing film and so therefore, it is not subject to apparent changes in temperature. Abrupt apparent changes are commonly encountered when measuring the temperature by pyrometry at the start of growth of GaN on GaAs.

Samples were characterised by XRD, which can be used to evaluate the presence of secondary phases, degree of polycrystallinity and, in the case of alloys, whether there is phase separation. Selected samples were also subjected to PL (performed by Glasgow University), SQUID and AFM measurements.

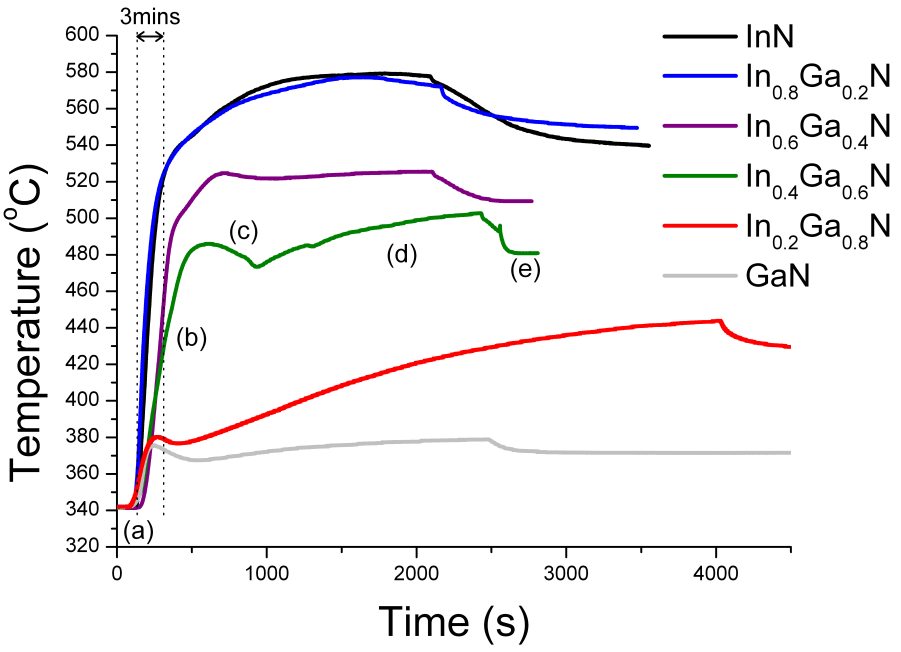

Figure 5.2 – Graph showing the band-edge measured temperature evolution during growths of $In_xGa_{1-x}N$, as a function of In composition. Graphs have been offset in temperature ($\pm 5\,^{\circ}C$) and time.

5.3 Temperature Control

During the first few calibration growths of InN, it became apparent that the growth of InN and In-rich InGaN in the mini-MBE machine results in rapid rises in substrate temperature; over 100 °C in a few minutes. In order to investigate this phenomenon in more detail, InGaN samples were grown across the whole compositional range in nominal 20% steps. A starting substrate temperature of 350 °C was chosen, to help avoid the sample temperatures reaching 600 °C; approximately where decomposition of InN is expected. All growths were initiated with a supplied heater power of $44 \pm 2\%$. This resulted in a stabilised sample temperature of $\sim 340\,^{\circ}C$, as determined by the BandiT. Samples produced using this method were taken as reference samples for InGaN grown without temperature control.

Sample	Composition	Initial rise in Temperature (b)	Change on closing shutters (e)	Net change
JH 124	InN	238 °C	38 °C	200 °C
JH 118	$In_{0.8}Ga_{0.2}N$	236 °C	27 °C	199 °C
JH 122	$In_{0.6}Ga_{0.4}N$	182 °C	17 °C	165 °C
JH 120	$In_{0.4}Ga_{0.6}N$	144 °C	22 °C	122 °C
JH 123	$In_{0.2}Ga_{0.8}N$	38 °C	17 °C	21 °C
JH 121	GaN	33 °C	7 °C	16 °C

Table 5.1 – Growth summary of temperature effects during uncontrolled growth of $In_xGa_{1-x}N$

5.3.1 Experimental results

The temperature dependence on growth time for several compositions of $In_xGa_{1-x}N$ is plotted in figure 5.2. The graph shows the temperature for each sample prior to growth (a), during growth (b)-(d) and when the shutters were closed, but all cells left running (e). During growth, all curves show a rapid initial rise in temperature (b) followed by a levelling off (c). Some curves, namely $In_{0.4}Ga_{0.6}N$ and $In_{0.2}Ga_{0.8}N$, show further features (d) which have been attributed to surface roughening effects. In no case does the final temperature (e) return to the initial temperature of the substrate (a), indicating all films show an increase in intrinsic absorption, due to the presence of a InGaN layer. The quantitative changes in temperature associated with the initial rise upon commencing growth (b) and decrease when the shutters were closed (e) can be found in table 5.1. The surfaces of JH 124 and JH 118 (In$\geq$ 0.8) were both visibly rough and showed evidence for the formation of In droplets, as well as sharing a similar maximum temperature. This would suggest that the decomposition temperature of InN is $\sim 580\,^{\circ}C$. It is not unreasonable to expect that if the starting temperature was lower, we would see a larger change in temperature (b) and possibly more of a distinction between the value recorded for $x = 0.8$ and $x = 1.0$.

If the rise in temperature was due to shutter transients alone, then we would expect the shutter closed temperature at the end of growth (e) to equal the shutter closed temperature before the start of growth (a); providing there are no changes in emissivity. This is observed in the growth of low-temperature GaAs, see figure 5.3. If there is sufficient surface roughening to cause a change in emissivity, this would generally lead to a lower than expected temperature, not higher as is observed.

It is notable from figure 5.2 and table 5.1 that the initial temperature rise (b)

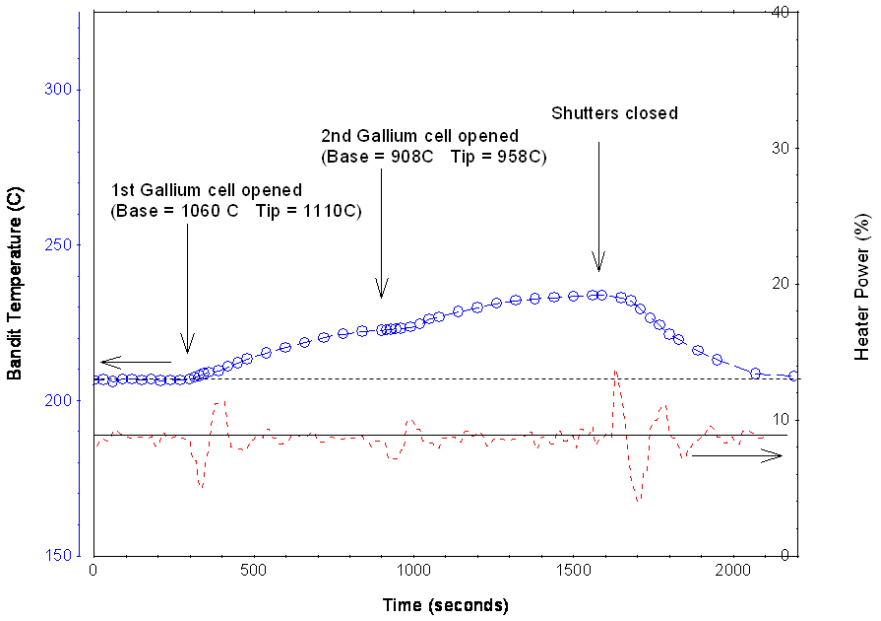

Figure 5.3 – Temperature evolution during growth of GaAs (performed by R. Campion on the Gen III) showing that the substrate temperature when shutter are closed at the end of growth, returns to the initial starting value.

increases with increasing In composition. For GaN and $In_{0.2}Ga_{0.8}N$, the rise of $30-40\,^{\circ}C$ is comparable (though slightly larger) to the magnitude expected from shutter transients alone. As the In composition goes beyond $x = 0.3$, there is a marked increase in the initial rise in temperature to more than $100\,^{\circ}C$. When the In composition exceeds $x = 0.7$, this initial rise in temperature reaches more than $200\,^{\circ}C$.

Band-edge measurement techniques have previously found changes in temperature during growth. One cause, of generally small changes, has been attributed to shutter transients [128], while more significant temperature increases have been observed and been associated with (i) growth of materials with narrower bandgaps than the substrate [129] and (ii) introduction of free carriers by doping (GaMnAs grown at low temperature [130]). Increases in temperature upon commencing growth can adversely affect film quality and in alloys, cause changes to composition, e.g. GaMnAs. Due to the relatively low decomposition temperature of InN, large changes in temperature are therefore, expected to be a problem for obtaining high-quality InGaN samples and impact the incorporation of Mn.

5.3.2 Modelling temperature rises

One might expect the large temperature rise observed in our growth of InN to be primarily due to growing a material with a narrower bandgap than the material on which it is deposited; E_g(InN) = 0.7 eV cf. E_g(GaAs) = 2.4 eV. However, previous band edge studies of even narrower bandgap materials grown on GaAs (co-incidentally with the same starting temperature), show smaller rises in temperature than those reported here. For example, growth of InAs (E_g = 0.35 eV) resulted in a temperature rise of $\sim 180\,^{\circ}$C [129]. This suggests that other mechanisms need to be considered to explain the observed rises in temperature. This is further supported by the fact that the bandgap of $In_xGa_{1-x}N$, is not expected to be narrower than GaAs until $x \sim 0.6$ (using equation 5.1). The sample with $x \sim 0.4$ however, already exhibits a large temperature rise of over $140\,^{\circ}$C.

As mentioned previously, InN is known to exhibit a high degree of unintentional doping with bulk carrier concentrations typically in the region of mid 10^{18} - mid 10^{19} cm^{-3}. It has also been shown that InN has a surface electron accumulation layer with a carrier density $\sim 10^{20}$ cm^{-3}. The calculated transition from depletion to surface electron accumulation of $x = 0.43$ for $In_xGa_{1-x}N$ co-incides with the observed onset of large temperature rises at $x = 0.4$

Absorption from free carriers in InN (and In-rich InGaN) is therefore also a viable mechanism for the large temperature variations. This was the process proposed as responsible for the temperature rise of $\sim 30\,^{\circ}$C observed during the growth of GaMnAs on GaAs [130]. In this instance, the Mn concentration is low enough that a significant difference in the bandgap of the epilayer and substrate is not expected. The rise is larger than that due to shutter transients. The authors presented a model considering effects to absorption of free carriers as well as phonons whereby doping with Mn, leading to strong free-carrier absorption in the near IR range, was attributed as the reason for the temperature rise.

A model will be described here to explain the origin of the observed temperature rises in InN and GaN, by accounting for absorption due to the bandgap, free carriers and phonons. The calculated temperature evolution during growth of $In_xGa_{1-x}N$ will not be explored, as there are currently too many unknown physical parameters.

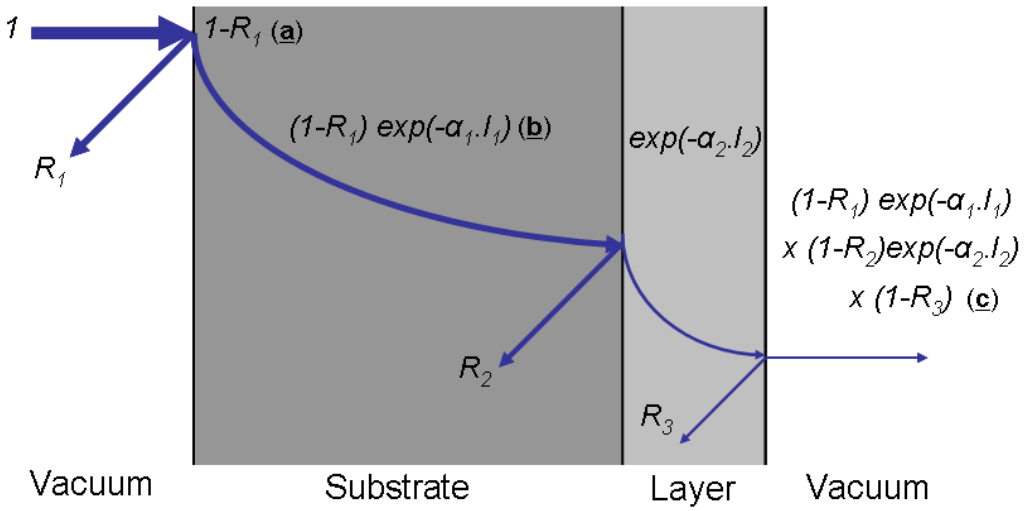

Figure 5.4 – Schematic of radiation pathway for a bilayer structure e.g. film grown on GaAs. Incident radiation is taken as unity, the intensity of radiation that enters the structure is given by (**a**), the intensity of radiation at depth l_1 in first layer is given by (**b**) and the intensity of radiation that leaves the structure is given by (**c**). Percentage of radiation reflected at each interface is R_1, R_2 and R_3.

Model outline

The heater radiation is approximated by a blackbody with spectral radiance (per unit solid angle), $I(\lambda, T)$, that obeys Planck's law

$$I\left(\lambda, T\right) = \frac{2hc^2}{\lambda^5}\left[\exp\left(\frac{hc}{\lambda k_B T}\right) - 1\right]^{-1} \tag{5.2}$$

where h is Planck's constant, c is the speed of light, λ is wavelength, k_B is the Boltzmann constant and T is the temperature (in Kelvin) of the blackbody, i.e. the heater.

A schematic of the radiation pathway throughout the sample is illustrated in figure 5.4. Radiation from the heater is taken as unity and assumed to be normally incident on the back side of the wafer as, in the mini-MBE samples are not mounted on plates. Some reflection, given by the reflectivity $R_x(\lambda)$ (equation 5.3), takes place at this, and subsequent, interfaces due to differences in the complex refractive index of the two media either side of each interface, $\tilde{n}_1$ and $\tilde{n}_2$. The relative amount of radiation transmitted by a layer i at a depth l_i, is $\exp(-\alpha_i.l_i)$ where α_i is the absorption coefficient, given in equation 5.4, which is dependent on the imaginary

part of the refractive index, κ_i.

$$R_x(\lambda) = \left| \frac{\tilde{n}_1(\lambda) - \tilde{n}_2(\lambda)}{\tilde{n}_1(\lambda) + \tilde{n}_2(\lambda)} \right|^2 \tag{5.3}$$

$$\alpha_i(\lambda) = \frac{4\pi\kappa_i(\lambda)}{\lambda} \tag{5.4}$$

The amount of radiation absorbed by a layer is referred to as its absorption factor. This is taken as the difference between the amount of radiation that enters a layer and the amount of radiation that reaches the interface marking the end of the layer, e.g. for GaAs this is given by $(1 - R_1)[1 - \exp(-\alpha_1.l_1)]$.

Absorption of the incident radiation by each layer is allowed to take place through one of three processes:

(i) absorption of photons - for energies, E, greater than the layer's bandgap, generally in the visible range

(ii) absorption due to TO phonon resonances - at energies near to the layer's phonon frequencies, in the mid IR domain

(iii) absorption by free carriers - at energies below the bandgap of the layer

Experimentally derived optical values for $\tilde{n}_i$ and α_i can be used for process (i). For processes (ii) and (iii), n_i and k_i can be deduced from calculated complex dielectric functions using derived physical parameters such as phonon frequencies, plasma frequencies, carrier concentrations etc.

As the GaAs substrate is 350μm thick, any radiation transmitted into the layer with energy larger than the GaAs bandgap is assumed to be absorbed, i.e. $\exp(-\alpha_1.l_1) = 0$. As GaN has a wider bandgap than GaAs, no absorption via process (i) will take place in the GaN layer. Since most of the temperature rise during the growth of InN takes places in the first few minutes, the assumption of total absorption for $E > E_g(\text{InN})$ in the InN layer cannot be applied as epilayer thicknesses are < 10 nm. The absorption coefficient for InN in this energy domain was calculated using

$$\alpha(\lambda) = A(h\nu - E_g)^2 \tag{5.5}$$

where A is an experimentally determined, non-wavelength dependent constant, which was found using reference [131]. The reflectivity at each interface for $E > E_g$ was calculated using optical values for the refractive index of each material.

To calculate the $R_x(\lambda)$ at each interface and $\alpha_i(\lambda)$ of each layer for $E < E_g$ i.e. effects of free carriers and phonons, dielectric functions, $\varepsilon_r(\omega)$, were calculated. These were subsequently used to deduce the real and imaginary parts of the refractive index, as a function of wavelength.

The contribution to the dielectric function due to free carriers is given by

$$\varepsilon_r(\omega) = \varepsilon_{opt}\left[1 - \frac{\omega_p^2}{(\omega^2 - i\gamma\omega)}\right] \tag{5.6}$$

where ε_{opt} is the optical dielectric constant, ω the angular frequency, γ the plasmon damping constant and ω_p the plasma frequency, which is itself determined by the carrier concentration N and effective electron mass m_e^* and is given by

$$\omega_p^2 = \frac{Ne^2}{\varepsilon_{opt}\varepsilon_0 m_e^*} \tag{5.7}$$

where e the charge of an electron and ε_0 the permittivity of free space.

The contribution to the dielectric function due to phonons is given by

$$\varepsilon_r(\omega) = \varepsilon_{opt} + (\varepsilon_{stat} - \varepsilon_{opt})\frac{\Omega_{TO}^2}{(\Omega_{TO}^2 - \omega^2 - i\Gamma\omega)} \tag{5.8}$$

where ε_{stat} is the static dielectric constant, Ω_{TO} the angular phonon frequency and Γ the phonon damping constant.

These two contributions are taken as cumulative and can therefore be combined into one expression:

$$\varepsilon_r(\omega) = \varepsilon_{opt} - \frac{\varepsilon_{opt}\omega_p^2}{(\omega^2 - i\gamma\omega)} + (\varepsilon_{stat} - \varepsilon_{opt})\frac{\Omega_{TO}^2}{(\Omega_{TO}^2 - \omega^2 - i\Gamma\omega)} \tag{5.9}$$

For each layer, the absorption factor for free carriers and phonons was calculated separately. The two absorption factors were then added to give the total relative absorption of each layer for $E < E_g$. This was undertaken to (i) ensure calculations

gave expected characteristic responses and (ii) separate out the two contributions, in order to determine which one is the dominant factor. Checks were undertaken to ensure that reflectivity was not greater than one.

The absorption factor (the percentage of radiation absorbed that entered a layer) for each energy domain was multiplied by the spectral radiance of the blackbody distribution to give a weighted absorption spectrum, i.e. the intensity of radiation absorbed by a layer at each wavelength. The total radiation absorbed by the growing film is given by summing the weighted absorption spectrum from each layer (i.e. substrate and nitride layer). The power of the radiation absorbed by the growing film is calculated by taking the integral of the total weighted absorption spectrum with respect to wavelength.

Finally, the temperature of the sample was found using equation 5.10 which uses the ratio of the power absorbed by GaAs plus the epilayer to just GaAs. Taking the fourth root of this ratio (i.e. assuming Stefan-Boltzmann's law) gives the ratio of the temperature difference (in Kelvin) of the film with respect to the GaAs starting temperature.

$$\sqrt[4]{\frac{Q_S + Q_F}{Q_S}} = \frac{T_{F+S}}{T_S} \tag{5.10}$$

Q_S is the integral of the weighted absorption spectrum of the GaAs substrate, Q_F the integral of weighted absorption spectrum of the layer, T_S the starting substrate temperature and T_{F+S} the temperatures of the grown sample.

By setting l_2 as the thickness of the epilayer (which is calculated using a growth-rate parameter), the theoretical evolution of film temperature can be found.

This model currently lacks a mechanism for heat loss and so it will predict an unbounded increase in temperature until the layer becomes opaque. In reality however, at the start of growth the power absorbed (P_{abs}) by the film is expected to be greater than the power emitted (P_{emit}), as the emissivity of the epilayer is similar to the emissivity of the GaAs substrate. The wavelength dependent emissivity of the layer is predicted to increase as a function of film thickness, until it reaches the value expected for the epilayer [132]. At this point P_{abs} will equal P_{emit}, thermal equilibrium is reached and the temperature is expected to stabilise. The model therefore, is only applicable to the portion of the growth where the temperature is rising. Although it cannot reproduce the whole evolution of growth, it can

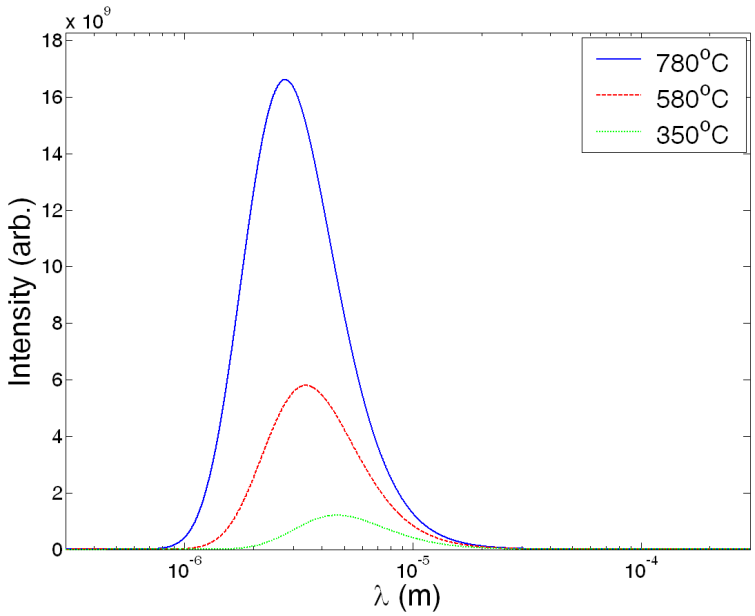

Figure 5.5 – The radiation distribution of a blackbody at (i) temperature of the heater (780 °C), (ii) highest observed sample temperature (580 °C) and starting substrate temperature (350 °C).

identify the mechanisms responsible for the increases in temperature observed.

Other factors not addressed by this model include:

(i) absorption of radiation reflected at the interfaces back into a layer - it is assumed that the intensity of reflected radiation is small cf. radiation that initially entered the layer

(ii) inclusion of a surface electron accumulation layer in InN which is very thin, of the order of a few nm

(iii) angle of transmitted radiation - the heater is positioned very close to sample

(iv) absorption of radiation emitted by the layers - T^4(layer)$<$ T^4(heater) meaning intensity of radiation is much less, see figure 5.5. Additionally, the intensity of the radiation emitted by the sample will be reduced from that shown, due to emissivity

(v) conduction between holder and sample - there is a very small area of contact

	E_g(eV)	N(cm^{-3})	m_e^*/m_e	ε_{opt}	ε_{stat}	Ω_{TO}(cm^{-1})	γ(cm^{-1})	Γ(cm^{-1})
GaAs	1.4	1x10^{7}	0.067	11.0	13.0	268.7	N/A	2.4
GaN	3.4	1x10^{17}	0.22	5.35	9.9	531.7	347	18.4
InN	0.7	6x10^{18}-2x10^{19}	0.1	8.3	12.26	478	265	2

Table 5.2 – The values used in simulations for bandgap, E_g, bulk carrier concentration, N, effective electron mass, m_e^*/m_e, optical and static dielectric constants, ε_{opt} and ε_{stat} respectively, angular wavenumber of TO phonon mode, Ω_{TO} and damping constants of plasmons and phonons, γ and Γ respectively for GaAs, GaN and InN. A growth rate of 100 nm/hr was used for both GaN and InN.

(vi) heat exposure from the cells - the effect of shutter transients is small cf. temperature rises observed and has been taken into account by recording the difference in temperature on closing shutters at end of growth.

Model results

All physical parameters used in the modelling are presented in table 5.2 and were found using references [133] (for GaAs), [134] (for GaN) and [135] (for InN). The InN growth performed for this project has not yet been optimised. For this reason, using a N towards the higher end of most commonly reported values, high 10^{19} cm^{-3}, is reasonable.

Figure 5.6(a) and (b) shows the positions of the wavelength corresponding to the bandgap, TO phonon and plasma frequency (if in range) of GaN and InN respectively, as well as those of the GaAs substrate, all with respect to the blackbody radiation emitted from the heater. A N value of 9×10^{18} cm^{-3} was used to calculate ω_p for InN. These simple representations serve to demonstrate which processes are expected to dominate increases in absorption of the growing films.

As the GaAs substrate is semi-insulating, its associated plasma frequency is outside the wavelength range shown. It can also be seen that the wavelength position of the GaAs TO phonon mode is outside the wavelength range defined by the heater radiation distribution hence, absorption of radiation due to a phonon resonance in GaAs will not take place. The position of the GaAs bandgap occurs just within the left hand tail of the blackbody radiation. In this scenario therefore, very little radiation from the heater is coupled into the GaAs substrate prior to growth.

Figure 5.6(a) shows that the plasma frequency of GaN is also outside the radiation

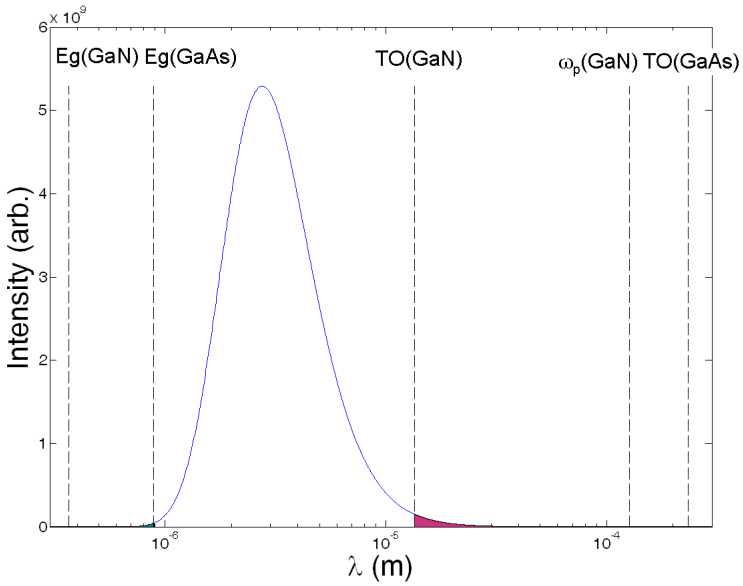

(a) GaN/GaAs

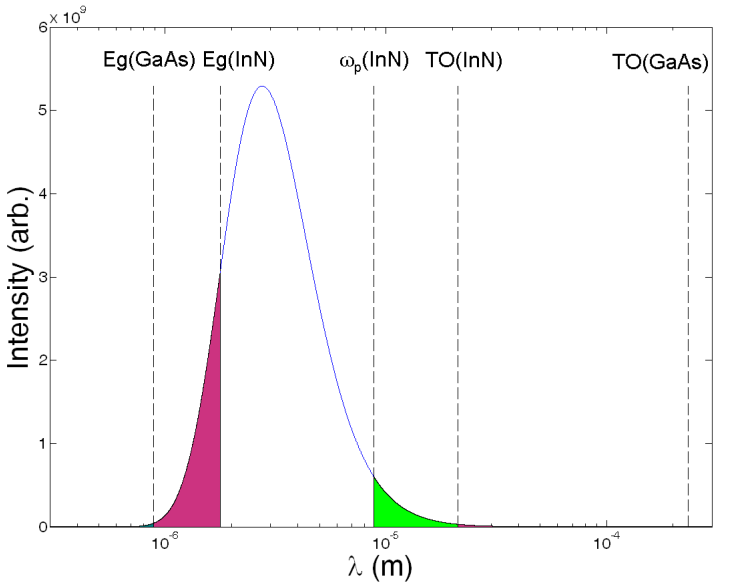

(b) InN/GaAs

Figure 5.6 – Power distribution emitted from a blackbody with temperature of 780 °C (blue solid line). Dashed lines show positions of wavelength (if in range) of the bandgap, Eg, plasma frequency, ω_p, and TO phonon, TO, for GaN/GaAs and InN/GaAs samples respectively with N values of $1 \times 10^{17}\,\mathrm{cm}^{-3}$ and $9 \times 10^{18}\,\mathrm{cm}^{-3}$.

range. In fact, the only additional absorption process available during the growth of GaN on GaAs (compared to just GaAs), is through the GaN phonon mode. However, since this occurs over a narrow wavelength range and corresponds with the right-hand tail (where $I(\lambda, T) \ll I(\lambda, T)_{max}$), the effect is expected to be small.

The schematic in figure 5.6(b) shows that during the growth of InN on GaAs, all three additional absorption processes are available in the InN layer. Absorption due to the InN TO phonon mode is expected to be small, as it is positioned only just inside the blackbody radiation range; where the intensity of radiation is very low. The plasma frequency and bandgap of InN meanwhile, are situated firmly in the middle of the radiation distribution. This suggests that much larger increases in temperature are expected compared to growth of GaN on GaAs. Further analysis is required to determine which, if any, is the dominant process.

The calculated reflectivities, $R(\lambda)$ due to phonons in GaN and GaAs are shown in figure 5.7, $R(\lambda)$ was also calculated for the free carriers (GaAs not shown). As expected, the only contribution that shows a response, within the given wavelength range, is due to the TO phonon resonance in GaN (as this is the only component whose position is situated with the wavelength range). Encouragingly, the response takes the form of the characteristic restrahlen band (whose position of rapid on-set and decrease correspond to the TO and LO phonon modes). Also shown are graphs of the calculated absorption factor and weighted absorption spectrum (which includes the contribution from each material's bandgap) for a 10 nm film of GaN on a 350 µmthick GaAs substrate subjected to radiation of a blackbody at 780 °C. As predicted, the increase in absorption due to the deposition of GaN onto GaAs is small, with the only additional radiation mechanism being due to resonance with of the GaN TO phonon mode.

A graph comparing the calculated and measured temperature evolution for growth of GaN on GaAs is presented in figure 5.8. No adjustable parameters were required to produce the theoretical curve; i.e. all physical parameters were taken straight from the literature. In the region where the temperature is increasing, the model results match the experimental values well, with the predicted rise in temperature increasing slightly faster than the measured rise. As emission of radiation by the film is ignored in the model, the calculation is expected to be an overestimate of the temperature rise.

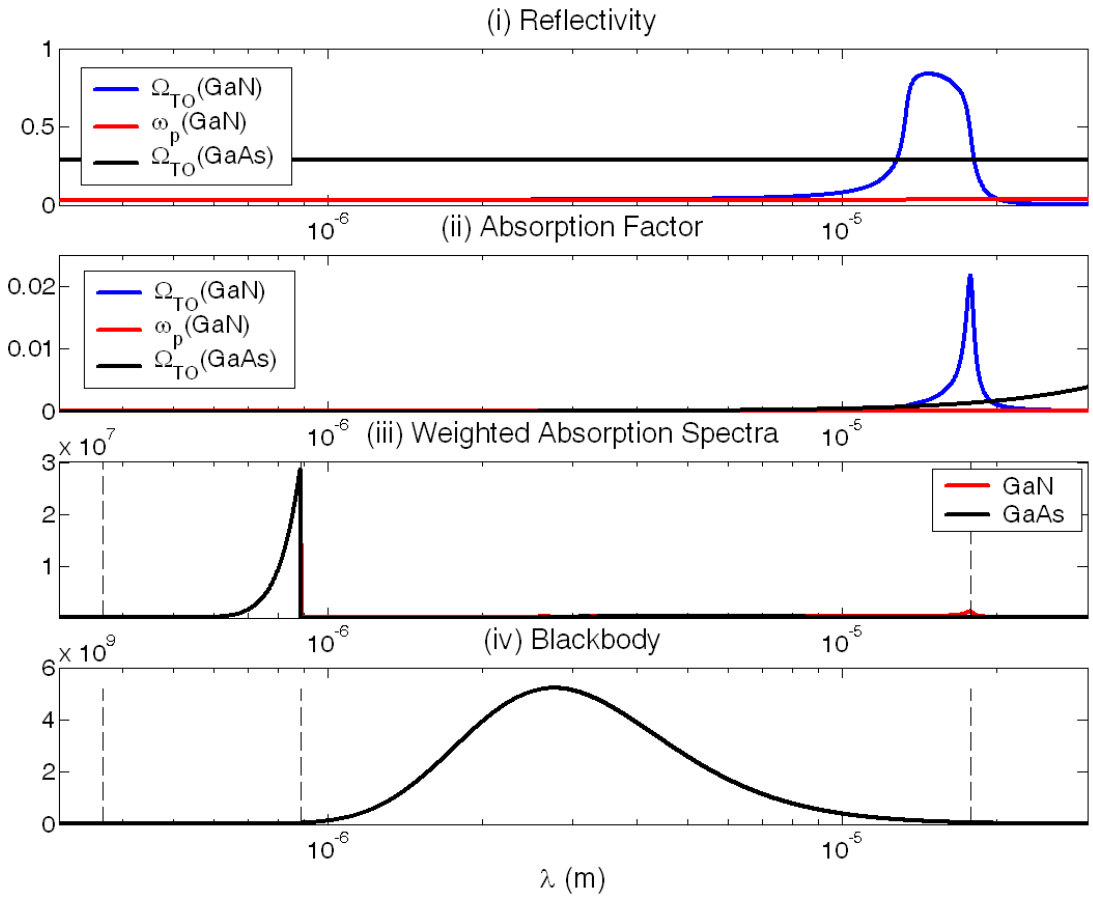

Figure 5.7 – (i) Graph showing the calculated reflectivity of GaN (due to free carriers and TO phonon mode) and GaAs (due to TO phonon mode) (i) within a wavelength range broadly defined by the calculated radiation emitted from the heater, graph (iv), where the wavelength positions (left to right) of Eg(GaN), Eg(GaAs) and Ω_{TO}(GaN) are marked by dashed lines. Also shown is the calculated absorption factor, graph (ii), and weighted absorption spectra, graph (iii), of a 10 nm GaN layer on a 350 μmGaAs substrate, with contributions from each layer's bandgap included.

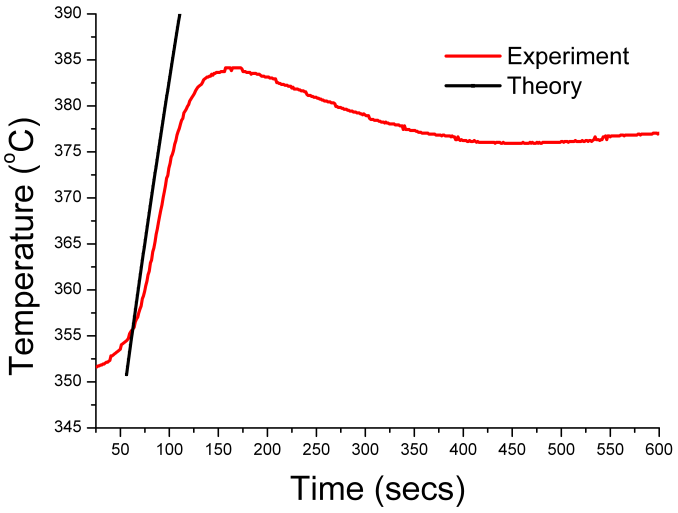

Figure 5.8 – Experimental (red) and simulated (black) evolution of substrate temperature during growth of GaN on GaAs.

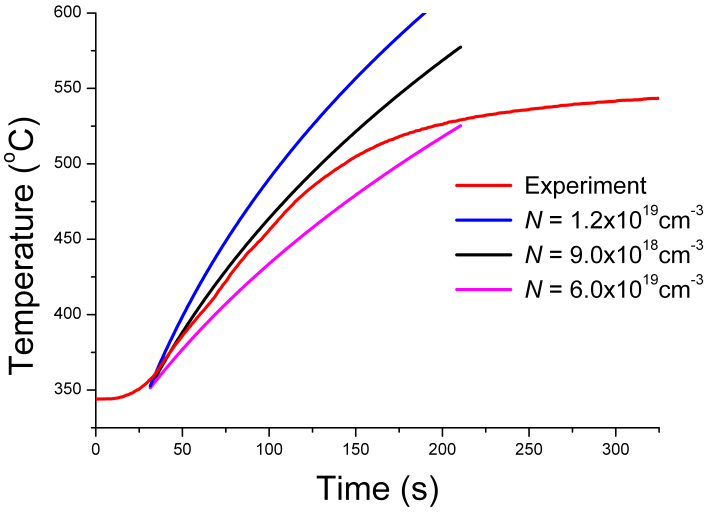

Figure 5.9 – Experimental and simulated evolution of substrate temperature during growth of InN on GaAs. A range of simulated curves were produced using carrier concentration N values of $6 \times 10^{18}\,\mathrm{cm}^{-3}$, $9 \times 10^{18}\,\mathrm{cm}^{-3}$ and $1.2 \times 10^{19}\,\mathrm{cm}^{-3}$.

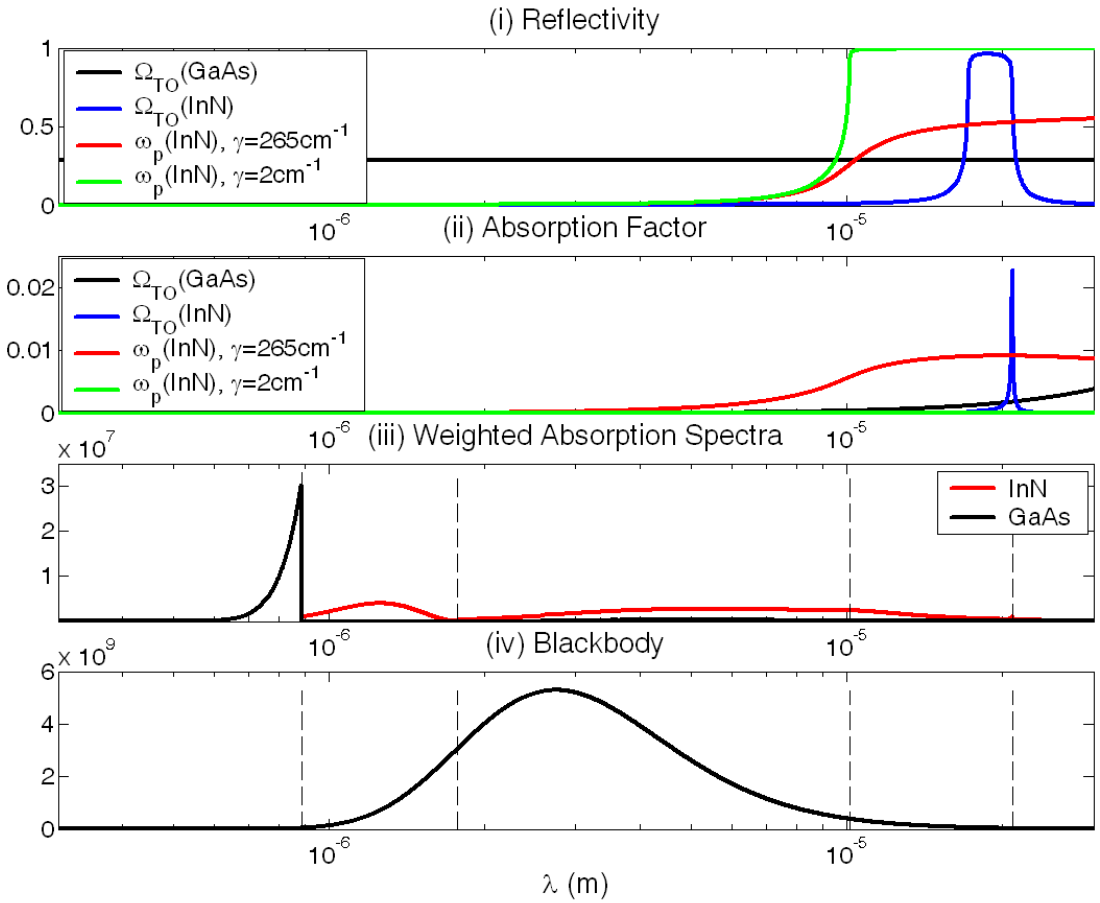

Figure 5.10 – (i) Graph showing the calculated reflectivity of InN (due to free carriers (with two different damping constants) and TO phonon mode) and GaAs (due to TO phonon mode) within a wavelength range broadly defined by the calculated radiation emitted from the heater, graph (iv), where the wavelength positions (from left to right) of Eg(GaAs) and Eg, ω_p and Ω_{TO} of InN are marked by dashed lines. Also shown is the calculated absorption factor, graph (ii), and weighted absorption spectra, graph (iii), of a 10 nm InN layer on a 350 μmGaAs substrate, with contributions from each layer's bandgap included.

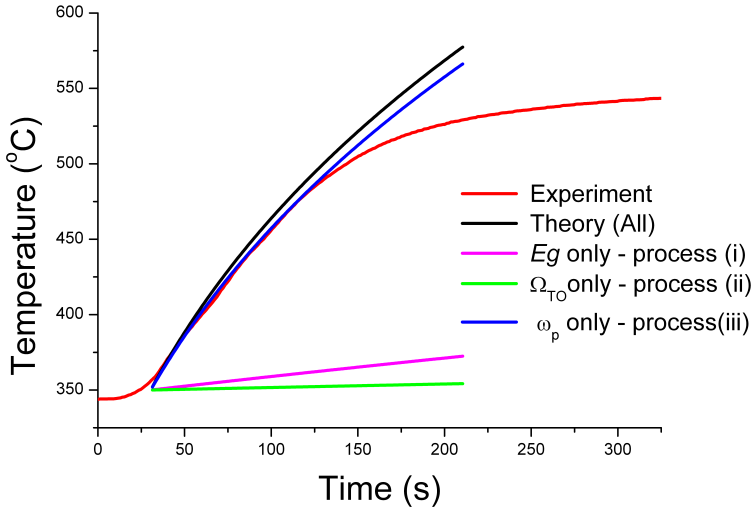

Figure 5.11 – Experimental and simulated (using $N = 9 \times 10^{18}\,\mathrm{cm}^{-3}$) evolution of substrate temperature during growth of InN on GaAs. Also shown is the effect of absorption due to bandgap (Eg), free carriers (ω_p) and phonons (Ω_{TO}) individually. Absorption due to free carriers is the dominant process responsible for the large rise in temperature observed upon commencing growth.

For InN, typical values of the carrier concentration for growth in our MBE system are less well known. N was therefore used as a approximate fitting parameter, with literature values used for all other physical parameters, see table 5.2. Results comparing measured and calculated (with varying N) temperature evolution are displayed in figure 5.9, where it is clear that an N value of $\sim 9 \times 10^{18}\,\mathrm{cm}^{-3}$ gives the best results.

Calculated reflectivities and absorption factors in InN and GaAs due to free carriers and phonons are shown in figure 5.10, which were calculated using $N = 9 \times 10^{18}\,\mathrm{cm}^{-3}$, InN thickness of 10 nm, GaAs substrate thickness of 350 µmand a blackbody at 780 °C. Only factors due to InN show responses in the reflectivity. As in the case of GaN, the InN phonon modes give rise to a characteristic restrahlen band, which consequently results in a sharp absorption factor about the position of the TO phonon mode. Two calculated reflectivities due to free carriers in InN are plotted, one using the measured damping constant of $265\,\mathrm{cm}^{-1}$ [135] and one with a more ideal damping constant of $2\,\mathrm{cm}^{-1}$. The reduced damping constant gives a response expected by a undamped free carrier gas; where $R(\lambda)$ is unity for $\omega \leq \omega_p$ (i.e. $\lambda > \omega_p$) and then decreases for $\omega > \omega_p$, approaching zero at $\omega = \infty$. In reality however, free carriers in semiconductors are associated

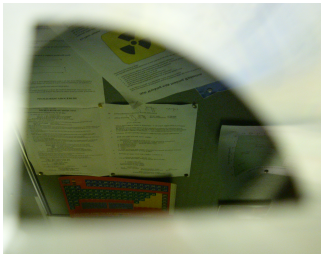

(a) JH92 - $In_{0.8}In_{0.2}N$

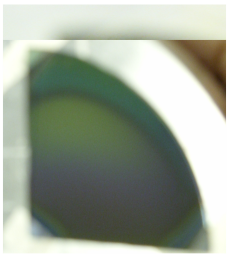

(b) JH95 - $In_{0.8}In_{0.2}N$

Figure 5.12 – Pictures comparing a typical pair of In-rich InGaN with nominally identical compositions grown with (a) and without (b) temperature control; where samples grown without temperature control have a final growth temperature exceeding 500 °C.

with large damping constants. Using the realistic plasmon damping constant for InN however, causes the reflectivity to be significantly less than unity, resulting in absorption over a broad wavelength range; the absorption factor calculated using $2\,\mathrm{cm}^{-1}$ is seen to result in very little absorption. The calculated weighted absorption spectrum for each layer is also shown. For InN, it can be seen that both the E_g and free carriers lead to significant absorption. Analysis shows that the integral of the weighted absorption spectrum due to free carriers is double the integral taken over the bandgap regime. This means that we expect absorption from free carriers to be the dominant process in the temperature increase observed when growing InN on GaAs.

By setting the absorption of two of the three processes to zero, which factors contribute most to the rise in temperature can be determined, figure 5.11. For example, setting the absorption from processes (ii) and (iii) (phonons and free carriers) to zero, shows the effect of growing a narrow bandgap material (process (i)). The results show that, as predicted, the mechanism most responsible for the temperature rise in InN is not the narrow bandgap, but the presence of a large background of free carriers; more specifically, it is the free carriers with their associated large damping constant (which is inversely related to carrier mobility).

5.3.3 Effects of temperature control

$In_xGa_{1-x}N$ films were grown at a near-constant temperature by manually changing the power to the heater. In conjunction with samples already described, this allows the effects of uncontrolled temperature rises on film quality to be assessed. Sets

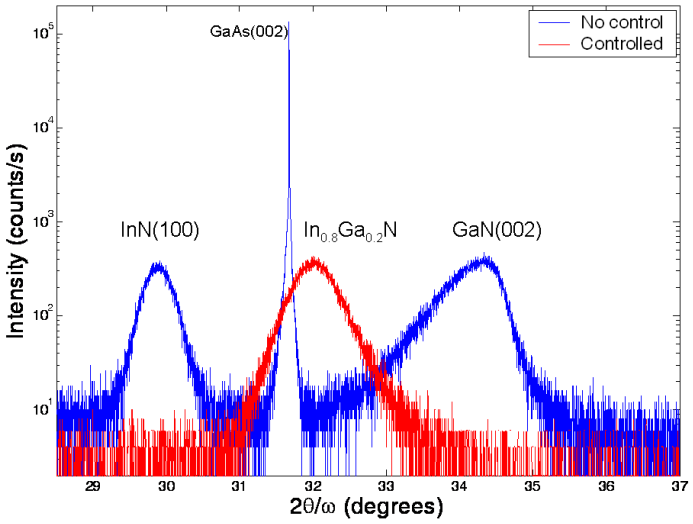

(a) $In_{0.8}Ga_{0.2}N$

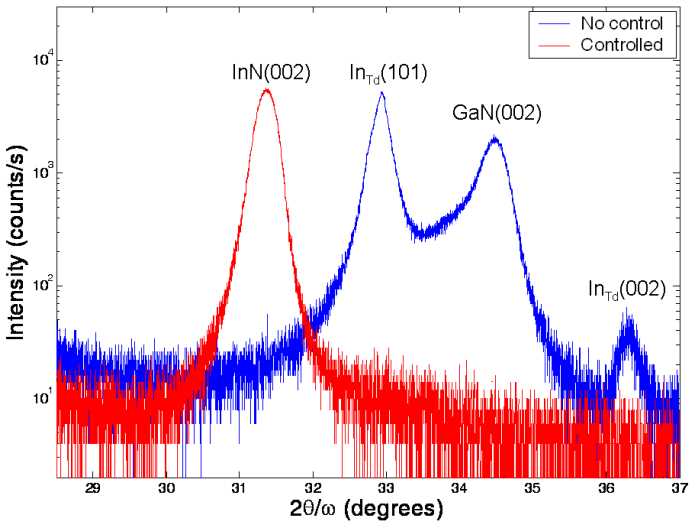

(b) InN

Figure 5.13 – $2\theta/\omega$ XRD linescans comparing nominally identical $In_xGa_{1-x}N/GaAs(0\,0\,1)$ structures grown with (red) and without (blue) temperature control for (a) $x = 0.8$ and (b) $x = 1$ respectively. The temperature controlled samples shows single phase InGaN material, while the samples grown without temperature control have undergone phase separation.

of samples with compositions of $x = 0.8$ and $x = 1$ exist that can be used for this purpose.

Figure 5.12 shows photographs comparing $In_{0.8}Ga_{0.2}N$ grown (a) at a steady growth temperature of 500 °C and (b) without temperature control. It can be seen that the sample allowed to rise in temperature shows roughening and segregation to such an extent, that it can be witnessed by eye. In contrast, the sample grown with temperature control has a highly reflective and homogeneous surface, suggesting improved material quality and showing no evidence for formation of metal droplets. The two equivalent samples for InN (not shown) display similar results. $In_xGa_{1-x}N$ samples with $x < 0.8$ grown without temperature control, meanwhile do not exhibit the same mottled surfaces. This would imply that the factor which is detrimental to surface quality and leads to phase separation is the final temperature exceeding 550 °C. However, while the surfaces may appear to be of better quality, $2\theta/\omega$ linescans (not shown) exhibit low intensity peaks, that are not well defined, suggesting amorphous or microcrystalline material. This poor material quality is most likely a result of low growth temperatures.

X-ray results comparing the effect of temperature control on structural quality are displayed in figure 5.13. The $2\theta/\omega$ linescans for both the temperature controlled samples show single-crystalline, single-phase material. The XRD results of the uncontrolled temperature samples meanwhile reveal a different story. For $In_{0.8}Ga_{0.2}N$, peaks due to InN(1 0 0) (note: not InN(0 0 2)) and GaN(0 0 2) are present. The GaN peak is seen to be asymmetric. This could be due to either Ga-rich InGaN being present with a varying alloy composition, the presence of In droplets, InN(1 0 1) or a combination of all of these. The XRD results of the InN sample grown without temperature control however, show the presence of In and GaN, but no InN. Since there was no Ga flux present during the growth, the GaN peak most likely originates from nitridation of the GaAs substrate. The absence of a InN peak suggests that in this instance, all InN (if formed in the first place) decomposes, with N evaporating from the surface, leaving behind In droplets.

Uncontrolled temperature rises clearly have an impact on the material quality of $In_xGa_{1-x}N$. This is attributed to the growth temperature exceeding the decomposition temperature of InN.

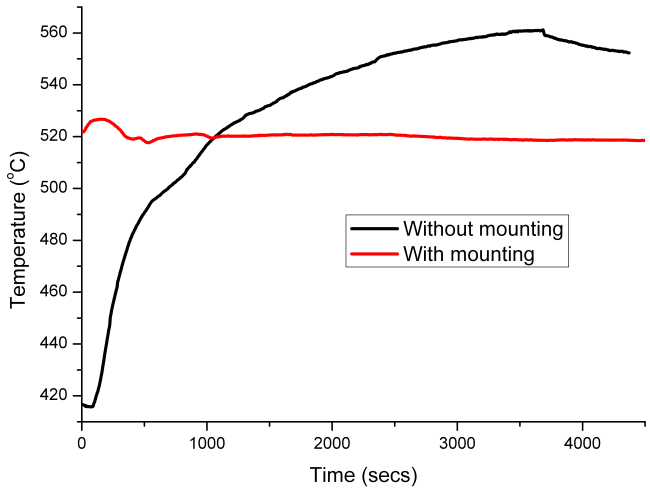

Figure 5.14 – Temperature evolution of two $In_{0.75}Ga_{0.25}N$ samples grown (black) without mounting and (red) substrate mounted on a PBN plate.

5.3.4 Effects of sample mounting

The large temperature rises observed during the growth of In-rich InGaN on GaAs have been attributed to the configuration of the MBE chamber. As samples in the mini-MBE machine cannot be mounted onto a plate within the substrate holder, heat can only be coupled into the wafer radiatively. The choice of substrate and heater temperature however, mean prior to growth, very little of the radiation emitted by heater can be absorbed by the sample. Upon depositing a small amount of In-rich InGaN, additional mechanisms of absorbing the heater radiation become available, resulting in a rapid rise in substrate temperature. If therefore, the growths were repeated, but on a mounted substrate, then the following is predicted: (i) substrate temperature would not increase beyond that expected for shutter transients and (ii) heater power required to achieve the same starting substrate temperature would be lower.

To this end, two $In_{0.75}Ga_{0.25}N$ samples were grown by R. Campion in the Gen III, results of the temperature evolution during growth of the samples are shown in figure 5.14. The sample grown on a substrate that is not mounted, shows similar temperature characteristics of the samples grown in the mini-MBE system. Upon starting growth a rapid rise in temperature is observed, followed by a slow levelling off to plateau at $\sim 560\,^{\circ}C$. The sample grown mounted on a PBN plate meanwhile,

displays very different behaviour. A small initial rise of $\sim 10\,^{\circ}$C is witnessed. This is attributed to exposure of an increased heat load resulting from opening the cells, i.e. shutter transients. This rise however, is soon followed by a fall in temperature at approximately the same rate as the initial increase. At this point, manual temperature control in the form of up-ramps (i.e. heater power needed to be increased), was required in order to maintain a growth temperature of $520\,^{\circ}$C. This can be understood in terms of roughening. On starting growth, no additional radiation can be coupled into the sample therefore, large temperature rises cannot occur. The relatively smooth GaAs surface is soon replaced by a much rougher InGaN surface changing the emissivity. This results in more emission which leads to a lower growth temperature.

As predicted, substrates that are mounted on PBN plates, exhibit very different temperature characteristics during growth than their non-mounted counterparts. Without mounting, the sample temperature of In-rich InGaN rises very rapidly, soon after starting growth. In-rich InGaN samples grown on mounted substrates, show a small initial rise in temperature due to shutter transients, followed by a gradual decrease in temperature, attributed to surface roughening.

5.4 Effects of Growth Temperature

Three nominally identical $In_{0.8}Ga_{0.2}N$ samples were grown at different substrate temperatures. XRD analysis, figure 5.15, reveals that growing at temperatures significantly above and below $500\,^{\circ}$C, leads to a degradation in material quality. A $2\theta/\omega$ linescan of the $500\,^{\circ}$C grown sample shows a single symmetric peak assigned as the 002 reflection from InGaN. Analysis of the 2θ position yields a In composition of 79.4%, which is in very good agreement with the nominal value of 80%. The sample grown at $450\,^{\circ}$C shows evidence for a peak originating from diffraction of GaN, in addition to the much stronger InGaN peak. The InGaN composition of this sample was calculated to be $x = 0.876$ (Ga = 12.4%), which is significantly different from the nominal composition. If phase separation leading to formation of GaN occurs, then this would lead to less Ga being available for incorporation into InGaN, thus increasing the apparent In content of the alloy. The broad signal present from $\sim 33.5 - 35^{\circ}$ could be due to the existence of Ga droplets and/or Ga-rich InGaN; further analysis would be required to positively

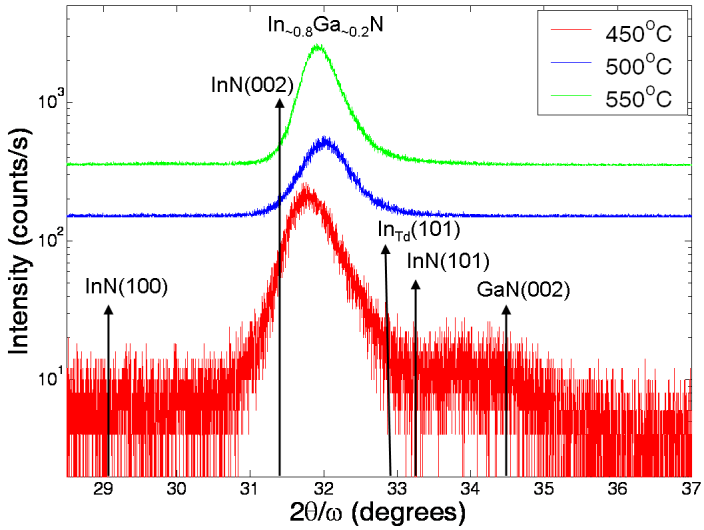

Figure 5.15 – $2\theta/\omega$ XRD linescans comparing three nominal identical $In_{0.8}Ga_{0.2}N$ samples grown at 450 °C, 500 °C and 550 °C.

identical its origin. While the linescan of the sample grown at 550 °C does not show any distinct peaks in addition to InGaN, there is evidence of poorer material quality when compared to the sample grown at 500 °C. The InGaN peak is asymmetric with broadening on the right hand side. This could be due to the presence of either In droplets or InN(1 0 1), but considering its broad nature, it is most likely due to alloy fluctuations. Analysis of the peak position gives a In composition of $x = 0.821$ (Ga= 17.9%).

Within the temperature intervals investigated in this work therefore, an optimum growth temperature for growth of $In_{\sim 0.8}Ga_{\sim 0.2}N$ has been found to be 500 ± 25 °C.

5.5 Alloy Control

The total group III flux that represents stoichiometric growth for InGaN, was found by growing a series of $In_{0.8}Ga_{0.2}N$ samples at 500 °C. The gallium and nitrogen fluxes were kept constant, while the indium cell temperature was increased to find the maximum flux that did not result in droplets being present on the surface. Gallium is assumed to have a unity sticking coefficient. Using the measured total flux value that represents stoichiometry and a gauge sensitivity factor of Ga to In of 1.4, $In_xGa_{1-x}N$ samples were grown for nominal gallium compositions of

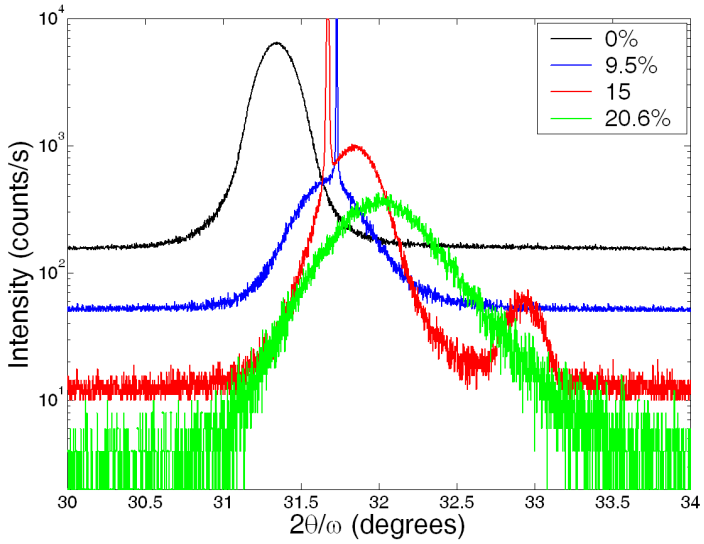

Figure 5.16 – $2\theta/\omega$ XRD linescans comparing 1 hr growth at 500 °C of $In_{1-y}Ga_yN$ for nominal y values of 0.0 (black), 0.1 (blue) and 0.2 (green and red). Data are plot from top to bottom in increasing Ga (y) content.

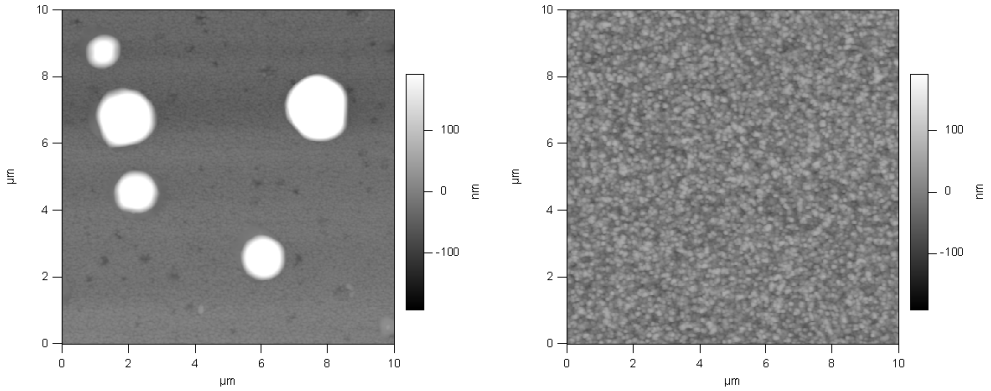

(a) Group III-rich conditions (b) Stoichiometric conditions

Figure 5.17 – 10x10 µm AFM images of $In_{0.8}Ga_{0.2}N$ grown at 500 °C under (a) group III-rich and (b) stoichiometric conditions. Both images have been to scaled to a vertical range of 383 nm.

0%, 10% and 20% in order to investigate how easy it is to control composition.

The XRD results for these samples are presented in figure 5.16, along with a $2\theta/\omega$ linescan taken of $In_{0.8}Ga_{0.2}N$ grown under group III-rich conditions (i.e. an In flux which is too high). For samples grown at stoichiometric conditions, the linescans all show a single peak representative of single-phase InGaN material. Analysis of the peak composition yields gallium concentrations of $0, 9.5$ and 20.6% for nominal values of $0, 10$ and 20% respectively; showing excellent agreement with nominal and actual compositions. This suggests that alloy control of In-rich InGaN is indeed, relatively straight forward. It can be seen however, that the FWHM of the peak increases with increasing gallium composition, indicating worsening material quality for InGaN samples with similar In and Ga mole fractions. AFM results also show deteriorating material quality for increasing gallium concentrations, as witnessed by rougher surfaces: RMS surface roughnesses of 7.7, 12.7 and 25.6 nm for nominal gallium concentrations of 0, 10 and 20% respectively.

The XRD result taken of the sample that was determined to have been grown under group III-rich conditions shows two peaks; assigned as $In_{0.85}Ga_{0.15}N$ and $In_{Td}(1\,0\,1)$. The sample appeared 'milky', suggesting the formation of In droplets, which is confirmed by these XRD results. AFM images also show the presence of droplets on the surface, figure 5.17(a). Droplets were not witnessed in AFM images taken of the $In_{0.8}Ga_{0.2}N$ sample grown under N-rich conditions, figure 5.17(b).

5.6 Mn-doped $In_{0.8}Ga_{0.2}N$

A nominal $GaMn_{0.03}As$ sample was grown in order to calibrate the Mn flux in the mini-MBE system. Analysis of SQUID measurements performed on the sample (not shown) yielded a Mn concentration of 2.9%, showing good agreement with nominal and actual Mn composition.

Initially, a set of Mn-doped $In_{0.8}Ga_{0.2}N$ samples were grown at 500 °C for a range of Mn fluxes. Samples were visually assessed after growth to determine whether the Mn flux had been incorporated into the alloy, by looking for evidence of droplets on the surface. In order to confidently assign the onset of droplet formation to segregation of Mn, growth was performed under N-rich conditions, therefore any effect on the surface is solely due to Mn and not due to an excess flux of group III

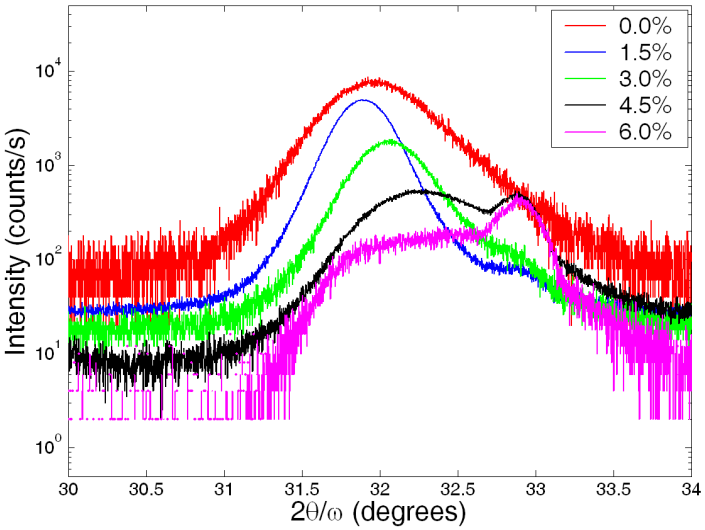

Figure 5.18 – $2\theta/\omega$ XRD linescans comparing $In_{0.8}Ga_{0.2}N$ grown at 500 °C doped with varying amounts of Mn. Data are plotted from top to bottom in order of increasing nominal Mn content.

material. Using the visual inspection method, Mn was found to be incorporated into the film up to concentrations between 3 and 3.5%.

XRD results, displayed in figure 5.18, show that with increasing Mn content, the InGaN peak shifts to the right. They also show the onset of a peak at $\sim$ 32.9°, which has been assigned as $In_{Td}(1\,0\,1)$. This peak is seen to increase in intensity with increasing [Mn]. The FWHM of the InGaN peak is seen to increase significantly for Mn concentrations greater than 4.5%. The InGaN peak in the [Mn]=6% sample in particular, is very broad (compared to other samples) and is also of a lower intensity than the peak due to diffraction from In droplets. Although the InGaN peak is seen to shift position with increasing Mn flux, this effect cannot be attributed to Mn incorporation leading to an increase in lattice parameter. This is due to the fact this is accompanied with an presence of In droplets. If In has segregated, then this would also lead to decreased lattice parameter due to a apparent larger Ga content in the film. It is possible therefore, that Mn decreases the lattice parameter of InGaN, but it is not observed due to the competing increase in lattice parameter resulting from a reduced In content. For samples that were determined (visually) to have segregated Mn, diffraction from GaN was also witnessed in the XRD results. This suggests that excess Mn, drives the formation of In droplets and GaN and that witnessing a GaN peak in

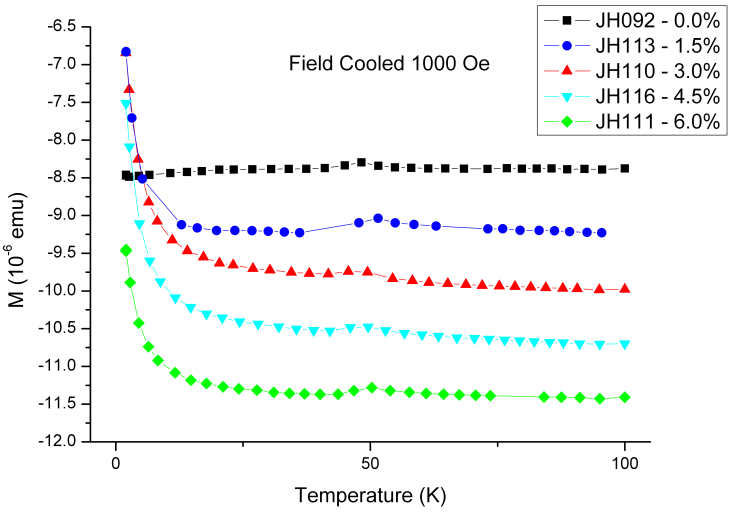

Figure 5.19 – Temperature dependence of magnetization under an external applied field of 1000oe for nominal $In_{0.8}Ga_{0.2}MnN$ grown at 500 °C for different nominal Mn concentrations.

XRD can be used as an indicator of Mn segregation. The In droplet peak cannot be used as an indicator as it has been seen that In droplets form in InGaN samples grown with too much group III flux, which can easily occur. Although the sample with 1.5% Mn was shown to have In droplets, this was attributed to growth not occurring under N-rich conditions and not due to the presence of Mn. This is supported by two facts: (i) the 3.0% Mn sample does not show peaks due to In and (ii) whilst AFM images do show formation of droplets, these are reduced in height by $\sim 1/2$ compared to droplets witnessed in all the samples deemed to have Mn segregation.

SQUID measurements were performed on these samples, with results shown in figure 5.19. While they show that samples grown exposed to a Mn flux are paramagnetic (as witnessed by increase in magnetic moment with decreasing temperature), they cannot be used to obtain quantitative results, i.e. the relative amount of [Mn] contributing to the magnetism. This is due to oxygen contamination, which gives rise to the feature at $\sim$ 50K that is present in all measurements. At temperatures below 50K, oxygen behaves anti-ferromagnetically, which causes the apparent magnetic moment to decrease. This competing signal can vary with each measurement, so therefore absolute values cannot be used.

PL measurements of these preliminary InGaMnN samples were also taken by Dr. C. Farmer at the University of Glasgow, in order to determine whether there is

an intermediate band present. No signal however, was observed from any of the samples, including the InGaN control sample. This was not entirely unexpected and has been attributed to poor material quality.

Sets of samples were then grown at 550 °C and 450 °C to investigate whether the growth temperature has an effect on how much Mn can be incorporated into the film before a transition in film quality is observed. For a growth temperature of 550 °C, a nominal Mn flux of just 1.5% was found to result in segregation. This is not unexpected, as the decomposition temperature of InN for growth conditions investigated in this work, has been found to be $\sim$ 580 °C. It is possible that very small amounts of Mn ($\leq$ 1%) can be incorporated into $In_{0.8}Ga_{0.2}N$ grown at 550 °C, but this cannot be determined from results presented in this work.

For samples grown at 450 °C, the Mn flux was not seen to have a detrimental efect on film quality until nominal mole fractions between 3.5 and 4.5% were used, $\sim$ 0.5% higher than that reported for growth of InGaMnN at 500 °C. This suggests therefore, that there is a relationship between maximum Mn concentration and growth temperature. However, since in the scope of the IBPOWER project, Mn concentrations of less than 1% are envisaged, doping with Mn is not expected to significantly alter the growth conditions as found by optimising the growth of $In_{0.8}Ga_{0.2}N$.

Summary of all growth details and results can be found in table 5.3.

5.7 Conclusions and Further Work

The work presented in this chapter represents preliminary growth studies into In-rich InGaN and Mn-doped $In_{0.8}Ga_{0.2}N$.

Temperature rises during the growth of $In_xGa_{1-x}N$ on free-standing GaAs substrates have been observed and were found to increase with increasing In content. A semi-quantitative model has been presented, which despite its limitations, we believe explains the origin of the rises observed during the growth of GaN and InN on GaAs. The rises in temperature largely occurs as only a small percentage of the heater radiation is coupled into the substrate prior to growth. The small rise in GaN is a result of a frequency difference of the phonons in GaAs and GaN. The large rise in InN is due to the high numbers of free carriers present in the InN

Sample	Temp	[Mn]	Surface	Peaks
JH 130	550 °C	0%	Clear	$In_{0.79}Ga_{0.21}N^{\dagger}$ InN(100)
JH 129	550 °C	1.5%	Droplets	InGaN (very broad) InN(100) GaN(100), GaN(002) In(101)
JH 125	550 °C	3.0%	Droplets	InN(100) GaN(002) In(101), In(110)
JH 109	500 °C	0%	Clear	$In_{0.82}Ga_{0.18}N$
JH 113	500 °C	1.5%	Clear*	$In_{0.84}Ga_{0.16}N$ In(101), In(002)
JH 110	500 °C	3.0%	Clear	$In_{0.77}Ga_{0.23}N$
JH 134	500 °C	3.5%	Droplets	$In_{0.75}Ga_{0.25}N$ InN(100) GaN(002) In(101), In(002)
JH 116	500 °C	4.5%	Droplets	$In_{0.72}Ga_{0.28}N$ InN(100) GaN(002) In(101), In(002), In(110)
JH 111	500 °C	6.0%	Droplets	InGaN (very broad) InN(100) GaN(002) In(101), In(002), In(110)
JH 131	450 °C	3.0%	Clear	$In_{0.85}Ga_{0.15}N$
JH 133	450 °C	3.5%	Clear	$In_{0.83}Ga_{0.17}N$
JH 132	450 °C	4.5%	Droplets	$In_{0.84}Ga_{0.16}N$ InN(100) GaN(002) In(101), In(002), In(110)

Table 5.3 – Summary of growth details and results for Mn-doped $In_{0.8}Ga_{0.2}N$: † 002 reflection, ∗ smaller droplets were witnessed in AFM images, but were approximately half the height of the droplets observed in other samples.

layer. The narrow bandgap of InN was calculated to have a much smaller effect on growth temperature. The lack of a heat loss mechanism in the model currently means that it cannot yet be used to for other growth scenarios. Model results are only presented for GaN and InN as too many unknowns exist for $In_xGa_{1-x}N$. Several factors were ignored in the model however, since good agreement was obtained for GaN, without the need for a fitting parameter, these are deemed to be acceptable assumptions. Different system configurations were predicted, and have been shown, to yield different results. Growth on substrates mounted on PBN plates were found to actually lead to small temperature decrease.

A growth temperature of $500 \pm 25\,^{\circ}C$ results structurally in the best material for $In_{0.8}Ga_{0.2}N$. Alloy control proved to be relatively straight forward and was achieved by controlling the Ga:In flux ratio and ensuring growth took place close to stoichiometry, most likely under slightly N-rich conditions. Further work to find the optimum growth temperature to a higher degree of accuracy is the logical next step. Manually controlling the temperature can still lead to temperature changes of $20\,^{\circ}C$, therefore future growths should be carried out on substrates mounted on PBN plates; either in the Gen III or by modification of the mini-MBE sample holder. There is also room for optimisation by more closely monitoring the Ga and In fluxes.

A transition in film quality was found to occur if $In_{0.8}Ga_{0.2}N$ was grown exposed to a critical Mn flux. This critical Mn flux was found to be a function of growth temperature; for $In_{0.8}Ga_{0.2}N$ grown at $550\,^{\circ}C$, a nominal Mn composition of 1.5% was found to result in poor film quality, while samples grown at 500 and $450\,^{\circ}C$ were found to withstand nominal Mn concentrations up to (but not including) 3.5 and 4.5% respectively. Samples that experienced a structural transition were accompanied by the onset of a peak in XRD originating from GaN. Large amounts of Mn were also found to promote the formation of In droplets. No work was presented on the form that Mn was deposited in the film, e.g. InGaMnN or Mn_xN_y secondary phases. Analysis by SIMS (in order to determine the total Mn concentration), SEM in conjunction with EDX (in order to identify phases present on surface of droplets) or TEM with SAD (investigate structure of the material and identify phases present) are suggested for further work.

Before investigating the concept of an intermediate band, good-quality (as determined by PL) InGaN and InGaN in a p-n junction need to be established. In

addition to investigating a narrower range of growth temperatures and fluxes, the use of buffer layers (including low temperature buffer layers) of InN or GaN could be explored.

Chapter 6

Summary of Major Results

GaAs was grown at low temperatures in order to investigate whether it grows in a rock-salt phase versus the conventional zinc-blende structure. For thickness up to 0.5μm, it was found that when grown by MBE, GaAs is no longer deposited in a epitaxial single-crystalline manner at a growth temperature at sim150 °C. EXAFS studies however, show that GaAs remains zinc-blende when grown at temperatures down to 120 °C. As XRD measurements show no measurable long-range order, this would suggest that the LT GaAs material is microcrystalline. The cause of increased disorder with decreasing growth temperature is attributed to the incorporation of excess arsenic, in the form of antisite defects. Preliminary work on the growth of LT GaAs using migration enhanced epitaxy (MEE) was carried out. Periodic pauses between closing of the arsenic cell and opening the gallium cell were designed to allow time for the evaporation of excess As from the surface. Using this method, single crystalline GaAs was obtained at a growth temperature of 115 °C.

XRD and absorption measurements show that GaAs grown in the presence of a sublimed AlN flux, are structurally and optically different to GaAs. Whether this is due to the presence of defects or the incorporation of Al and/or N is unclear. Currently therefore, the question of whether AlN can be used as a nitrogen source is unanswered.

Epitaxial growth of ScN on c-GaN(0 0 1), GaAs(0 0 1) and ScAs(0 0 1) has been reported. Despite the lattice match, ScN grows in a (1 1 1) orientation on c-GaN(1 0 0), for a variety of Sc:N flux ratios and growth temperatures (up to

$\sim$ 700 °C). This appears to be the first incidence in the literature, of the orientation of ScN not being pre-determined by the material it was deposited on. Growth of ScN on GaAs(1 0 0) mostly results in ScN with a twinned (1 1 1) orientation, though a (1 1 0) orientation can be obtained under certain conditions. The ScN(1 1 1) films were found to be of poor-quality with either an amorphous or microcrystalline structure. ScN grown on ScAs(0 0 1) was found to result in a (1 0 0) orientation. RHEED indicated growth took place in a 2D growth mode with the surface showing a (1x1) reconstruction. No investigation into Sc:N flux ratio, growth temperature or nucleation conditions has so far, taken place. GaN grown on ScN(0 0 1) surfaces was found to result in rough c-GaN(0 0 1) films, though growth conditions have yet to be optimised.

TEM analysis shows that for ScN interlayers in c-GaN(0 0 1) with thicknesses greater than 5nm, stacking faults running along {1 1 1} formed in c-GaN(1 0 0) terminate at the c-GaN/ScN interface. GaN grown atop ScN(1 1 1) however, crystallises in the hexagonal polymorph. ScN thicknesses of $\sim 1-2$nm meanwhile, result in overgrowth of GaN in the cubic phase, however no significant reduction in stacking fault density or surface roughness is observed. This leads to the conclusion that the use of ScN interlayers is not a suitable method for reducing the defect density of c-GaN(0 0 1).

Growth of nominal hexagonal and cubic ScGaN on GaAs, has taken place across the whole compositional range in nominal 20% intervals. RHEED analysis showed rock-salt like structures for Sc concentrations greater than 70%, amorphous structures for [Sc]=60%, intermediate structures for [Sc] = 20 and 40% and cubic or hexagonal for GaN. XRD analysis however, showed the material quality of Sc-rich samples in the hexagonal series to be poor. Although relatively good-quality c-ScGaN was obtained, it was not possible to confirm whether the material had a cubic (001) orientation, as the peak position that this would lead to, also contains contributions from the c-GaN(0 0 1) buffer layer. Bandgap of all samples was measured using ORS, whereby it was found that there was not a linear dependence with composition. For Ga-rich compositions, the bandgap was found to vary linearly. There is tentative evidence for 3 regimes of growth for (I) high Ga, (II) intermediate Ga and (III) low Ga compositions, as reported by Constantin [78].

Initial investigations into the growth of ScMnN resulted in films which were paramagnetic, opposed to ferromagnetic as predicted by Herwadkar and Lambrecht [9].

This is possibly due to the poor-material quality of the host semiconductor, which itself is due to growth taking place on GaAs.

Temperature rises during the growth of $In_xGa_{1-x}N$ on free-standing GaAs substrates have been observed and were found to increase with increasing In content. A semi-quantitative model has been presented to explains the origin of the rises observed during the growth of GaN and InN. The small rise in GaN is a result of a frequency difference of the phonons in GaAs and GaN. The large rise in InN is due to the high numbers of free carriers present in the InN layer. The narrow bandgap of InN was calculated to have a far smaller effect on growth temperature. The rises in temperature largely occur, as only a small percentage of the heater radiation is coupled into the substrate prior to growth. Different system configurations were predicted, and have been shown, to yield different results. Growth on substrates mounted on PBN plates were found to actually lead to a small temperature decrease.

A growth temperature of $500 \pm 25\,^{\circ}C$ results in the best structural material for $In_{0.8}Ga_{0.2}N$. Alloy control proved to be relatively straightforward and was achieved by controlling the Ga:In flux ratio and ensuring that growth took place close to stoichiometry, under slightly N-rich conditions.

A degradation in film quality was found to occur if $In_{0.8}Ga_{0.2}N$ was grown exposed to a critical Mn flux. This critical Mn flux was found to decrease with increasing growth temperature. Samples that experienced a structural transition were accompanied by the onset of a peak in XRD originating from GaN. Large amounts of Mn were also found to drive the formation of In droplets. Further work is required to determine the detailed structure of $In_{0.8}Ga_{0.2}N$ films containing Mn.

Appendix A

Calculations

A.1 Relative flux ratio of Sc to Ga

There are two factors which affect the flux scale factor, SF, between two sources: (i) the density of the flux and (ii) sensitivity of the flux gauge itself. Only relative flux scale factors are required, in this instance, the scale factor of scandium is calculated relative to a gallium flux.

The velocity of a flux beam is a function of both its temperature, T, and atomic/molecular weight M. This is related to the measured flux by:

$$\text{Flux} \propto \text{Density}$$
$$\text{Density} \propto 1/\text{Velocity}$$
$$\text{Velocity} \propto \sqrt{\frac{T}{M}}$$

The sensitivity of the gauge, S, for a particular element of atomic number N, can be calculated using the following equation:

$$S = 0.038N + 0.465$$

Material	**Sensitivity**	**Typical T**
$^{70}_{31}$Sc	1.643	900 °C
$^{45}_{21}$Sc	1.263	1300 °C

Sensitivity component of SF:

$$\begin{aligned} \mathrm{S_{Sc}} &= \mathrm{X} \times \mathrm{S_{Ga}} \\ \mathrm{X} &= \mathrm{S_{Sc}}/\mathrm{S_{Ga}} \\ &= 1.263/1.643 \\ &= 0.76 \end{aligned}$$

Density component of SF:

$$\begin{aligned} \mathrm{K} &= \frac{\sqrt{T_{\mathrm{Ga}}}}{\sqrt{T_{\mathrm{Sc}}}} \times \frac{\sqrt{M_{\mathrm{Sc}}}}{\sqrt{M_{\mathrm{Ga}}}} \\ &= \frac{\sqrt{990+273}}{\sqrt{1330+273}} \times \frac{\sqrt{45}}{\sqrt{70}} \\ &= 0.88 \times 0.80 \\ &= 0.70 \end{aligned}$$

Combined scale factor:

$$\begin{aligned} SF(\mathrm{Sc{:}Ga}) &= \mathrm{X} \times \mathrm{K} \\ &= 0.70 \times 0.76 \\ &= 0.54 \end{aligned}$$

i.e. for a given gallium flux, the equivalent scandium flux is approximately half.

A.2 Mn concentration of JH 178

Total magnetic moment:

$$\begin{aligned} &= \sqrt{\text{Moment along } [110]^2 + \text{Moment along}[1\bar{1}0]^2} \quad \text{emu} \\ &= \sqrt{(1.295 \times 10^{-5})^2 + (5.018 \times 10^{-6})^2} \quad \text{emu} \\ &= 1.389 \times 10^{-5} \text{ emu} \end{aligned}$$

Volume of sample:

$$\begin{aligned} &= \left(5 \times 10^{-3}\right) \times \left(4 \times 10^{-3}\right) \times \left(12.5 \times 10^{-9}\right) \text{ m}^3 \\ &= 2.5 \times 10^{-13} \text{ m}^3 \end{aligned}$$

Moment of 1 Mn atom:

$$\begin{aligned} 4\mu_B &= 4 \times \left(9.274 \times 10^{-21}\right) \text{ emu} \\ &= 3.710 \times 10^{-20} \text{ emu} \end{aligned}$$

Number of Mn atoms:

$$\begin{aligned} &= 1.389 \times 10^{-5} / 3.710 \times 10^{-20} \\ &= 3.744 \times 10^{14} \end{aligned}$$

No of Mn atoms per 1 m^{-3}:

$$\begin{aligned} &= 3.744 \times 10^{14} / 2.5 \times 10^{-13} \\ &= 1.498 \times 10^{27} \end{aligned}$$

Assume all Mn atoms are substitutionally sited on Ga sublattice, which contains 4 Ga atoms per unit cell.

Volume of one unit cell of GaAs:

$$\begin{aligned} &= (a_0)^3 \ \text{m}^{-3} \\ &= \left(5.6537 \times 10^{-10}\right)^3 \ \text{m}^{-3} \\ &= 1.807 \times 10^{-28} \ \text{m}^{-3} \end{aligned}$$

No of Ga atoms per 1 m^{-3}:

$$\begin{aligned} &= 4/1.807 \times 10^{-28} \\ &= 2.213 \times 10^{28} \end{aligned}$$

Percentage Mn:

$$\begin{aligned} &= \left(\frac{\text{No. of Mn atoms per } 1\text{m}^3}{\text{No. of Ga atoms per } 1\text{m}^3}\right) \times 100 \\ &= \left(\frac{1.498 \times 10^{27}}{2.213 \times 10^{-28}}\right) \times 100 \\ &= 6.7\% \end{aligned}$$

Appendix B

EXAFS Studies on LT GaAs

B.1 Fitting Results

B.1.1 Fitting Details

The spectra were background subtracted and the EXAFS backscattering oscillations were extracted using Athena from the iFEFFit software suite that was used for all data processing and analysis. Ga and As edge zinc-blende and rock-salt (RS) fitting models were constructed from the crystallographic structures using Atoms software. These models differed in space group, lattice constant and atomic coordinates. Two RS models were created: one had the same lattice constant as ZB GaAs (termed 'low a'), and the other had a lattice constant that was 15% larger than ZB GaAs (termed 'high a'), which represents the increase of cell volume from changing the first shell coordination number (N) from 4 (tetrahedral ZB) to 6 (octahedral RS), and correspondingly increasing the interatomic distances (R). The EXAFS data was then fitted to the ZB and RS structures, where for each coordination shell the fitted variables were the difference of interatomic distance between data and model (ΔR) and the Debye-Waller factor (σ^2, the mean squared displacement of interatomic distance i.e. a measure of structural disorder). Note that the coordination numbers were fixed to the theoretical values, and the same two shells were fitted for all of the samples i.e. first Ga and As shell.

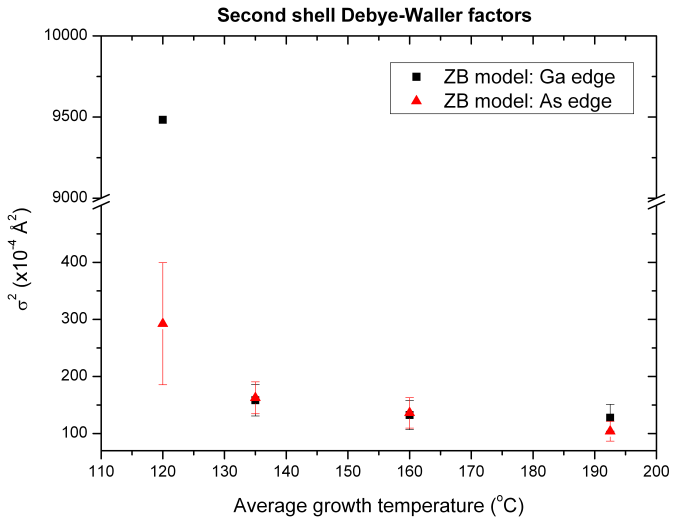

Figure B.1 – Second shell Debye-Waller factor using a zinc-blende model for LT GaAs grown at a variety of temperatures.

B.1.2 Results

The second shell Debye-Waller factor is responsive to structural disorder in GaAs. The fitting results in figure B.1 show that disorder increases with decreasing growth temperature, which agrees with observations of spectral broadening.

The difference between model and data-derived first shell interatomic distances (figure B.2) is very small when the zinc-blende model is applied, especially above the lowest growth temperature. The difference is greater for the rock-salt models, with the greatest disparity occurring for the more physically realistic high a rock-salt structure. For the rock-salt models, the magnitude of ΔR increases with growth temperature, showing a growing difference between the data and the rock-salt structure as structural order increases. The high a rock-salt model appears to show some applicability to the JH49, which was grown at the lowest temperature. Further inspection of the fitted Fourier transformed spectra however, shows that the first neighbouring atomic position (i.e. the major peak) was not actually being fitted.

The fit index quantifies the goodness of the overall fit on a scale from 0 to 1, a lower number indicating a better overlap, results are plotted in figure B.3.

The fit index is lowest when the zinc-blende model is applied to the data, and

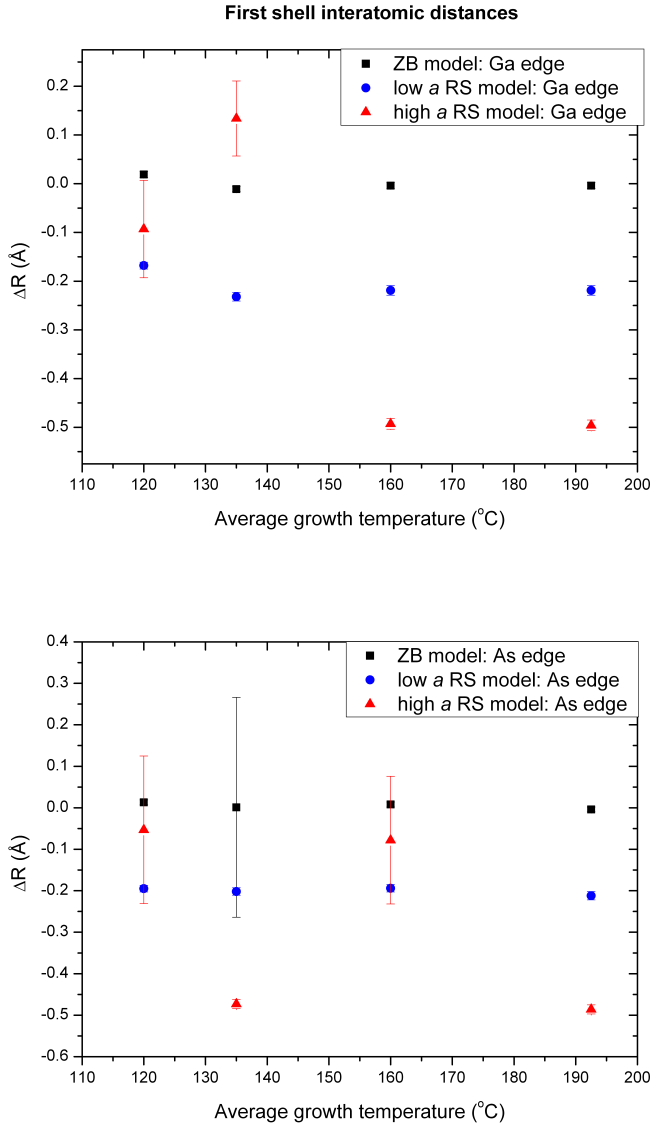

Figure B.2 – Plots of difference between model and data-derived first shell interatomic distances for all three applied models of measurements from LT GaAs samples grown at a variety of temperatures at both the Ga and As edge

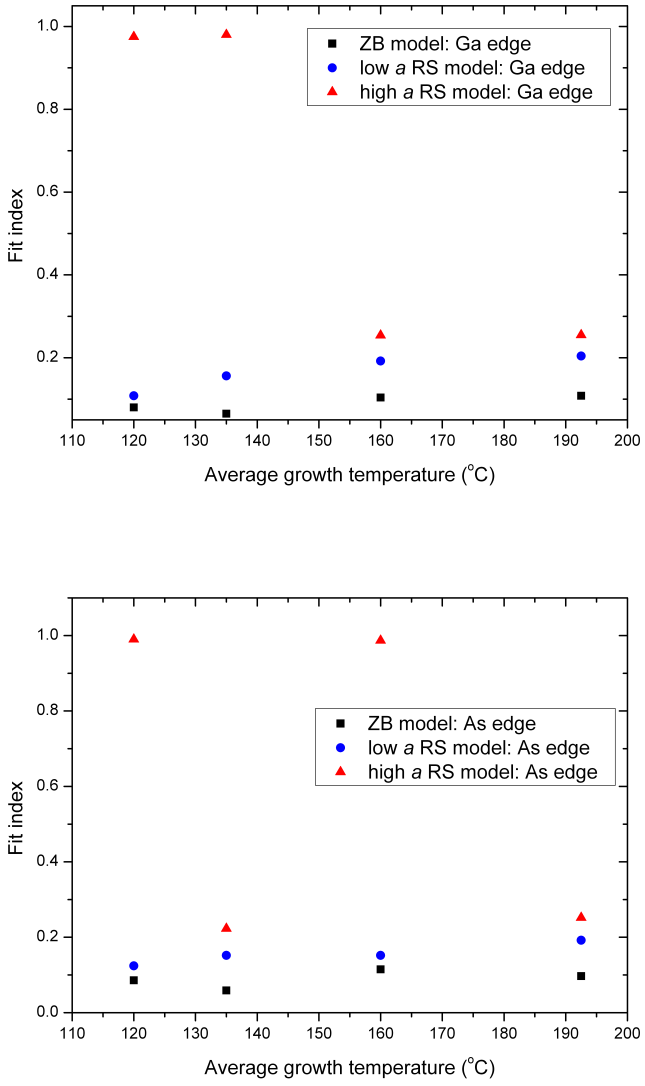

Figure B.3 – Fit index of all three applied models of measurements from LT GaAs samples grown at a variety of temperatures at both the Ga and As edge.

the high a rock-salt structure produces the worst fits. The very large indices for the high a rock-salt structure demonstrate that the first neighbour peak was not being fitted.

References

[1] M. Wang, R. P. Campion, K. W. Rushforth, A. W.and Edmonds, C. T. Foxon, G. B. L., Achieving high Curie temperature in (Ga,Mn)As, Applied Physics Letters 93 (2008) 132103.

[2] Ustinov VM and Zhukov AE, GaAs-based long-wavelength lasers, Semicond. Sci. Technol 15 (8) (2000) 41–54.

[3] Tu CW, Chen WM, Buyanova IA and Hwang JS, Material properties of dilute nitrides: Ga (In) NAs and Ga (In) NP, Journal of Crystal Growth 288 (1) (2006) 7–11.

[4] V. Grant, R. Campion, C. Foxon, W. Lu, S. Chao, E. Larkins, Optimization of RF plasma sources for the MBE growth of nitride and dilute nitride semiconductor material, Semiconductor Science and Technology 22 (2007) 15.

[5] Y. Li, D. Brenner, First principles prediction of the gas-phase precursors for AlN sublimation growth, Physical review letters 92 (7) (2004) 75503.

[6] C. Humphreys, Solid-state lighting, Mrs Bulletin 33.

[7] J. Orton, C. Foxon, Group III nitride semiconductors for short wavelength light-emitting devices, Rep. Prog. Phys 61 (1) (1998) 1–75.

[8] M. Moram, Y. Zhang, M. Kappers, Z. Barber, C. Humphreys, Dislocation reduction in gallium nitride films using scandium nitride interlayers, Applied Physics Letters 91 (2007) 152101.

[9] A. Herwadkar, W. Lambrecht, Mn-doped ScN: A dilute ferromagnetic semiconductor with local exchange coupling, Physical Review B 72 (23) (2005) 235207.

[10] W. Walukiewicz, J. Ager III, K. Yu, Z. Liliental-Weber, J. Wu, S. Li, R. Jones, J. Denlinger, TOPICAL REVIEW: Structure and electronic properties of InN and In-rich group III-nitride alloys, Journal of Physics D Applied Physics 39 (2006) 83.

[11] T. Ohashi, T. Kouno, M. Kawai, A. Kikuchi, K. Kishino, Growth and characterization of InGaN double heterostructures for optical devices at 1.5-1.7 mm communication wavelengths, PHYSICA STATUS SOLIDI C CONFERENCES 1 (10) (2004) 2850–2854.

[12] Y. Nanishi, Y. Saito, T. Yamaguchi, RF-molecular beam epitaxy growth and properties of InN and related alloys, Jpn. J. Appl. Phys 42 (2003) 2549.

[13] H. Komaki, R. Katayama, K. Onabe, M. Ozeki, T. Ikari, Nitrogen supply rate dependence of InGaN growth properties, by RF-MBE, Journal of Crystal Growth 305 (1) (2007) 12–18.

[14] A. Martí, C. Tablero, E. Antolín, A. Luque, R. Campion, S. Novikov, C. Foxon, Potential of Mn doped In1- xGaxN for implementing intermediate band solar cells, Solar Energy Materials and Solar Cells 93 (5) (2009) 641–644.

[15] A. Luque, A. Martí, Increasing the efficiency of ideal solar cells by photon induced transitions at intermediate levels, Physical Review Letters 78 (26) (1997) 5014–5017.

[16] Frank FC and van der Merwe JH, Proc. Royal Soc. A198 (1949) 205–216.

[17] Volmer M and Weber E, Z. Phys. Chem. 119 (1926) 227.

[18] Stranski IN and von Krastanow L, Natur. K1 IIb 146 (1939) 796.

[19] Franchi S, Trevisi G, Seravalli L and Frigeri P, Quantum dot nanostructures and molecular beam epitaxy, Progress in Crystal Growth and Characterization of Materials 47 (2) (2003) 166–195.

[20] M. Law, J. Goldberger, P. Yang, Semiconductor nanowires and nanotubes.

[21] C. Foxon, Three decades of molecular beam epitaxy, Journal of Crystal Growth 251 (1) (2003) 1–8.

[22] Y. Varshni, Temperature dependence of the energy gap in semiconductors, Physica 34 (1) (1967) 149–154.

[23] Harris JJ and Joyce B, Oscillations in the Surface Structure of Sn-Doped GaAs During Growth by MBE, Surface Science 103 (1) (1981) L90–L96.

[24] Bowen DK and Tanner BK, High Resolution X-Ray Diffractometry and Topography, Meas. Sci. Technol 11 (2000) 169.

[25] P. Fewster, X-Ray Scattering from Semiconductors, World Scientific, 2001.

[26] R. Wiesendanger, Scanning probe microscopy and spectroscopy: methods and applications, Cambridge University Press, 1994.

[27] P. Buseck, J. Cowley, L. Eyring, High-Resolution Transmission Electron Microscopy and Associated Techniques, Oxford University Press, 1988.

[28] `http://www.qdusa.com/resources/index.html`.

[29] K. Eid, M. Stone, K. Ku, O. Maksimov, P. Schiffer, N. Samarth, T. Shih, C. Palmstrøm, Exchange biasing of the ferromagnetic semiconductor GaMnAs, Applied Physics Letters 85 (2004) 1556.

[30] Hurle, Don, Private communication (2006).

[31] Anayama C, Tanahashi T, Kuwatsuka H, Nishiyama S, Isozumi S and Nakajima K, High-purity GaSb epitaxial layers grown from Sb-rich solutions, Applied Physics Letters 56 (1990) 239.

[32] Crain J, Ackland GJ, Maclean JR, Piltz RO, Hatton PD and Pawley GS, Reversible pressure-induced structural transitions between metastable phases of silicon, Phys. Rev. B 50 (17) (1994) 13043–13046.

[33] McMahon MI and Nelmes RJ, Observation of a Wurtzite Form of Gallium Arsenide, Physical Review Letters 95 (21) (2005) 215505.

[34] Z. Liliental-Weber, W. Swider, K. Yu, J. Kortright, F. Smith, A. Calawa, Breakdown of crystallinity in low-temperature-grown GaAs layers, Applied Physics Letters 58 (1991) 2153.

[35] Foxon, C.T., Private communication (2008).

[36] Liliental-Weber Z, Swider W, Yu KM, Kortright J, Smith FW and Calawa AR, Breakdown of crystallinity in low-temperature-grown GaAs layers, Applied Physics Letters 58 (1991) 2153.

[37] Zhao LX, Staddon CR, Wang KY, Edmonds KW, Campion RP, Gallagher BL and Foxon CT, Intrinsic and extrinsic contributions to the lattice parameter of GaMnAs, Applied Physics Letters 86 (2005) 071902.

[38] B. Teo, EXAFS: Basic Principles and Data Analysis, Springer-Verlag New York, 1986.

[39] G. Dalba, D. Diop, P. Fornasini, A. Kuzmin, F. Rocca, EXAFS and XANES study of GaAs on Ga and As K edges, Journal of Physics: Condensed Matter 5 (1993) 1643–1654.

[40] A. Suda, N. Otsuka, Arsenic flux dependence of incorporation of excess arsenic in molecular beam epitaxy of GaAs at low temperature, Applied Physics Letters 73 (1998) 1529.

[41] Y. Horikoshi, Migration-enhanced epitaxy of GaAs and AlGaAs, Semiconductor Science and Technology 8 (6) (1993) 1032–1051.

[42] P. Taylor, W. Jesser, M. Martinka, J. Dinan, Epitaxial growth of stoichiometric (100) GaAs at 75 C, Journal of Applied Physics 85 (1999) 3850.

[43] Dietl T, Ohno H, Matsukura F, Cibert J and Ferrand D, Zener Model Description of Ferromagnetism in Zinc-Blende Magnetic Semiconductors, Science 287 (5455) (2000) 1019–1022.

[44] X. Liu, A. Prasad, J. Nishio, E. Weber, Z. Liliental-Weber, W. Walukiewicz, Native point defects in low-temperature-grown GaAs, Applied Physics Letters 67 (1995) 279.

[45] Temkin H, Coblentz D, Logan RA, van der Ziel JP, Tanbun-Ek T, Yadvish RD and Sergent AM, High temperature characteristics of InGaAsP/InP laser structures, Applied Physics Letters 62 (1993) 2402.

[46] Pessa M, Peng CS, Jouhti T, Pavelescu EM, Li W, Karirinne S, Liu H and Okhotnikov O, Long-wavelength nitride lasers on GaAs, Microelectronic Engineering 69 (2-4) (2003) 195–207.

[47] Ledentsov N, Bimberg D, Ustinov VM, Alferov ZI and Lott JA, Quantum dots for VCSEL applications at λ= 1.3 μm, Physica E: Low-dimensional Systems and Nanostructures 13 (2-4) (2002) 871–875.

[48] Blum O and Klem JF, IEEE Photonics Technol. Lett. 12 (2-4) (2000) 771–3.

[49] Harris JS, GaInNAs long-wavelength lasers: progress and challenges, Semiconductor Science and Technology 17 (8) (2002) 880–891.

[50] Ha W, Gambin V, Wistey M, Bank S, Yuen H, Kim S and Harris Jr, JS, Long wavelength GaInNAsSb/GaNAsSb multiple quantum well lasers, Electronics Letters 38 (6) (2002) 277–278.

[51] Weyers M, Sato M and Ando H, Red shift of photoluminescence and absorption in dilute GaAsN alloy layers, Jpn. J. Appl. Phys 31 (1992) L853–L855.

[52] Kondow M, Uomi K, Niwa A, Kitatani T, Watahiki S and Yazawa Y, GaInNAs: A novel material for long-wavelength-range laser diodes with excellent high-temperature performance, Jpn. J. Appl. Phys 35 (2B) (1996) 1273.

[53] Riechert H, Ramakrishnan A and Steinle G, Development of InGaAsN-based 1.3 mm VCSELs, Semicond. Sci. Technol 17 (8) (2002) 892–897.

[54] Shan W, Walukiewicz W, Ager III JW, Haller EE, Geisz JF, Friedman DJ, Olson JM and Kurtz SR, Effect of nitrogen on the band structure of GaInNAs alloys, Journal of Applied Physics 86 (1999) 2349.

[55] Ralston JD, Weisser S, Esquivias I, Larkins EC, Rosenzweig J, Tasker PJ and Fleissner J, Control of differential gain, nonlinear gain and damping factor forhigh-speed application of GaAs-based MQW lasers, Quantum Electronics, IEEE Journal of 29 (6) (1993) 1648–1659.

[56] Raghothamachar B, Dudley M, Rojo JC, Morgan K and Schowalter LJ, X-ray characterization of bulk AlN single crystals grown by the sublimation technique., Journal of Crystal Growth 250 (1) (2003) 244–250.

[57] Karpov SY, Zimina DV, Makarov YN, Mokhov EN, Roenkov AD, Ramm MG and Vodakov YA, Sublimation Growth of AlN in Vacuum and in a Gas Atmosphere, physica status solidi(a) 176 (1) (1999) 435–438.

[58] X. Shen, Y. Fu, G. Feng, B. Zhang, Z. Feng, Y. Wang, H. Yang, Structural characterization of epitaxial lateral overgrown GaN on patterned GaN/GaAs (001) substrates, Journal of Crystal Growth 246 (1) (2002) 69–72.

[59] P. Gibart, Metal organic vapour phase epitaxy of GaN and lateral overgrowth, Reports on Progress in Physics 67 (5) (2004) 667–715.

[60] I. Akasaki, H. Amano. Y. Koide, K. Hiramatsu, and N. Sawaki, J. Cryst. Growth 98 (1989) 209.

[61] M. Kappers, R. Datta, R. Oliver, F. Rayment, M. Vickers, C. Humphreys, Threading dislocation reduction in (0001) GaN thin films using SiNx interlayers, Journal of Crystal Growth 300 (1) (2007) 70–74.

[62] A. Smith, H. Al-Brithen, D. Ingram, D. Gall, Molecular beam epitaxy control of the structural, optical, and electronic properties of ScN (001), Journal of Applied Physics 90 (2001) 1809.

[63] H. A. Al-Brithen, A. R. Smith, D. Gall, Surface and bulk electronic structure of *scn*(001) investigated by scanning tunneling microscopy/spectroscopy and optical absorption spectroscopy, Phys. Rev. B 70 (4) (2004) 045303.

[64] M. E. K. Xuewen Bai, Structure and optical properties of ScN thin films, Applied Surface Science 175-176 (2001) 499.

[65] D. Gall, I. Petrov, P. Desjardins, J. Greene, Microstructural evolution and Poisson ratio of epitaxial ScN grown on TiN (001)/MgO (001) by ultrahigh vacuum reactive magnetron sputter deposition, Journal of Applied Physics 86 (1999) 5524.

[66] Z. Gu, J. Edgar, J. Pomeroy, M. Kuball, D. Coffey, Crystal growth and properties of scandium nitride, Journal of Materials Science: Materials in Electronics 15 (8) (2004) 555–559.

[67] R. Niewa, D. Zherebtsov, M. Kirchner, M. Schmidt, W. Schnelle, New Ways to High-Quality Bulk Scandium Nitride, Chem. Mater 16 (25) (2004) 5445–5451.

[68] J. Dismukes, W. Yim, V. Ban, Journal of Crystal Growth 13-14 (1972) 362.

[69] T. Moustakas, R. Molnar, J. Dismukes, Electrochem. Soc. Proceedings 96 (11) (1996) 197.

[70] D. Gall, I. Petrov, N. Hellgren, L. Hultman, J. Sundgren, J. Greene, Growth of poly-and single-crystal ScN on MgO (001): Role of low-energy N irradiation in determining texture, microstructure evolution, and mechanical properties, Journal of Applied Physics 84 (1998) 6034.

[71] H. Al-Brithen, A. Smith, Molecular beam epitaxial growth of atomically smooth scandium nitride films, Applied Physics Letters 77 (2000) 2485.

[72] M. Moram, T. Joyce, P. Chalker, Z. Barber, C. Humphreys, Microstructure of epitaxial scandium nitride films grown on silicon, Applied Surface Science 252 (24) (2006) 8385–8387.

[73] M. Moram, S. Novikov, A. Kent, C. Nörenberg, C. Foxon, C. Humphreys, Growth of epitaxial thin films of scandium nitride on 100-oriented silicon, Journal of Crystal Growth (2008) 2746–2750.

[74] B. Heying, R. Averbeck, L. Chen, E. Haus, H. Riechert, J. Speck, Control of GaN surface morphologies using plasma-assisted molecular beam epitaxy, Journal of Applied Physics 88 (2000) 1855.

[75] L. Jenkins, T. Cheng, C. Foxon, S. Hooper, J. Orton, S. Novikov, V. Tretyakov, Auger electron spectroscopy, x-ray diffraction, and scanning electron microscopy of InN, GaN, and Ga (AsN) films on GaP and GaAs (001) substrates, Journal of Vacuum Science & Technology B: Microelectronics and Nanometer Structures 13 (1995) 1585.

[76] T. Lei, K. Ludwig Jr, T. Moustakas, Heteroepitaxy, polymorphism, and faulting in GaN thin films on silicon and sapphire substrates, Journal of Applied Physics 74 (1993) 4430.

[77] M. Moram, M. Vickers, X-ray diffraction of III-nitrides, Reports on Progress in Physics 72 (2009) 036502.

[78] C. Constantin, H. Al-Brithen, M. Haider, D. Ingram, A. Smith, ScGaN alloy growth by molecular beam epitaxy: Evidence for a metastable layered hexagonal phase, Physical Review B 70 (19) (2004) 193309.

[79] W. Yim, E. Stofko, R. Smith, Vapor Growth and Properties of ScAs and ScP, Journal of Applied Physics 43 (1972) 254.

[80] B. Lépine, A. Quémerais, D. Sébilleau, G. Jézéquel, D. Agliz, Y. Ballini, A. Guivarch, X-ray photoelectron diffraction study of YbAs/GaAs (001) and ScAs/GaAs (001) heterostructures, Journal of Applied Physics 76 (1994) 5218.

[81] A. Tebboune, D. Rached, A. Benzair, N. Sekkal, A. Belbachir, Structural and electronic properties of ScSb, ScAs, ScP and ScN., Physica Status Solidi(b) 243 (12) (2006) 2788–2795.

[82] W. Lambrecht, Electronic structure and optical spectra of the semimetal ScAs and of the indirect-band-gap semiconductors ScN and GdN, Physical Review B 62 (20) (2000) 13538–13545.

[83] A. Maachoua, B. Amranib, M. Drizc, Electronic structure and optical spectra of the semimetal ScAs and of the indirect-band-gap semiconductors ScN and GdN, Physica B 388 (2007) 348–389.

[84] M. Moreno-Armenta, L. Mancera, N. Takeuchi, First principles total energy calculations of the structural and electronic properties of ScxGa1-xN, Physica Status Solidi-B-Basic Research 238 (1) (2003) 127–135.

[85] N. Takeuchi, First-principles calculations of the ground-state properties and stability of ScN, Physical Review B 65 (4) (2002) 45204.

[86] N. Farrer, L. Bellaiche, Properties of hexagonal ScN versus wurtzite GaN and InN, Physical Review B 66 (20) (2002) 201203.

[87] W. Adli, R. Mecheref, N. Sekkal, F. Tair, B. Amrani, FIRST PRINCIPLE STUDY OF CUBIC ScGaN TERNARIES.

[88] S. Zerroug, F. Sahraoui, N. Bouarissa, Ab initio calculations of structural properties of ScGaN, Journal of Applied Physics 103 (2008) 063510.

[89] T. Moustakas, J. Dismukes, S. Pearton, III-V nitride materials and processes, CONF-960502–, Electrochemical Society, Inc., Pennington, NJ (United States), 1996.

[90] M. Little, M. Kordesch, Band-gap engineering in sputter-deposited ScGaN, Applied Physics Letters 78 (2001) 2891.

[91] H. Al-Brithen, H. Yang, A. Smith, Incorporation of manganese into semiconducting ScN using radio frequency molecular beam epitaxy, Journal of Applied Physics 96 (2004) 3787.

[92] M. Haider, C. Constantin, H. Al-Brithen, H. Yang, E. Trifan, D. Ingram, A. Smith, C. Kelly, Y. Ijiri, Ga/N flux ratio influence on Mn incorporation, surface morphology, and lattice polarity during radio frequency molecular beam epitaxy of (Ga, Mn) N, Journal of Applied Physics 93 (2003) 5274.

[93] H. Yang, H. Al-Brithen, E. Trifan, D. Ingram, A. Smith, Crystalline phase and orientation control of manganese nitride grown on MgO (001) by molecular beam epitaxy, Journal of Applied Physics 91 (2002) 1053.

[94] C. Constantin, Growth, Structural, Electronic and Optical Characterization of Nitride Semiconductors Grown by rf-Plasma Molecular Beam Epitaxy.

[95] J. Zhao, A. Wang, M. Green, 24.5% Effiency Silicon PERT Cells on MCZ Substrates and 24.7% Effiency PERL Cells on FZ Substrates, Prog. Photovolt 7 (471) (1999) 144.

[96] W. Shockley, H. Queisser, Detailed Balance Limit of Efficiency of p-n Junction Solar Cells, Journal of Applied Physics 32 (1961) 510–519.

[97] G. Conibeer, Third-generation photovoltaics, Materials Today 10 (11) (2007) 42–50.

[98] A. Martí, L. Cuadra, A. Luque, Quantum dot intermediate band solar cell, in: Photovoltaic Specialists Conference, 2000. Conference Record of the Twenty-Eighth IEEE, 2000, pp. 940–943.

[99] K. Yu, W. Walukiewicz, J. Wu, W. Shan, J. Beeman, M. Scarpulla, O. Dubon, P. Becla, Diluted II-VI oxide semiconductors with multiple band gaps, Physical review letters 91 (24) (2003) 246403.

[100] K. Yu, W. Walukiewicz, J. Ager III, D. Bour, R. Farshchi, O. Dubon, S. Li, I. Sharp, E. Haller, Multiband GaNAsP quaternary alloys, Applied Physics Letters 88 (2006) 092110.

[101] P. Palacios, J. Fernández, K. Sánchez, J. Conesa, P. Wahnon, First-principles investigation of isolated band formation in half-metallic Ti_ {x} Ga_ {1- x} P (x= 0.3125–0.25), Physical Review B 73 (8) (2006) 85206.

[102] P. Palacios, K. Sánchez, J. Conesa, P. Wahnón, First principles calculation of isolated intermediate bands formation in a transition metal chalcopyrite semiconductor, Phys. Stat. Sol.(a) 203 (2006) 1395–1401.

[103] E. Cánovas, A. Martí, A. Luque, W. Walukiewicz, Optimum nitride concentration in multiband III-N–V alloys for high efficiency ideal solar cells, Applied Physics Letters 93 (2008) 174109.

[104] X. Cui, Z. Tao, R. Zhang, X. Li, X. Xiu, Z. Xie, S. Gu, P. Han, Y. Shi, Y. Zheng, Structural and magnetic properties in Mn-doped GaN grown by metal organic chemical vapor deposition, Applied Physics Letters 92 (2008) 152116.

[105] H. Munekata, H. Ohno, S. Von Molnar, A. Segm
"uller, L. Chang, L. Esaki, Diluted magnetic III-V semiconductors, Physical Review Letters 63 (17) (1989) 1849–1852.

[106] M. Reed, E. Berkman, M. Reed, F. Arkun, T. Chikyow, S. Bedair, J. Zavada, N. El-Masry, Magnetic properties of Mn-doped GaN, InGaN, And AlGaN, in: MATERIALS RESEARCH SOCIETY SYMPOSIUM PROCEEDINGS., Vol. 798, Warrendale, Pa.; Materials Research Society; 1999, 2003, pp. 563–568.

[107] Y. Saito, H. Harima, E. Kurimoto, T. Yamaguchi, N. Teraguchi, A. Suzuki, T. Araki, Y. Nanishi, Growth Temperature Dependence of Indium Nitride Crystalline Quality Grown by RF-MBE, Physica Status Solidi B Basic Research 234 (3) (2002) 796–800.

[108] J. Wu, W. Walukiewicz, K. Yu, W. Shan, J. Ager III, E. Haller, H. Lu, W. Schaff, W. Metzger, S. Kurtz, Superior radiation resistance of InGaN alloys: Full-solar-spectrum photovoltaic material system, Journal of Applied Physics 94 (2003) 6477.

[109] W. Walukiewicz, S. Li, J. Wu, K. Yu, J. Ager, E. Haller, H. Lu, W. Schaff, Optical properties and electronic structure of InN and In-rich group III-nitride alloys, Journal of Crystal Growth 269 (1) (2004) 119–127.

[110] I. Mahboob, T. Veal, C. McConville, H. Lu, W. Schaff, Intrinsic electron accumulation at clean InN surfaces, Physical review letters 92 (3) (2004) 36804.

[111] P. King, T. Veal, H. Lu, P. Jefferson, S. Hatfield, W. Schaff, C. McConville, Surface electronic properties of n-and p-type InGaN alloys, Physica Status Solidi-B-Basic Solid State Physics 245 (5) (2008) 881–883.

[112] L. Bailey, T. Veal, P. King, C. McConville, J. Pereiro, J. Grandal, M. Sánchez-García, E. Muñoz, E. Calleja, Band bending at the surfaces of In-rich InGaN alloys, Journal of Applied Physics 104 (2008) 113716.

[113] M. Moret, B. Gil, S. Ruffenach, O. Briot, C. Giesen, M. Heuken, S. Rushworth, T. Leese, M. Succi, Optical, structural investigations and band-gap bowing parameter of GaInN alloys, Journal of Crystal Growth 311 (10) (2009) 2795–2797.

[114] D. Doppalapudi, S. Basu, K. Ludwig Jr, T. Moustakas, Phase separation and ordering in InGaN alloys grown by molecular beam epitaxy, Journal of Applied Physics 84 (1998) 1389.

[115] A. Wakahara, T. Tokuda, X. Dang, S. Noda, A. Sasaki, Compositional inhomogeneity and immiscibility of a GaInN ternary alloy, Applied Physics Letters 71 (1997) 906.

[116] M. McCluskey, L. Romano, B. Krusor, D. Bour, N. Johnson, S. Brennan, Phase separation in InGaN/GaN multiple quantum wells, Applied Physics Letters 72 (1998) 1730.

[117] H. Komaki, T. Nakamura, R. Katayama, K. Onabe, M. Ozeki, T. Ikari, Growth of In-rich InGaN films on sapphire via GaN layer by RF-MBE, Journal of Crystal Growth 301 (2007) 473–477.

[118] X. Chen, K. Matthews, D. Hao, W. Schaff, L. Eastman, Growth, fabrication, and characterization of InGaN solar cells, Physica Status Solidi(a) 205 (5) (2008) 1103–1105.

[119] F. Yam, Z. Hassan, InGaN: An overview of the growth kinetics, physical properties and emission mechanisms, Superlattices and Microstructures 43 (1) (2008) 1–23.

[120] T. Bottcher, S. Einfeldt, V. Kirchner, S. Figge, H. Heinke, D. Hommel, H. Selke, P. Ryder, Incorporation of indium during molecular beam epitaxy of InGaN, Applied Physics Letters 73 (1998) 3232.

[121] Q. Guo, H. Ogawa, H. Yamano, A. Yoshida, Growth of InN films on GaAs (111) and GaP (111) substrates by microwave-excited metalorganic vapor phase epitaxy, Applied Physics Letters 66 (1995) 715.

[122] A. Bhuiyan, A. Hashimoto, A. Yamamoto, Indium nitride (InN): A review on growth, characterization, and properties, Journal of Applied Physics 94 (2003) 2779.

[123] J. Wu, W. Walukiewicz, Band gaps of InN and group III nitride alloys, Superlattices and microstructures 34 (1-2) (2003) 63–75.

[124] K. Ploog, A. Fischer, Surface segregation of Sn during MBE of n-type GaAs established by SIMS and AES, Journal of Vacuum Science and Technology 15 (1978) 255.

[125] D. Hurle, A comprehensive thermodynamic analysis of native point defect and dopant solubilities in gallium arsenide, Journal of Applied Physics 85 (1999) 6957.

[126] G. Thaler, M. Overberg, B. Gila, R. Frazier, C. Abernathy, S. Pearton, J. Lee, S. Lee, Y. Park, Z. Khim, et al., Magnetic properties of n-GaMnN thin films, Applied Physics Letters 80 (2002) 3964.

[127] S. Novikov, K. Edmonds, L. Zhao, A. Giddings, K. Wang, R. Campion, C. Staddon, M. Fay, Y. Han, P. Brown, et al., Mn doping and p-type conductivity in zinc-blende GaMnN layers grown by molecular beam epitaxy, Journal of Vacuum Science & Technology B: Microelectronics and Nanometer Structures 23 (2005) 1294.

[128] P. Thompson, Y. Li, J. Zhou, D. Sato, L. Flanders, H. Lee, Diffuse reflectance spectroscopy measurement of substrate temperature and temperature transient during molecular beam epitaxy and implications for low-temperature III–V epitaxy, Applied Physics Letters 70 (1997) 1605.

[129] B. Shanabrook, J. Waterman, J. Davis, R. Wagner, Large temperature changes induced by molecular beam epitaxial growth on radiatively heated substrates, Applied Physics Letters 61 (1992) 2338.

[130] V. Novák, K. Olejník, M. Cukr, L. Smrčka, Z. Remeš, J. Oswald, Substrate temperature changes during molecular beam epitaxy growth of GaMnAs, Journal of Applied Physics 102 (2007) 083536.

[131] Q. Guo, A. Yoshida, Temperature dependence of band gap change in InN and AlN, Jpn. J. Appi. Phys. Vol 33 (1994) 2453–2456.

[132] P. Pigeat, D. Rouxel, B. Weber, Calculation of thermal emissivity for thin films by a direct method, Physical Review B 57 (15) (1998) 9293–9300.

[133] D. Lockwood, G. Yu, N. Rowell, Optical phonon frequencies and damping in AlAs, GaP, GaAs, InP, InAs and InSb studied by oblique incidence infrared spectroscopy, Solid State Communications 136 (7) (2005) 404–409.

[134] D. Wang, C. Tin, J. Williams, M. Park, Y. Park, C. Park, T. Kang, W. Yang, Raman characterization of electronic properties of self-assembled GaN nanorods grown by plasma-assisted molecular-beam epitaxy, Applied Physics Letters 87 (2005) 242105.

[135] K. Kurihara, T. Yanagawa, N. Nakagawa, K. Fukui, A. Yamamoto, Temperature dependence of infrared reflectance spectra of InN, Infrared Physics and Technology 51 (5) (2008) 482–484.